TECHNISCHE UNIVERSITÄT WIEN
Vienna University of Technology

Dissertation

Investigation of stabilized $Li_7La_3Zr_2O_{12}$ garnets by combining electrochemical measurements with chemical analysis

ausgeführt zum Zwecke der Erlangung des akademischen Grades eines Doktors der technischen Wissenschaften (Dr. techn.), eingereicht and der TU Wien, Fakultät für Technische Chemie, von

Stefan Smetaczek

Mat.Nr.: 01025186

[redacted]

unter der Leitung von

Univ.Prof. Dipl.-Phys. Dr.rer.nat. Jürgen Fleig

Institute of Chemical Technologies and Analytics, E164

Wien, im Juni 2021

Dipl.-Ing. Stefan Smetaczek, BSc

Abstract

Current Li-ion batteries (LIBs) suffer from issues caused by the instability of the utilized organic electrolytes. For safety and performance improvements, replacing them by inorganic solid ion conductors is of major interest. Due to their high Li-ion conductivity and stability against metallic Li, cubic $Li_7La_3Zr_2O_{12}$ (LLZO) garnets are among the most promising solid electrolytes to be employed in future LIBs.

In this thesis the investigation of several LLZO key properties employing a combination of electrochemical measurements and chemical analysis is presented. Among the used techniques are microelectrode electrochemical impedance spectroscopy (ME-EIS), direct current (DC) chronoamperometry, laser ablation inductively coupled plasma optical emission spectroscopy (LA-ICP-OES) as well as -mass spectrometry (LA-ICP-MS), and laser induced breakdown spectroscopy (LIBS).

To investigate conductivity fluctuations within LLZO and their relation to the material composition, local conductivity measurements are correlated with spatially resolved chemical analysis. Not only differences between nominally identical samples are shown, but also distinct local conductivity and stoichiometry variations within individual pellets revealed. No clear correlation between composition and conductivity behavior is observable, indicating that a yet unknow factor (e.g., oxygen vacancies or local cation site occupancies) has a high impact on the ionic conductivity.

Furthermore, the electrochemical stability and decomposition behavior of LLZO is examined using various field stress experiments in combination with subsequent material characterization. It is shown that LLZO decomposition starts at approx. 4.1–4.3 V vs. Li^+/Li, leading to the formation of Li-poor phases like $La_2Zr_2O_7$ beneath the positively polarized electrode. The reaction is still on-going even after several days of polarization (i.e., no blocking interfacial layer is formed), and is observable not only at elevated but also at room temperature, questioning the compatibility of LLZO with high voltage cathode materials.

Lastly, moisture-induced chemical degradation and Li^+/H^+ exchange of LLZO is investigated using depth-resolved H and Li determination after exposure to H_2O. The experiments reveal that polycrystalline samples show a much more pronounced Li^+/H^+ exchange than LLZO single crystals, indicating an increased H^+ diffusion along the grain boundaries of the material.

Kurzfassung

Einige der schwerwiegendsten Probleme moderner Li-Ionen-Akkumulatoren ergeben sich durch die chemische Instabilität der verwendeten organischen Elektrolyte. Es ist daher von großem Interesse, diese durch anorganische Festkörperelektrolyte zu ersetzen und auf diesem Wege die Sicherheit sowie die Leistungsfähigkeit der Akkumulatoren zu verbessern. Zu den vielversprechendsten Materialien für den Einsatz in zukünftigen Systemen zählen gegenwärtig kubische $Li_7La_3Zr_2O_{12}$ (LLZO) Granate, die sich durch ihre hohe Li-Ionen Leitfähigkeit sowie ihre Stabilität gegenüber metallischem Lithium auszeichnen.

Aufbauend auf den aktuellen Forschungsstand beschäftigt sich die vorliegende Arbeit mit unterschiedlichen ungeklärten Fragen hinsichtlich der Materialeigenschaften von LLZO. Zu diesem Zweck wurde eine Kombination aus elektrochemischen Messungen und chemischen Analysen zum Einsatz gebracht. Die dabei verwendeten Techniken inkludieren Mikroelektroden - elektrochemische Impedanzspektroskopie (ME-EIS), Chronoamperometrie, Laserablation - induktiv gekoppeltes Plasma - optische Emissionsspektroskopie (LA-ICP-OES) und - Massenspektrometrie (LA-ICP-MS) sowie laserinduzierte Plasmaspektroskopie (LIBS).

Um mögliche Leitfähigkeitsschwankungen innerhalb der Granate und ihren Zusammenhang mit der Materialzusammensetzung zu untersuchen, wurden lokale Leitfähigkeitsmessungen mit ortsaufgelösten chemischen Analysen kombiniert. Die Ergebnisse dieser Messungen machen nicht nur Unterschiede zwischen nominell identen Proben deutlich, sondern zeigen auch ausgeprägte Variationen der lokalen Leitfähigkeit sowie Stöchiometrie innerhalb einzelner Proben. Eine in diesem Zusammenhang fehlende Korrelation zwischen chemischer Zusammensetzung und Leitfähigkeit deutet darauf hin, dass ein noch unbekannter Faktor (z. B. Sauerstoff-Leerstellen oder die exakten Belegungen der verschiedenen Gitterplätze) entscheidende Auswirkungen auf die ionische Leitfähigkeit hat.

Des Weiteren wurden die elektrochemische Stabilität sowie das Zersetzungsverhalten von LLZO geprüft, indem verschiedene Feldbelastungs-Experimente gemeinsam mit nachfolgender Materialcharakterisierung eingesetzt wurden. Hierbei wurde deutlich, dass sich LLZO bei etwa 4.1–4.3 V gegen Li^+/Li zu zersetzen beginnt, wodurch sich unter der positiv polarisierten Elektrode Li-arme Phasen wie beispielsweise $La_2Zr_2O_7$ bilden. Die Tatsache, dass diese Reaktion auch nach mehreren Tagen Polarisation andauert (d. h. es bildet sich keine blockierende Passivierungsschicht) und nicht nur bei erhöhten Temperaturen, sondern auch bei Raumtemperatur erkennbar ist, stellt die Kompatibilität von LLZO mit Hochvolt-Kathodenmaterialien in Frage.

Abschließend wurden zur Untersuchung der durch Feuchtigkeit hervorgerufenen LLZO Degradation und des damit verbundenen Li^+/H^+ Austausches tiefenaufgelöste chemische Analysen eingesetzt. Die Ergebnisse machen hierbei deutlich, dass polykristallinen Proben nach Kontakt mit H_2O einen stark erhöhten Ionenaustausch im Vergleich zu entsprechenden Einkristallen zeigen, was auf eine beschleunigte H^+ Diffusion entlang der Korngrenzen hinweist.

Danksagung

Zahlreiche Personen haben mich bei der Anfertigung meiner Dissertation unterstützt, wofür ich mich dieser Stelle herzlich bedanken möchte.

Zuallererst gebührt Prof. Jürgen Fleig mein Dank, bei dem ich mich sowohl fachlich als auch menschlich stets besten betreut gefühlt habe. Immer wenn ich Unterstützung brauchte, stand seine Tür für mich offen – sowohl im übertragenen Sinne als auch wörtlich, und sein Fachwissen sowie Ideenreichtum haben diese Arbeit wesentlich bereichert. Gleiches gilt für Prof. Andreas Limbeck, dessen Anregungen für die Bewältigung einer Vielzahl analytischer Frage- und Problemstellungen entscheidend waren.

Mein Dank gilt auch dem FWF und dem Projekt „Solids4Fun“ für die Finanzierung der hier präsentierten Forschung, sowie den verschiedenen Kooperationspartnern für die äußerst produktive Zusammenarbeit. Speziell möchte ich mich hierbei bei Dr. Reinhard Wagner, Dr. Steffen Ganschow und Dr. Daniel Rettenwander für die Probenherstellung sowie -vermittlung bedanken.

Besonders danken möchte ich auch meinem „Vorgänger“ Dr. Andreas Wachter-Welzl (a.k.a. Plüsch) sowie meinen ehemaligen Diplomanden Joseph Ring und Eva Pycha, die durch ihre Experimente wesentlich zu dem Erfolg dieser Arbeit beigetragen haben. Auch bei allen anderen (ehemaligen) Mitgliedern der Forschungsgruppe möchte ich mich herzlich bedanken: für ihre geschlossene Hilfsbereitschaft, ihren Humor, sowie das dadurch entstandene Arbeitsklima. Danke Max (a.k.a. Absolute Unit), Harald, Christin, Matthäus, Martin, Andi, Markus, Tobi, Steffi, Christoph, Andreas, Clemens, Richard, und natürlich auch Alex, Alex, Alex und Alex.

Natürlich gilt mein Dank auch all meinen Kollegen „auf der Analytik“, mit denen ich stets gerne zusammengearbeitet habe. Speziell bedanken möchte ich mich bei Christopher und Lukas, die unter anderem durch unsere – teilweise recht ausgedehnten („geh ma hald schnell rauf zum Westbahnhof“) – gemeinsamen Mittagessen meinen Arbeitsalltag mitgestaltet haben.

Abschließend möchte ich mich von ganzem Herzen bei meiner Familie bedanken, die mich während meiner Zeit an der Universität auf jede erdenkliche Weise unterstützt und diesen Abschluss dadurch überhaupt erst möglich gemacht hat. Ein besonderer Dank gilt meiner Freundin Christine und unserem Hund Koda, die seit mehr als sechs Jahren die besten Wegbegleiter sind, die ich mir vorstellen kann.

Vielen Dank!

Table of contents

Abstract ..... **III**

Kurzfassung ..... **IV**

Danksagung ..... **VI**

Table of contents ..... **VII**

1 Introduction **1**

2 Spatially resolved stoichiometry determination of $Li_7La_3Zr_2O_{12}$ solid-state electrolytes using LA-ICP-OES **6**

2.1 Introduction **6**

2.2 Experimental **8**

2.2.1 LLZO synthesis 8

2.2.2 Preparation of matrix-matched standards 8

2.2.3 Bulk analysis via liquid ICP-OES 9

2.2.4 LA-ICP-OES and -MS calibration 10

2.2.5 Elemental imaging 13

2.2.6 Validation approach 14

2.3 Results and discussion **14**

2.3.1 Standard characterization 14

2.3.2 LA-ICP-OES calibration 16

2.3.3 Quantitative LLZO imaging 19

2.3.4 Method validation 21

2.4 Conclusion **22**

3 Local Li-ion conductivity changes within Al stabilized $Li_7La_3Zr_2O_{12}$ solid electrolytes and their relation to three-dimensional variations of the bulk composition **23**

3.1 Introduction **23**

3.2 Experimental **24**

3.2.1 Sample preparation 24

3.2.2 X-ray diffraction 24

3.2.3 Electrochemical impedance spectroscopy 24

3.2.4 LA-ICP-OES 25

3.3 Results and discussion **26**

3.3.1 Sample quality 26

3.3.2 Macroelectrode measurements 27

3.3.3 Microelectrode measurements 29
3.3.4 Local conductivities 30
3.3.5 LA-ICP-OES analysis 33
3.3.6 Correlation of conductivity and chemical composition 39

3.4 Conclusion 42

4 Investigating the electrochemical stability of $Li_7La_3Zr_2O_{12}$ solid electrolytes using field stress experiments 44

4.1 Introduction 44
4.2 Experimental 45
4.2.1 LLZO synthesis 45
4.2.2 Field stress experiments 47

4.3 Polarization of stripe electrodes 50
4.3.1 Morphology changes 51
4.3.2 (Electro)chemical analysis 53

4.4 Polarization of microelectrodes 55
4.4.1 Stepwise voltage increase 56
4.4.2 Constant voltage 58
4.4.3 Polarization at room temperature 64

4.5 Conclusion 66

5 Impact of H_2O exposure on $Li_7La_3Zr_2O_{12}$ garnets: Investigate Li^+/H^+ exchange using LIBS depth profiling 67

5.1 Introduction 67
5.2 Experimental 68
5.2.1 H_2O exposure 68
5.2.2 ICP-OES measurements 69
5.2.3 LIBS measurements 70
5.2.4 EIS 72

5.3 Results and discussion 73
5.3.1 H_2O analysis via ICP-OES 73
5.3.2 LLZO analysis via LIBS 77
5.3.3 Impact on the conductivity behavior 82

5.4 Conclusion 85

6 Summary 86

List of abbreviations and symbols 90

References 92

1 Introduction

The increasing demand of energy storage and energy conversion is one of the greatest challenges of our modern society. Mitigating CO_2 emission is necessary to avoid climatic consequences, and fossil fuels are becoming increasingly scarce, making a shift to renewable and clean energy sources more and more important. Due to the intermittent character of most renewable sources such as wind and solar energy, this shift is accompanied by a growing need for load-levelling in form of large-scale energy storage. Moreover, portable electronic devices play a crucial role in our modern society and are constantly advancing, further increasing the demands on energy storage systems. Overall, energy storage technologies with higher energy and power densities, better safety, and lower cost are of uttermost interest.

Li-ion batteries (LIBs) can be found in most portable electronics and are utilized in emerging key applications such electric vehicles and stationary load-levelling.[1–5] Among the different existing battery technologies, Li-based ones offer the highest volumetric and gravimetric energy density (Figure 1.01) and are therefore the most promising option to face the upcoming challenges.[6] The reason for that is that Li is the lightest metal (relative density $\rho = 0.53$ g cm^{-3}), and also the one with the most negative electrochemical potential (–3.04 V vs. standard hydrogen electrode), thus enabling to store more energy per mass (or volume) than other systems.

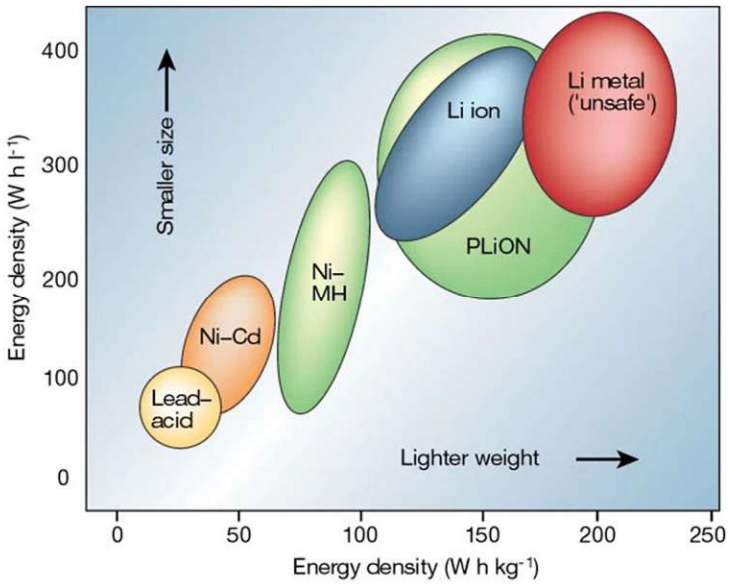

Figure 1.01: Volumetric and gravimetric energy density of the different battery technologies, namely lead-acid, nickel cadmium (Ni-Cd), nickel metal hydride (Ni-MH), Li-ion, plastic Li-ion (PLiON), and Li metal. Li-based batteries have superior energy density, especially if metallic Li is used as anode. Reprinted from Ref. [6].

Batteries are electrochemical devices which can convert chemical energy into electrical energy through a reduction-oxidation (redox) reaction. They consist of positive and negative electrodes (both sources of chemical reactions) separated by an electrolyte, which enables ion transfer between the two electrodes. The stored (chemical) energy can be released by connecting the electrodes externally, starting the chemical reactions and thereby liberating electrons supplying the external circuit with (electrical) energy. Unlike single-use primary batteries in which the electrode materials are irreversibly changed during discharge, LIBs are secondary batteries which can be recharged using an applied electric current.

Conventional LIBs utilize graphite as negative electrode (anode – Li source).[7] Other possible anode materials are $Li_4Ti_5O_{12}$ (LTO)[8,9] and conversion/alloying materials such as Si and Sn[10-12]. The use of metallic Li as negative electrode is highly desired due to its superior energy density, however, Li metals form dendrites potentially short-circuiting the battery and thus strongly limiting its application. As positive electrode (cathode – Li sink), generally intercalation materials are used.[13] The most prominent options include layered oxides such as $LiCoO_2$ (LCO)[14], $LiNi_{1/3}Mn_{1/3}Co_{1/3}O_2$ (NMC)[15], and $LiNi_{0.8}Co_{0.15}Al_{0.05}O_2$ (NCA)[16], as well as the spinel $LiMn_2O_4$ (LMO)[17] and the olivine $LiFePO_4$ (LFP)[18]. High voltage cathode materials ($\geq$ 5 V vs. Li^+/Li) have been developed and intensively investigated in recent years, however, they are not compatible with the currently employed electrolytes composed of organic solvents or polymers with a dissolved Li-salt.[19–21]

Beside restricting the choice of electrode materials due to limited mechanical and electrochemical stability, the conventionally used organic electrolytes also cause safety issues. They are flammable and have a low thermal stability, potentially leading to fire accidents or even explosions.[22,23] Additionally, the toxicity of their decomposition products presents a concern for environment and health.[24] Overall, traditional LIBs suffer from severe safety issues and performance limitations caused by the employed electrolytes. It is therefore of uttermost interest to replace the used organics by more stable inorganic solid ion conductors.[25] The use of such solid electrolytes is crucial to enable future battery concepts like all-solid-state batteries with superior energy density and safety.

To be competitive with conventional LIBs, solid Li-ion conductors must meet several criteria[26-30]:

- High ionic conductivity (above 10^{-4} S cm^{-1} at room temperature)
- Negligible electronic conductivity (Li-ion transference number close to unity)
- Wide electrochemical stability window (preferably 0–5 V vs. Li^+/Li)

- Good chemical compatibility with electrode materials
- Good mechanical and thermal stability
- Simple fabrication
- Low cost and environmental friendliness

A variety of inorganic solid Li-ion conductors have been considered for use in all-solid state batteries.[25,27,31,32] Among the most prominent options are oxides with NASICON (sodium super ionic conductor) structure, in particular $LiM_2(PO_4)_3$ (M = Ge, Zr or Ti), as well as perovskite-type $Li_{3x}La_{2/3-x}TiO_3$ (LLTO) and sulfide-type materials such as $Li_2S–P_2S_5$.[27] While some of the proposed solid electrolytes exhibit very promising properties, the performance of batteries based on these inorganic ion conductors is still inferior to that of commercially available LIBs.[27] Several challenges still remain, such as poor electrolyte/electrode interface, instability in ambient environment, flexibility concerns, and poor cycling stability.[27,28,30,33]

One of the most promising solid Li-ion conductors is the Li stuffed garnet $Li_7La_3Zr_2O_{12}$ (LLZO), which was first reported by Murugan et al.[34] in 2007. Beside its high Li-ion conductivity (up to 10^{-3} S cm^{-1} at ambient temperature), LLZO also features chemical stability against elemental Li, enabling its use in Li-metal batteries.[2,29,34,35]

Pure LLZO crystalizes in two different modifications: a low-conductivity tetragonal polymorph (ionic conductivity in the 10^{-6}–10^{-5} S cm^{-1} range[36–38]), generally stable at room temperature, and a high-temperature cubic polymorph with superior conductivity behavior. The phase transition from the tetragonal to the cubic structure occurs at approx. 645 °C for pristine LLZO not exposed to humidity,[39] however, at ambient conditions the phase change can already been observed between 100–200 °C.[39,40]

Tetragonal LLZO has a garnet-related structure with a space group *I*41/*acd* (No. 142) and a framework composed of two types of dodecahedral LaO_8 and octahedral ZrO_6 (Figure 1.02a).[36] Three crystallographic sites in the interstices of this framework are occupied by Li atoms: the tetrahedral 8*a* sites and the distorted octahedral 16*f* and 32*g* sites.[36] Cubic LLZO shows the space group $Ia\bar{3}d$ (No. 230) and a garnet framework structure composed of dodecahedral LaO_8 and octahedral ZrO_6 (Figure 1.02b).[41] Li atoms are located at three interstitial positions: tetrahedral 24*d* as well as the octahedral 48*g*/96*h* sites.[42,43] The displaced (off-centered) 96*h* sites are evolved from the distortion of 48*g* sites due to Li^+-Li^+ repulsion (i.e., the short 24*d*-48*g* distance introduces a Coulomb repulsion that displaces Li ions to the 96*h* sites).[44] The Li atoms are arranged in a three-dimensional network structure with short Li-Li distance, which might be related to the high ionic conductivity of the garnet.[41] In contrast to the tetragonal

modification, the Li-sites are only partially occupied in cubic phase, which is also considered as possible reason for the superior ionic conductivity of cubic LLZO.[29,40]

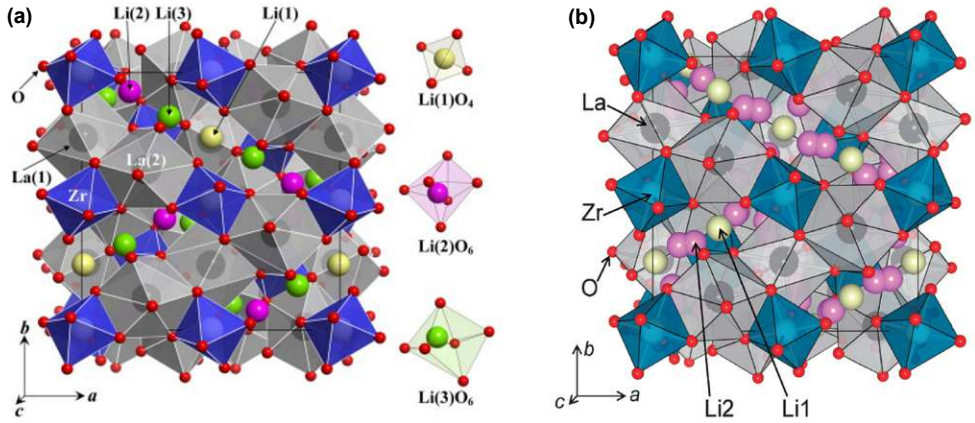

Figure 1.02: (a) Crystal structure of tetragonal $Li_7La_3Zr_2O_{12}$. Li atoms fully occupy the tetrahedral 8a (Li1, yellow) and the distorted octahedral 16f (Li2, purple) and 32g (Li3, green) sites. Reprinted from Ref.[36]. (b) Crystal structure of cubic $Li_7La_3Zr_2O_{12}$. Li atoms partially occupy the tetrahedral 24d (Li1, yellow) as well as the octahedral 96h (Li2, purple) and 48h (located between two adjacent Li2, not shown) sites. Reprinted from Ref.[41].

While for pure LLZO only the tetragonal structure is stable at room temperature, cubic LLZO can be stabilized by substitution of aliovalent ions.[34,36,41,45] The substitution introduces vacancies into the Li sublattice due to charge compensation, reducing the free energy advantage that comes with complete ordering and ultimately leading to a transition to cubic symmetry.[46] The first substitution element successfully used for the stabilization of cubic LLZO was Al, which was unintentionally incorporated into the LLZO lattice by using Al_2O_3 crucibles during the synthesis.[37,40] Since Al occupies the Li sites, this substitution (Al^{3+} → 3 Li^{+}) results in the formula unit $Li_{7-3x}Al_xLa_3Zr_2O_{12}$.[47] After the discovery of the stabilizing effect of Al, numerous elements substituting the Li, La, or Zr site have been reported. The various substitution elements are summarized Table 1.01. For Ga and Ta stabilized LLZO, a total ionic conductivity above 10^{-3} S cm^{-1} has been achieved.[48]

Table 1.01: Substitution elements stabilizing cubic LLZO at room temperature.

Site	Substitution element	Ref.
Li	Al^{3+}, Fe^{3+}, Ga^{3+}, Ge^{4+}	49–53, 54, 52,55,56, 57
La	Ca^{2+}, Sr^{2+}, Ce^{4+}	58, 59, 60
Zr	Mg^{2+}, Cr^{3+}, Gd^{3+}, Sc^{3+} Y^{3+}, Nb^{5+}, Sb^{5+}, Ta^{5+}, Ti^{5+}, Mo^{6+}, Te^{6+}, W^{6+}	61, 61, 62, 61, 63, 64, 65, 44,50,52,66,67, 68, 69, 70, 71

A lot of research has focused on LLZO in recent years, and knowledge became available on the ideal synthesis route, degradation phenomena, maximizing ionic conductivity, conduction paths, etc.[43,53,55,72–83] However, many aspects are still not understood and several key challenges remain. For example, the instability of LLZO in ambient atmosphere (due to moisture and CO_2) as well as interfacial issues could limit the application of LLZO in all-solid-state batteries.[30,84] To address these open questions, a deeper understanding of the garnet properties is necessary, which can only be achieved via thorough analysis of the material. While the electrochemical behavior, morphology, and structure of LLZO is usually investigated in detail,[40,43,85,86] most studies pay very little attention to other aspects like the chemical composition of the material. Accordingly, crucial information to truly understand the material properties of LLZO garnets is still missing.

In this work, several key properties of LLZO are investigated by combining electrochemical measurements with chemical analysis techniques. In Chapter 2, a novel method for spatially resolved stoichiometry determination of LLZO via laser ablation inductively coupled plasma optical emission spectroscopy (LA-ICP-OES) is presented. The method is used to investigate LLZO polycrystals, revealing strong variations in the local chemical composition of individual samples. To investigate the impact of these stoichiometry variations, the measurements are combined with local conductivity measurements via microelectrode electrochemical impedance spectroscopy (ME-EIS) in Chapter 3. Correlation analysis between local chemical composition and local ionic conductivity are performed, gaining valuable insights in the conductivity behavior of LLZO.

In Chapter 4, the electrochemical stability of LLZO single crystals is investigated by combining various electric field stress experiments with subsequent electrochemical, chemical, and structural analysis. The performed ME-EIS, scanning electron microscopy (SEM), laser-induced breakdown spectroscopy (LIBS), laser ablation inductively coupled plasma mass spectrometry (LA-ICP-MS), and microfocus x-ray diffraction (XRD) measurements reveal significant material changes caused by the applied field stress, questioning the compatibility of LLZO with high voltage cathode materials.

Lastly, the Li^+/H^+ exchange behavior of LLZO is investigated in Chapter 5. For that purpose, LLZO samples were immersed in water and composition changes subsequently analyzed using ICP-OES as well as LIBS depth profiling. The experiments show significantly increased H^+ incorporation for polycrystalline samples compared to single crystals, indicating enhanced H^+ diffusion along the grain boundaries of the material.

2 Spatially resolved stoichiometry determination of $Li_7La_3Zr_2O_{12}$ solid-state electrolytes using LA-ICP-OES

The study presented in this chapter has also been published as a scientific paper in "Journal of Analytical Atomic Spectrometry"[87].

2.1 Introduction

Although a lot of research has focused on LLZO in recent years, the reproducible synthesis of garnets with high Li-ion conductivity remains challenging. For example, pellets with the same nominal composition prepared at different laboratories show differences in ionic conductivity of more than an order of magnitude.[29,88] Furthermore, local conductivity variations have been reported within one and the same sample.[89] The reasons for these variations are still not completely understood, however, they probably relate to differences in sample stoichiometry.[88] Since synthesis of LLZO normally involves high-temperature treatment, partial loss of Li_2O due to evaporation cannot be avoided.[74,90] In addition, Al incorporation from the commonly used Al_2O_3 crucibles further changes the sample composition.[37,40,74] Thus, determination of the chemical composition after the synthesis is crucial for reliable LLZO investigation.

Chemical analysis of Al stabilized LLZO pellets is mostly performed using sample-digestion and subsequent inductively coupled plasma optical emission spectroscopy (ICP-OES) or inductively coupled plasma mass spectrometry (ICP-MS) analysis.[36,37,53,90,91] While this approach enables reliable determination of the bulk composition, it requires time consuming sample preparation and does not provide any spatially resolved information. For elemental surface analysis of LLZO, mostly energy-dispersive x-ray spectroscopy (EDX) is used.[36,40,51,74,92] This method enables the determination of the Al, La, and Zr distribution, but its use is strongly limited by its incapacity to detect Li. Other applied surface analysis techniques are x-ray photoelectron spectroscopy (XPS)[75,82,83,93,94] and secondary ion mass spectrometry (SIMS)[57,73,95,96], however, both techniques usually only provide semi-quantitative information and are limited in terms of sampling depth (i.e., surface effects and not bulk properties are investigated). Additionally, the excellent spatial resolution of SIMS with spot sizes down to the sub-µm range makes the analysis of macroscopic areas very time-consuming.

Also LIBS has been used for the elemental analysis of LLZO. Depth profiles[77], 2D cross-sectional maps[74,75,97] and even 3D distribution images[76] have been recorded, showing that LIBS is a very powerful tool for the investigation of sample inhomogeneity close to the sample

surface. In these experiments, the bulk composition of the samples (determined by ICP-OES) served as standard for signal quantification, assuming that the chemical composition is constant over the whole sample after reaching a specific sampling depth. Since previous studies[88] revealed macroscopic inhomogeneities in Al stabilized LLZO pellets, this assumption does not seem to be correct for all samples, questioning the suitability of this quantification approach. Overall, there is still need for a laterally resolved method for LLZO analysis that provides reliable quantitative information.

A promising option for the chemical analysis of LLZO is coupling of ICP-MS or ICP-OES to laser ablation (LA). While the use of LA prevents time-consuming sample digestion and dilution, the subsequent analysis of the generated aerosol with ICP-OES or ICP-MS allows detection of all LLZO constituents including Li. Furthermore, these methods provide spatially resolved information and have already been used for the quantitative determination of bulk, trace and ultra-trace elements in various advanced materials including ceramics.[98,99] While neither LA-ICP-MS nor LA-ICP-OES is widely adapted in the field of LIBs, both techniques have been successfully applied for the characterization of electrode materials.[100–104]

Since LA suffers from sample-dependent ablation behavior and elemental fractionation, reliable signal quantification is challenging. However, these issues can be overcome by using matrix-matched calibration standards in combination with appropriate signal normalization strategies.[105]

The aim of this study is to develop a method for the laterally resolved analysis of Al stabilized LLZO ($Li_{7-3x}Al_xLa_3Zr_2O_{12}$) by using LA-ICP-OES. To ensure reliable signal quantification, matrix-matched standards were prepared and characterized by sample digestion and subsequent liquid ICP-OES measurement. These standards were used to conduct LA-ICP-OES calibrations, and the obtained results were compared with parallel LA-ICP-MS measurements. To show the capabilities of the developed method, quantitative distribution images of an Al stabilized LLZO pellet were recorded.

2.2 Experimental

2.2.1 LLZO synthesis

$Li_{7-3x}Al_xLa_3Zr_2O_{12}$ garnets with intended Al contents ranging from x = 0.00 to x = 0.40 were synthesized using a high-temperature sintering route based on the procedure described by Wagner et al.[106]. Li_2CO_3 (≥ 99 %, Merck, Germany), Al_2O_3 (≥ 99.5 %, Sigma-Aldrich, Germany), La_2O_3 (≥ 99.99 %, Carl Roth, Germany), and ZrO_2 (≥ 99 %, Carl Roth, Germany) were used as starting materials. The reagents were weighed in the intended stoichiometric proportions with an excess of 10 m% Li_2CO_3 to compensate Li_2O loss during sintering. The powders were ground and mixed in an agate mortar under addition of isopropyl alcohol and subsequently cold-pressed into pellets using a uniaxial press. The resulting pellets were put into an alumina crucible and placed on a pellet of pure LLZO to avoid undesired Al contamination from the crucible. The samples were heated to 850 °C with a rate of 5 °C min^{-1} and calcinated for 4 h. After cooling down, the resulting pellets were again ground in an agate mortar and ball-milled for 1 h under isopropyl alcohol (FRITSCH Pulverisette 7, Germany, 800 rpm, 2 mm ZrO_2 balls). After drying, the powders were cold-pressed, and the resulting pellets were again put into an alumina crucible. The samples were placed between two pellets of pure LLZO to avoid unwanted incorporation of Al^{3+} from the crucible as well as formation of extra phases due to loss of Li_2O during the final sintering step. The pellets were sintered for 6 h at 1230 °C in a muffle furnace using air atmosphere and a heating rate of 5 °C/min.

2.2.2 Preparation of matrix-matched standards

A series of $Li_{7-3x}Al_xLa_3Zr_2O_{12}$ standards was prepared from synthesized LLZO pellets with intended Al contents of x = 0.00, 0.05, 0.10, 0.15, 0.20, 0.25, 0.30, 0.35, 0.40. To ensure homogeneity, the pellets were crushed and ground in an agate mortar. About 1 g of each of the obtained powders were transferred into a flexible silicone rubber mold and cold pressed using a mechanical isostatic press (Paul-Otto Weber, Germany) at a pressure of 300 MPa. To remove potential surface contaminations caused by the pressing mold, the sample surfaces were cleaned using P2000 SiC grinding paper (Struers, Denmark). The procedure resulted in pressed pellets with about 8 mm diameter and about 5 mm thickness.

2.2.3 Bulk analysis via liquid ICP-OES

The prepared LLZO standards were characterized using liquid ICP-OES analysis. For that purpose, parts of the powders that were used to press the standard pellets were digested. Borax fusion was used for sample digestion: The sample powders were transferred into Pt crucibles, mixed with a 16-fold excess of sodium tetraborate (anhydrous, ≥ 98 %, Merck, Germany), and heated to 1000 °C for 5 h. The digestion was replicated three times for each standard (50 mg per replicate). Additionally, blank digestions without sample were performed to check for potential contaminations caused by the sample pre-treatment. After cooling down, the solidified fusions were dissolved using an 8/1/40 (v/v/v) mixture of hydrochloric acid (37 m%, Emsure®, Merck, Germany), hydrofluoric acid (40 m%, Emsure®, Merck, Germany), and deionized water (18.2 MΩ cm^{-1}) obtained by a Barnstead™ Easypure ™ II (Thermo Fisher Scientific, USA). The prepared solutions were diluted to a final LLZO concentration of about 18 mg kg^{-1} using a 1/100 (v/v) dilution of nitric acid (65 m%, Emsure®, Merck, Germany).

For signal quantification, univariate calibration using certified single element ICP-standard solutions (Certipur®, Merck, Germany) was used. Al, La, Li, and Zr standards were mixed to obtain elemental ratios corresponding to a $Li_{6.4}Al_{0.2}La_3Zr_2O_{12}$ sample. By diluting the standard mixture, calibration standards with an LLZO concentration ranging from 3.6 to 36 mg kg^{-1} were prepared. An Eu ICP-standard solution (Certipur®, Merck, Germany) was added to all standard and sample solutions to a final concentration of 0.2 mg kg^{-1} and acted as internal standard for the analysis.

An iCAP 6500 RAD (Thermo Fisher Scientific, USA) equipped with an echelle-type monochromator and a charge injection device (CID) detector was used for the ICP-OES analysis. For data acquisition, Qtegra software provided by the manufacturer of the instrument was used. Introduction of the samples was performed using an ASX-520 autosampler (CETAC Technologies, USA), PTFE tubing, and a sample introduction kit consisting of a conventional Meinhard high-solids quartz nebulizer and a quartz cyclone spray chamber without ascension tube. A plasma torch containing a quartz injector tube with 1.5 mm inner diameter was used for the analysis. Detailed information about the used instrument parameters can be found in Table 2.01.

For each analyte, the two most sensitive and non-interfered emission lines were recorded. Only one emission line per element was used for quantification, the other one was used for quality control (i.e., check for spectral interferences). In case of Al only one emission line with sufficient signal intensity was accessible (396.152 nm). Since this line suffers from spectral interference caused by a minor Zr emission line, interference correction was applied. For that

purpose, Zr single element standard solutions with various concentrations were analyzed to determine the impact of the interference.

For the compensation of differences in sample introduction and instrumental drifts, internal standardization was used (i.e., all analyte signals were normalized to an Eu emission line). To further minimize errors in signal quantification, two additional measures were applied: (a) the calibration standards were measured not consecutively but separately between the samples and in random order and (b) the whole analysis was repeated three times. The analyte concentrations obtained by this threefold analysis were averaged for further data processing.

Table 2.01: Instrumental settings for bulk analysis via ICP-OES

	Thermo iCAP 6500 RAD	
RF power	1200 W	
Radial observation height	12 mm	
Plasma gas flow (Ar)	12 l min^{-1}	
Nebulizer gas flow (Ar)	0.8 l min^{-1}	
Auxiliary gas flow (Ar)	0.8 l min^{-1}	
Integration time	5 s	
Replicates per sample	5	
Purge pump rate	1.6 ml min^{-1}	
Sample flow rate	0.8 ml min^{-1}	
Analytical wavelengths		
Al	396.152 nm*△	
Eu (Internal standard)	281.396 nm (□)	381.967 nm (△)
La	333.749 nm□	412.323 nm*□
Li	610.362 nm△	670.784 nm*△
Zr	339.198 nm□	343.823 nm*□

* used for quantification
□/△ normalized to Eu 281.396/381.967 nm signal

2.2.4 LA-ICP-OES and -MS calibration

For all LA experiments, a NWR213 laser ablation system (ESI, USA) equipped with a frequency quintupled 213 nm Nd:YAG laser and a fast-washout ablation cell always positioned above the actual ablation site was utilized. The device was coupled to either ICP-OES or ICP-MS using PTFE tubing with 2 mm inner diameter. He was used as a carrier gas for cell washout, which was mixed with Ar make-up gas upon introduction into the plasma. Detailed information about the used instrumental settings can be found in Table 2.02.

Table 2.02: Instrumental settings LA-ICP-OES and -MS analysis

Laser ablation system	ESI NWR213	
Average fluence		
Pre-Ablation	2.50 J cm^{-2}	
Analysis	4.25 J cm^{-2}	
Laser diameter		
Pre-Ablation	250 µm	
Analysis	100 µm	
Scan speed		
Pre-Ablation	250 µm s^{-1}	
Analysis	100 µm s^{-1}	
Repetition rate	20 Hz	
Carrier gas flow (He)	0.6 l min^{-1}	
Make-up gas flow (Ar)	0.8 l min^{-1}	
ICP-OES instrumentation	Thermo iCAP 6500 RAD	
RF power	1200 W	
Radial observation height	12 mm	
Plasma gas flow (Ar)	12 l min^{-1}	
Auxiliary gas flow (Ar)	0.5 l min^{-1}	
Integration time	1 s	
Analytical wavelengths		
Al	309.271 nm	396.152 nm*
La	261.034 nm*	419.655 nm
Li	610.362 nm*	670.784 nm
Zr	257.139 nm*	274.256 nm
	* used for quantification	
ICP-MS instrumentation	Thermo iCAP Q	
RF power	1550 W	
Plasma gas flow (Ar)	14 l min^{-1}	
Auxiliary gas flow (Ar)	0.8 l min^{-1}	
Dwell time per isotope	10 ms	
Cones	Ni	
Mass resolution	$m/\Delta m = 300$	
Measured isotopes	^{7}Li, ^{27}Al, ^{90}Zr, ^{138}La	

For the LA-ICP-OES experiments, the same ICP-OES instrument as for the bulk analysis was used (see Section 2.2.3). In contrast to the liquid measurements, a plasma torch containing a corrosion-resistant ceramic injector tube was used. Data acquisition was performed using iTEVA software (v.2.8.0.96) provided by the manufacturer of the instrument. For each analyte, two emission lines were recorded, where one emission line was used for signal quantification and the other one was used for quality control. Compared to the liquid analysis, less sensitive La and Zr emission lines were selected to avoid detector saturation. Furthermore, the integration time was reduced to 1 s in order to allow fast monitoring of the transient signals provided in imaging experiments. Similar to the liquid measurements, interference correction for the Al 396.152 nm emission lines was applied. In order to determine the impact of the Zr interference, an Al-free YSZ single crystal (ZrO_2 stabilized with 9.5 mol% Y_2O_3, 5 mm × 5 mm × 0.5 mm, Crystec, Germany) was measured prior to the analysis using identical instrument setting.

In case of the LA-ICP-MS measurements, the LA system was coupled to a quadrupole ICP-MS instrument (Thermo iCAP Qc, ThermoFisher Scientific, Germany). For data acquisition, Qtegra software (v.2.10.3324.62) provided by the manufacturer of the instrument was used. Before every experiment, the measurement parameters concerning the MS instrumentation were optimized for maximum ^{115}In signal using a NIST 612 trace metals in glass standard (National Institute of Standards and Technologies, Gaithersburg, MD). Additionally, the oxide ratio was monitored via the $^{140}Ce^{16}O/^{140}Ce$ ratio, which was below 2.0% for all experiments.

LA-ICP-OES and -MS measurements were quantified using the prepared LLZO pellets as matrix-matched calibration standards. Analysis of these standards was performed using line scan ablation patterns with adjoining lines. Per standard, four laser patterns (each having an area of about 0.4 mm^2) were placed on different locations on the pellets. Each laser pattern was ablated three times. For further data processing, average values were calculated for each pattern. In order to remove potential surface contaminations (e.g., Li_2CO_3 due to air exposure[75]), a pre-ablation step consisting of a similar line scan patterns was applied prior to the analysis.

Two different calibration strategies were used for signal quantification. On the one hand, conventional univariate calibration in combination with the use of La as internal standard was applied, assuming equal La content and -distribution in all samples. Additionally, an internal standard-independent calibration strategy presented by Li et al.[107] was adapted for LLZO samples. Based on the consideration that the sum of all metal oxides in LLZO adds up to 100 m%, this approach uses the intensities of all measured analytes expressed as the corresponding

oxides (Al_2O_3, Li_2O, La_2O_3, ZrO_2) for signal normalization. The sample composition was calculated using the following Equations (2.01+2.02)

$$c^i_{sam} = \frac{100 \cdot I^i_{sam} \cdot l^i}{\sum_{k=1}^{N} (I^k_{sam} \cdot l^k)} \quad (2.01)$$

$$l^i = \sum_{j=1}^{n} \left(\frac{c^i_{rmj}}{I^i_{rmj}} \cdot \frac{c^i_{rmj}}{\sum_{j=1}^{n} c^i_{rmj}} \right) \quad (2.02)$$

where N = number of measured elements, n = number of reference materials used as external standard, c^i_{sam} = concentrations of analyte element i in the sample, c^i_{rmj} = concentrations of analyte element i in the reference material j, I^i_{sam} (I^k_{sam}) = Signal intensity (net count rate) of element i (k) in the sample, and I^i_{rmj} = Signal intensity (net count rate) of element i in the reference material j. Detailed information about this calibration strategy can be found in Ref.[107].

2.2.5 Elemental imaging

2D distribution images of an Al stabilized LLZO pellet with the nominal composition of $Li_{6.4}Al_{0.2}La_3Zr_2O_{12}$ were recorded using LA-ICP-OES. Prior to the analysis, the thickness of the pellet was reduced to about 250 µm using P500 SiC grinding paper (Struers, Denmark). The purpose of this was twofold: first, removing the surface near region ensures that the analysis investigates the bulk of the material. Second, a reduced sample thickness decreases the impact of composition variations perpendicular to the surface, ensuring that the average composition determined by the LA measurement (which one probes the sample surface) represents the bulk value of the whole pellet.

LA-ICP-OES settings described in the previous section were used for all measurements. To create elemental maps, line-scan ablation patterns with adjoining lines were used. A laser beam diameter of 100 µm and a scan speed of 100 µm s^{-1} were used, which, taking the washout-time of the ablation cell into consideration, results in images with a lateral resolution of 100 µm. As with the measurement of the calibration standards, a pre-ablation step for cleaning purposed (e.g., removing residues from SiC grinding paper) was also applied for the sample analysis.

Image processing was performed using the software ImageLab (v.2.41, Epina GmbH, Austria).

2.2.6 Validation approach

In order to control the accuracy of the quantitative LA-ICP-OES imaging analysis, the average sample stoichiometry derived from distribution maps were compared with the bulk chemical composition determined by sample digestion and subsequent liquid ICP-OES measurement. The bulk analysis was performed after the imaging experiment using the procedure described in Section 2.2.3. Before the digestion, the pellet (with a total mass of 30 mg) was crushed and ground to obtain a homogeneous powder. The digestion was replicated three times, using about 10 mg sample each.

2.3 Results and discussion

2.3.1 Standard characterization

Obtaining suitable reference materials is a crucial aspect for reliable and accurate quantification of LA-ICP-OES and -MS measurements. As for most novel materials, LLZO certified reference materials are not commercially available and in-house standard preparation is therefore necessary. Since calibration standards are a limiting factor for the accuracy of an analysis, it is important to ensure careful preparation as well as high-precision characterization of the material.

Figure 2.01 shows the standard preparation and characterization process schematically. LLZO pellets with different doping content ranging from 0.0 to 0.4 Al per formula unit (pfu) were synthesized using a conventional high temperature sintering route. Since the high temperature is likely to affect the chemical composition of the pellets (e.g., due to loss of Li_2O or diffusion processes), leading to sample inhomogeneities, the obtained pellets are not suitable for direct use as standard. To overcome this issue, the sintered pellets were crushed and ground and the obtained powders were subsequently pressed into pellets. This results in LLZO pellets with constant chemical composition that are suitable for use as matrix-matched standard for LA-ICP-OES measurements.

For the characterization of the obtained standards, the remaining powders that were not consumed by the pressing of the standards were used. The samples were transferred into liquid form using borax fusion and the obtained liquids analyzed via ICP-OES. To obtain results as accurate as possible, multiple measures were applied: (a) three replicate digestions for each sample, (b) internal-standard corrections using Eu, (c) random measuring sequence of standards and samples, (d) threefold repeat of the whole measurement including calibration, and (e) interference correction for the main Al emission line (396.152 nm, interfered by a minor Zr

line). Although the Zr interference is rather weak and might not be relevant for samples with high doping contents, correcting it is still considered necessary to prevent inaccurate results for samples with low Al concentration.

The determined bulk compositions of all standards are listed in Table 2.03. The results show significant but reasonable deviations from the intended values. The average Zr/La atomic ratio is 0.650, which is close to the expected value (0.667). Also the Al/La atomic ratios agree well with the intended ratios, except for the nominally Al-free standard. In this case, the standard shows a much higher Al/La ratio of 0.025, which indicates Al incorporation during the sintering in the Al_2O_3 crucibles. The reason that this can only be observed for the nominally Al-free sample could be related to the fact that that Al-substitution stabilizes the cubic LLZO modification.[37,40,85]

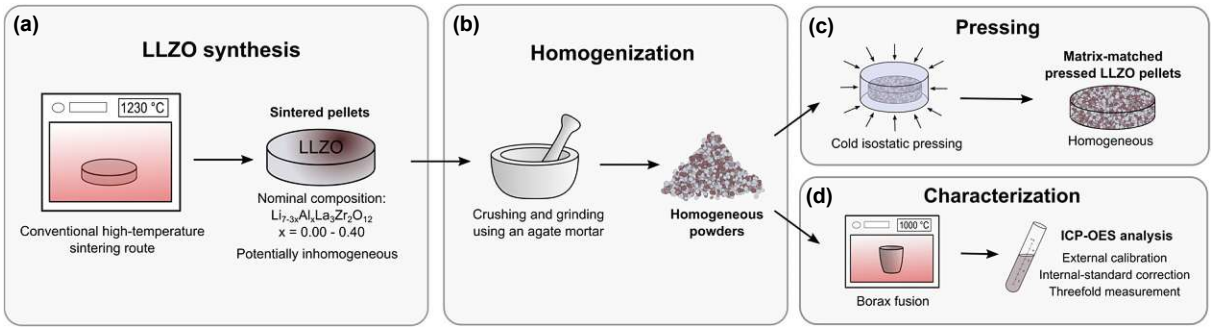

Figure 2.01: Preparation and characterization of matrix-matched LLZO standards. (a) LLZO synthesis leading to sintered pellets, followed by (b) crushing and grinding of the pellets to ensure homogeneity. The resulting powders were used for (c) pressing them into pellets to obtain homogenous standards and (d) characterizing the standards using borax fusion and ICP-OES analysis.

Table 2.03: Chemical composition of the prepared standards (nominally $Li_{7-3x}Al_xLa_3Zr_2O_{12}$) determined via ICP-OES analysis. The stated measurement uncertainties correspond to the confidence intervals of the mean values derived from the measurement of three replicate digestions (α = 0.10, n = 3). The nominal atomic ratios are displayed in brackets. The analysis confirms significant deviations from the intended stoichiometry, especially in case of Li.

x	Al/La	Li/La	Zr/La	Formula*
0.00	0.025 ± 0.006 (0.000)	2.17 ± 0.04 (2.33)	0.638 ± 0.003 (0.667)	$Li_{6.51}Al_{0.08}La_3\ Zr_{1.91}O_{11.7}$
0.05	0.013 ± 0.008 (0.017)	2.23 ± 0.10 (2.28)	0.651 ± 0.006 (0.667)	$Li_{6.69}Al_{0.04}La_3\ Zr_{1.95}O_{11.8}$
0.10	0.029 ± 0.007 (0.033)	2.18 ± 0.03 (2.23)	0.650 ± 0.003 (0.667)	$Li_{6.55}Al_{0.09}La_3\ Zr_{1.95}O_{11.8}$
0.15	0.048 ± 0.004 (0.050)	2.17 ± 0.04 (2.18)	0.653 ± 0.005 (0.667)	$Li_{6.52}Al_{0.15}La_3\ Zr_{1.96}O_{11.9}$
0.20	0.066 ± 0.004 (0.067)	2.14 ± 0.06 (2.13)	0.652 ± 0.004 (0.667)	$Li_{6.42}Al_{0.20}La_3\ Zr_{1.96}O_{11.9}$
0.25	0.083 ± 0.003 (0.083)	2.10 ± 0.06 (2.08)	0.651 ± 0.005 (0.667)	$Li_{6.29}Al_{0.25}La_3\ Zr_{1.95}O_{11.9}$
0.30	0.097 ± 0.004 (0.100)	2.06 ± 0.06 (2.03)	0.646 ± 0.003 (0.667)	$Li_{6.19}Al_{0.29}La_3\ Zr_{1.94}O_{11.9}$
0.35	0.116 ± 0.008 (0.117)	2.02 ± 0.05 (1.98)	0.653 ± 0.003 (0.667)	$Li_{6.07}Al_{0.35}La_3\ Zr_{1.96}O_{12.0}$
0.40	0.137 ± 0.006 (0.133)	2.00 ± 0.03 (1.93)	0.655 ± 0.004 (0.667)	$Li_{6.00}Al_{0.41}La_3\ Zr_{1.96}O_{11.9}$

* Calculated, based on atomic ratios. Oxygen contents are estimated from charge balance considerations.

The strongest deviations from the intended values can be observed for the Li/La atomic ratio. This is not surprising, since it is known that Li_2O evaporates during sintering, changing the Li content of the pellet. While usually Li excess is used in the starting material mixture to compensate this phenomenon,[34,37,40,41] the assumed amount of lost Li might not be correct. Interestingly, the Li/La ratio is lower than desired for the standards with low Al contents, and higher than intended for the Al-rich standards. This means that less Li was lost during the synthesis of samples with a higher Al content, indicating that the Li_2O loss depends on the Al content. Overall, the results highlight the importance of monitoring the chemical composition of LLZO samples after high-temperature treatment, not only if they are used as standards, but also for general purposes.

2.3.2 LA-ICP-OES calibration

After the preparation and characterization of matrix-matched LLZO standards, they were used for the calibration of the LA-ICP-OES experiments. For this purpose, each of the pellets was analyzed using multiple ablation patterns.

Figure 2.02 shows typical calibrations obtained by such an experiment. Conventional univariate calibrations are displayed where signal normalization was preformed using La as internal standard. A distinct linear correlation and an excellent coefficient of determination (R^2 = 0.9988) can be observed for the Al signal (Figure 2.02a). The limit of detection (LOD) of the analysis (calculated based on the slope and the standard deviation of the response of the calibration curve) is 0.049 m%, which shows that the selected measurement parameters offer sufficient sensitivity for an accurate analysis of the Al content, even for the lowest dopant levels.

In case of Li the coefficient of determination is lower (R^2 = 0.9628), however, also here the signal shows a clear correlation (Figure 2.02b). It is important to notice that in case of Li the covered mass range is very narrow (highest and lowest standard only differ by 17 % relatively) and obtaining a suitable calibration therefore difficult. This once more highlights the importance of a high-precision analysis for this material system.

Beside the LA-ICP-OES calibration, Figure 2.02 also displays the results of analogue LA-ICP-MS measurements for comparative purposes. While the calibration shows similar quality in case of Al (Figure 2.02c), no significant correlation at all can be observed for the Li signal when ICP-MS is used for the analysis (Figure 2.02d). This is mostly likely caused by the fact that the measurement of light elements such as Li suffers severely from matrix-induced suppression in the ion beam,[108] limiting the precision of the ICP-MS analysis. The lack of

precision in case of LA-ICP-MS confirms that LA-ICP-OES is more reliable for the measurement of Li and is therefore the preferred choice for the analysis of LLZO.

An important aspect for reliable signal quantification is the use of appropriate signal normalization, especially if the used calibration standards potentially show different ablation behavior due to differences in the mechanical properties (ablation rate compact samples vs. pressed standards). The most straightforward normalization approach for the analysis of LLZO is the use of La as internal standard, assuming that the same amount of La is present in all standards and samples. This assumption is most likely valid, since La_2O_3 is very heat resistant (melting point > 2300 °C) and occurrence of La loss during the LLZO synthesis is therefore very unlikely. The performed experiments confirm this, since good LA calibrations are obtained when using La for signal normalization (cf. Figure 2.02). However, assuming a constant La content introduces an additional uncertainty, potentially decreasing the precision of the analysis. Furthermore, it is not possible to determine the full stoichiometry of LLZO samples using that approach, since the La content is not investigated.

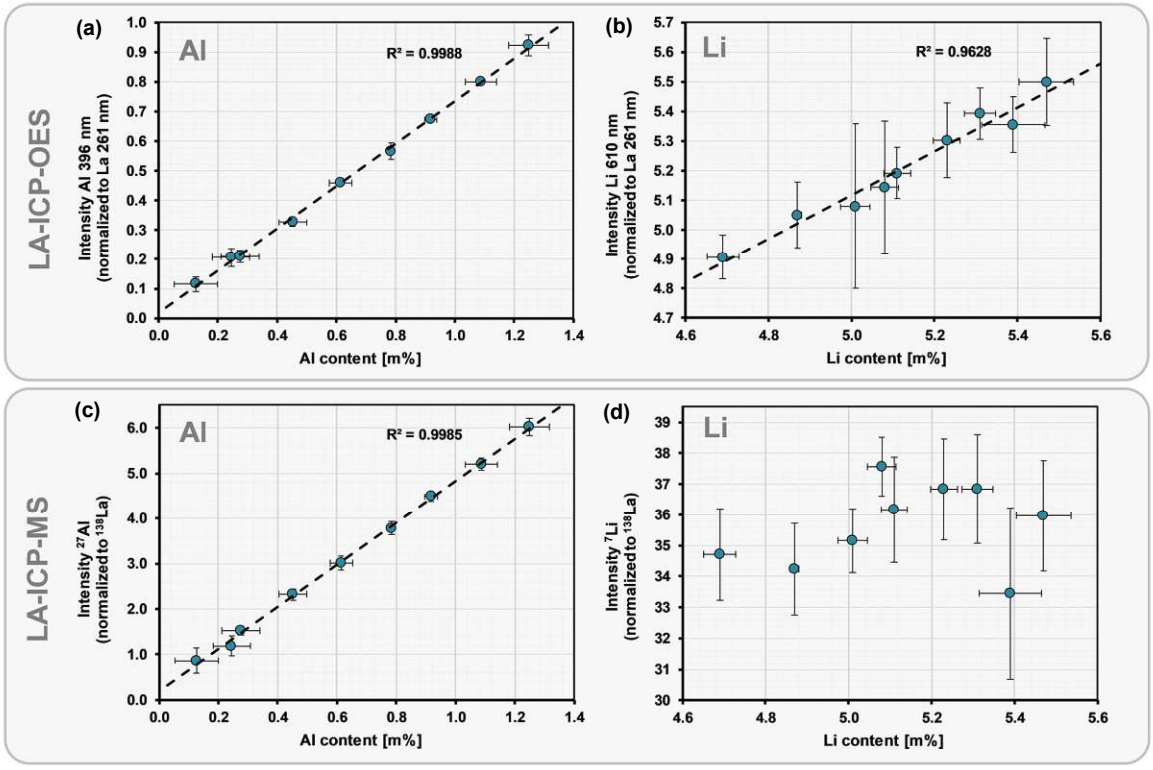

Figure 2.02: LA-ICP-OES calibration of the Al (a) and Li (b) signal as well as analogue LA-ICP-MS measurements (c+d). A conventional univariate calibration strategy is applied, where La is used as internal standard for signal normalization. The vertical error bars represent the confidence intervals of the mean values derived from the measurement of multiple ablation patterns (α = 0.10, n = 4); the horizontal error bars represent the confidence intervals of the standard characterization via liquid ICP-OES (α = 0.10, n = 3). The plots confirm LA-ICP-OES is superior to LA-ICP-MS for the determination of Li, while similar results are obtained for the analysis of Al.

To overcome this issues, an adapted version of internal standard-independent calibration strategy presented by Li et al.[107] was applied. This approach is based on the consideration that the sum of all metal oxides in LLZO adds up to 100 m% and uses intensities of all measured analytes for signal normalization. Since the mass fractions of all cations (including La) are determined, this calibration strategy enables the calculation of all cation atomic ratios, giving access to the complete stoichiometry of the material.

To determine the accuracy of this quantification strategy, a cross-validation approach was used: In a first step, the stoichiometry (expressed as atomic ratios) of each standard is determined using all other standards for the calibration of the measurement. After that, the obtained values are compared with the corresponding target values (derived from the standard characterization via ICP-OES). Figure 2.03 shows the results of this cross-validation. In general, excellent agreement between measured and target stoichiometry can be observed. The average deviations for the Al/La, Li/La, and Zr/La atomic ratio are 3.1 %, 1.1 %, and 0.5 %, respectively. Solely the Al/La ratio for the sample with the lowest Al content shows a significantly larger deviation. The reason for this is the low absolute Al concentration in the material, which leads to low signal intensity and therefore large relative measurement uncertainties. This is in agreement with the relatively large error bars for the Al-poor standards. Overall, the measurements confirm that the internal standard-independent calibration strategy based on 100 m% is reliable for the analysis of LLZO samples.

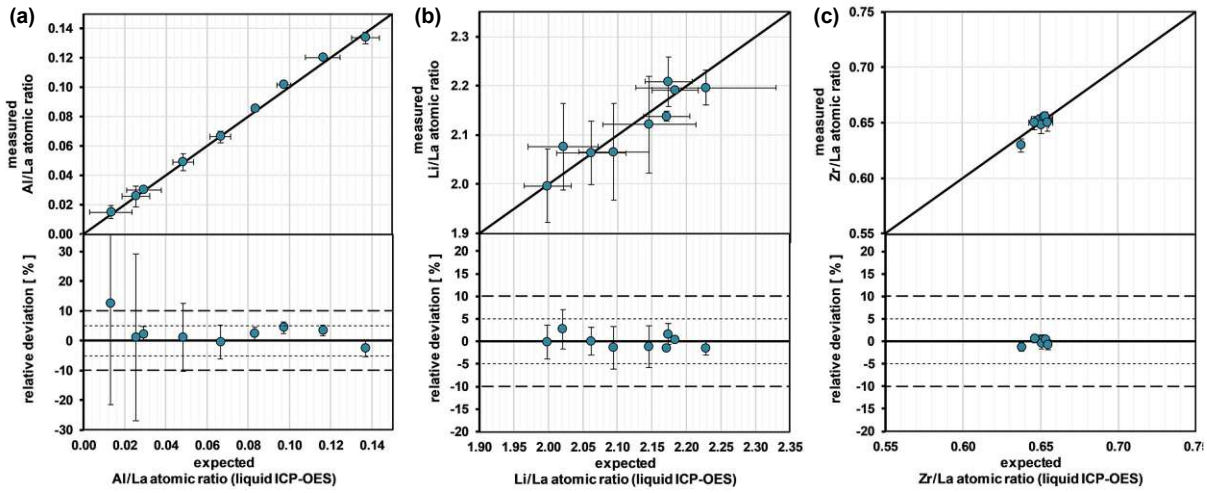

Figure 2.03: Cross-validation of a LA-ICP-OES calibration using 100 m% normalization. Predicted (a) Al/La, (b) Li/La, and (c) Zr/La atomic ratios for each standard vs. corresponding target values (determined via liquid ICP-OES). In addition, the relative deviations are shown for a better visualization of the differences. The vertical error bars represent the confidence intervals of the mean values derived from the measurement of multiple ablation patterns (α = 0.10, n = 4); the horizontal error bars represent the confidence intervals of the standard characterization via liquid ICP-OES (α = 0.10, n = 3). The plots show an excellent agreement with a relative deviation below 5% for all Li/La and Zr/La as well as most Al/La ratios.

2.3.3 Quantitative LLZO imaging

Using the developed quantification strategy, an Al stabilized LLZO pellet with a nominal composition of $Li_{6.4}Al_{0.2}La_3Zr_2O_{12}$ was investigated. For that purpose, a 2D distribution imaging experiment covering the whole pellet was performed.

Since the aim of this experiment is to investigate the bulk of the material, two measures to avoid influences of surface effects were applied: first, near surface layers that could be affected by Al-enrichment[76] or other surface-related composition variations were mechanically removed. Second, a pre-ablation step was applied directly before the measurement, ablating ca. 2 µm material and removing potential surface alterations caused by the grinding process or contact with air (e.g. Li_2CO_3 formation[75]).

The imaging experiment resulted in distribution maps with a lateral resolution of 100 µm in both vertical and horizontal direction. The ablation depth of the analysis was approx. 3 µm. Due to use of the 100 m% normalization strategy, the mass fractions of all cations (Al, La, Li, and Zr) were obtained by the analysis. These mass fractions were converted into the corresponding atomic ratios, defining the stoichiometry of the material.

Figure 2.04 shows the obtained distribution images. The maps represent the (locally resolved) sample stoichiometry expressed in form of atomic ratios (Al/La, Li/La, and Zr/La). Significant composition differences between the inner and the outer part of the pellet can be observed. For a better visualization of these variations, the atomic ratios along a selected cross section are plotted next to the corresponding images. To verify that the selected cross-section is representative for the sample, additional cross-sections were investigated, leading to similar results (not shown). As expected, the sample shows a constant Zr/La atomic ratio across the whole pellet (see Figure 2.04a). Since it is extremely unlikely that the Zr and La content changes in the same ratio, this confirms that Zr as well as La are evenly distributed within the pellet. This is not surprising, since both elements are not prone to evaporation of their oxide, and, moreover, their crystal sites are not affected by Li. Hence, they are most likely not changed by the sintering process.

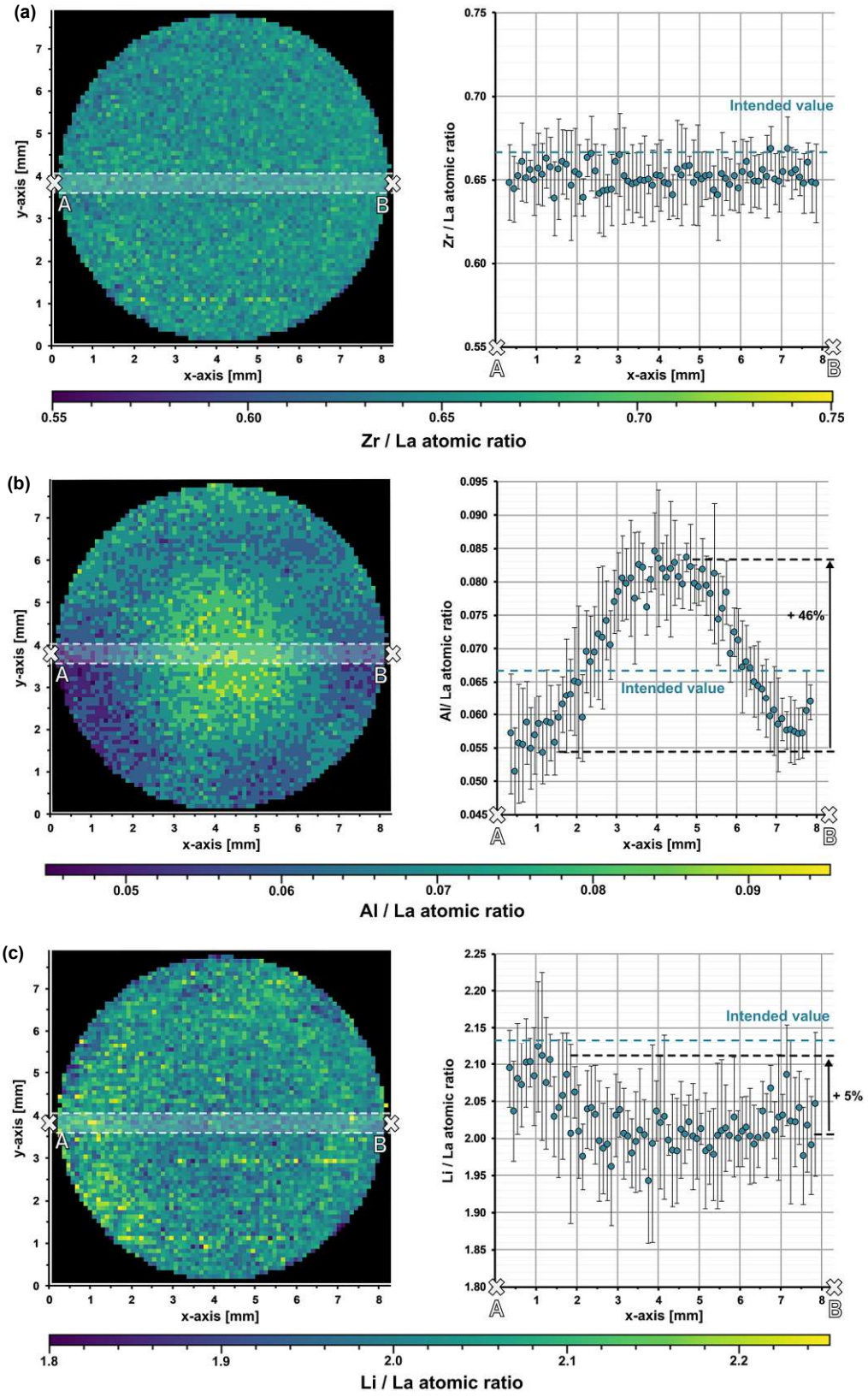

Figure 2.04: Quantitative LA-ICP-OES imaging of a LLZO pellet with the nominal composition $Li_{6.4}Al_{0.2}La_3Zr_2O_{12}$. (a) Al/La, (b) Li/La, and (c) Zr/La distribution maps and corresponding atomic ratios along the cross-section from A to B. Each data point in the cross-section plot represents the mean value of five pixels adjacent in the y-direction; the error bars represent the corresponding confidence intervals (α = 0.10, n = 5). The images show a strong Al-enrichment in the middle of the pellet as well as small but significant variations of the Li content.

In contrast to that, significant Al and Li variations are observed. The Al/La map shows a strong Al-enrichment in the inner part of the pellet with an increase of Al/La atomic ratio up to 46 % compared to the outer part of the sample (see Figure 2.04b). Considering the fact that Al replaces Li in the LLZO crystal lattice, the Li distribution image should show an opposing trend. Indeed, the Li/La image indicates a higher Li content in the outer part of pellet (see Figure 2.04c), however, the differences are much smaller and hardly visible in the map. The reason why the variations are much harder to see in case of Li is the fact that LLZO contains a relatively high amount of Li. The changes of the Li content that are induced by Al-doping are therefore relatively small, making the variations less pronounced. Interestingly, the images show that the Li content is significantly lower than intended, indicating that more Li than expected was lost during the sintering process.

The obtained distribution images demonstrate the existence of stoichiometry variations within the bulk of LLZO samples. These composition changes are of great relevance since they might affect the electrochemical behavior of LLZO, which is crucial for its application as solid electrolyte material. Possible correlations were investigated in Chapter 3, where several LLZO pellets were analyzed using the presented method and the findings compared with local conductivity measurements.

2.3.4 Method validation

In addition to visualizing the analyte distributions, the recorded images were used to determine the mean sample stoichiometry. For that purpose, the values of all measured pixels were averaged. Under the assumption that the pellet does not show composition changes perpendicular to the surface, this represents the average stoichiometry of the analyzed pellet. This assumption is valid since (a) the investigated pellet was very thin (the thickness of the pellet was reduced to approx. 250 µm, see Experimental) and (b) the distribution maps revealed that the stoichiometry changes are on a macroscopic rather than a microscopic scale.

In a further step, the bulk composition of the pellet was determined via conventional ICP-OES analysis. For that purpose, the remaining pellet was analyzed using the same procedure as for the characterization of the standard powders.

In order to validate the accuracy of the LA measurement, the average stoichiometry derived from the distribution images was compared with the bulk composition of the sample determined via ICP-OES. The results of the comparison are summarized in Table 2.04. The determined values

agree very well with relative deviations below 2 % for the Al/La, Li/La as well as the Zr/La atomic ratios. This excellent agreement confirms the accuracy of the developed LA-ICP-OES analysis.

Table 2.04: Comparison of the average sample stoichiometry determined via LA-ICP-OES imaging with the bulk composition determined using conventional ICP-OES analysis. The stated measurement uncertainties of the LA measurement correspond to the double standard deviations of all averaged pixels; the stated measurement uncertainties of the liquid measurement correspond to the confidence intervals of the mean values derived from the measurement of three replicate digestions (α = 0.10, n = 3). Both methods show excellent agreement.

		LA-ICP-OES	ICP-OES (liquid)	Relative deviation
Atomic ratio	Li/La	2.03 ± 0.12	2.05 ± 0.05	- 0.9 %
	Al/La	0.068 ± 0.016	0.067 ± 0.007	1.7 %
	Zr/La	0.65 ± 0.03	0.661 ± 0.006	- 1.4 %
Formula		$Li_{6.09}Al_{0.20}La_3Zr_{1.96}O_{11.8}$	$Li_{6.15}Al_{0.20}La_3Zr_{1.98}O_{11.9}$	

2.4 Conclusion

The use of LA-ICP-OES for the laterally resolved analysis of the solid electrolyte material LLZO was successfully demonstrated. Reliable signal quantification was achieved by combining the use of in-house prepared and carefully characterized matrixed-matched standards with an internal-standard independent calibration strategy based on 100 m% normalization. The analysis shows a significantly improved precision for the Li determination compared to analogue LA-ICP-MS measurements, confirming that OES is better suited for the investigation of this material system.

The recorded distribution images revealed macroscopic composition variations within the bulk of Al stabilized LLZO samples. Beside strong Al inhomogeneities, also significant variations in the Li content were observed. The stoichiometry variations were most likely caused by the high-temperature treatment during the synthesis, leading to loss of Li_2O and Al diffusion. Moreover, the Li_2O loss depends on the Al content, with less loss for Al-rich samples.

The obtained results demonstrate the importance of spatially resolved sample characterization. Stoichiometry variations might strongly affect the electrochemical behavior of a solid electrolyte material and need to be monitored for that reason. To get a deep understanding of the material properties, combining electrochemical measurements with spatially resolved chemical analysis is necessary.

3 Local Li-ion conductivity changes within Al stabilized $Li_7La_3Zr_2O_{12}$ solid electrolytes and their relation to three-dimensional variations of the bulk composition

The study presented in this chapter has also been published as a scientific paper in "Journal of Material Chemistry A"[109].

3.1 Introduction

As already discussed in Chapter 2, an important aspect that needs clarification for understanding the conductivity behavior of LLZO are the partly very different ionic conductivities reported for nominally identical samples. Not only interfacial effects on the local or effective conductivity of samples, also strongly scattering bulk conductivities are reported. For LLZO stabilized by Al, published values for bulk conductivity cover essentially the entire range from 10^{-4} S cm^{-1} to 10^{-3} S cm^{-1}, whereby overall effective conductivities are often lower than the bulk value.[42,85,88,110] A recent study on 44 nominally identical samples revealed conductivities from about 10^{-5} S cm^{-1} to 0.8×10^{-3} S cm^{-1} for LLZO with 0.2 Al pfu.[88] Conductivity variations thus cannot be only attributed to different preparation routes and degradation effects and must be caused by another (yet unknown) parameter. One likely reason are unintended composition changes during LLZO synthesis,[88] which usually involves high temperatures at which lithium oxide loss and associated diffusion processes are to be expected. Investigating the impact of compositional variations and correlating them with the observed conductivity fluctuations is therefore crucial to get a better understanding of the conductivity behavior of LLZO.

Possible effects of local compositional variations beyond the surface region (i.e., in depths of several µm) were already investigated by LIBS and even 3D elemental maps of LLZO ceramics became accessible.[74–77] However, those were not correlated with local conductivities, rather the focus was on the impact of the composition on the overall interfacial resistances of the samples.[74,75]

In this study, bulk compositional variations within Al stabilized LLZO ceramics are investigated as a possible reason behind the scatter of bulk conductivity values. The relation between the local bulk ionic conductivity and the corresponding local bulk composition is investigated by combining ME-EIS with LA-ICP-OES. Impedance spectroscopic studies on circular microelectrodes with diameters of 100 µm revealed the bulk conductivity of a similarly sized region beneath.[111–115] Afterwards, in several depths beneath the electrodes (up to 100 µm

deep) the chemical composition was analyzed by LA-ICP-OES. These measurements enabled the analysis of correlations between local Al or Li content and local ionic conductivity. In contrast to many common interpretations of ion conduction in LLZO, neither the Al nor the Li content shows a simple correlation with the ionic conductivity. Thus, further local structural or compositional factors have to play a key role for the ionic conductivity of LLZO.

3.2 Experimental

3.2.1 Sample preparation

Four nominally identical samples (A, B, C, D) with an intended composition of $Li_{6.40}Al_{0.20}La_3Zr_2O_{12}$ were investigated. The synthesis route is based on the procedure described by Wagner et al.[106] and is identical to the one used in chapter 2 (see section 2.2.1).

3.2.2 X-ray diffraction

Phase analysis was performed by XRD experiments on a Panalytical X'Pert MPD with Cu K_α radiation. The pattern was analyzed with HighScore[116], a program provided by Panalytical. A 2θ scan range between 5° and 120° with a step size of 0.026° was used.

3.2.3 Electrochemical impedance spectroscopy

The ionic conductivity was measured by EIS. To measure the effective conductivity of macroscopic specimens (macroelectrode measurements), samples were polished by SiC grinding paper (P4000) to remove near surface reaction layers, and thin films of Pt (200 nm) and Ti (10 nm) were deposited on the top and bottom side as electrodes. A thin film of titanium is required in order to improve the adhesion of platinum. For the EIS measurements, an Alpha-A high performance frequency analyzer (Novocontrol Technologies, Germany) was used in the frequency range from 10 Hz to 3 or 10 MHz. In such macroelectrode measurements the temperature was controlled by a F-25 HE thermostat (Julabo GmbH, Germany), and the exact temperature was 25.4 °C, determined by a thermocouple at the sample.

Local conductivities were measured by means of microelectrodes. Using photolithographic techniques in combination with ion beam etching, circular electrodes with diameters of 100 µm were prepared from the macroscopic Pt/Ti thin films on top of the samples. Microelectrode measurements were performed at ambient temperature (T = 23.5 °C). Tungsten needles were

used to contact the microelectrodes under an optical microscope. The position of the needles was adjusted by mechanically controlled micromanipulators. Figure 3.01a illustrates the measurement setup and Figure 3.01b shows a part of the microelectrode array on top of the sample. Impedance spectroscopic measurements (Novocontrol Alpha Analyzer) were then performed between a microelectrode and a counter electrode on the bottom side (Pt thin film with Pt paste at the sample edges for contact reasons).

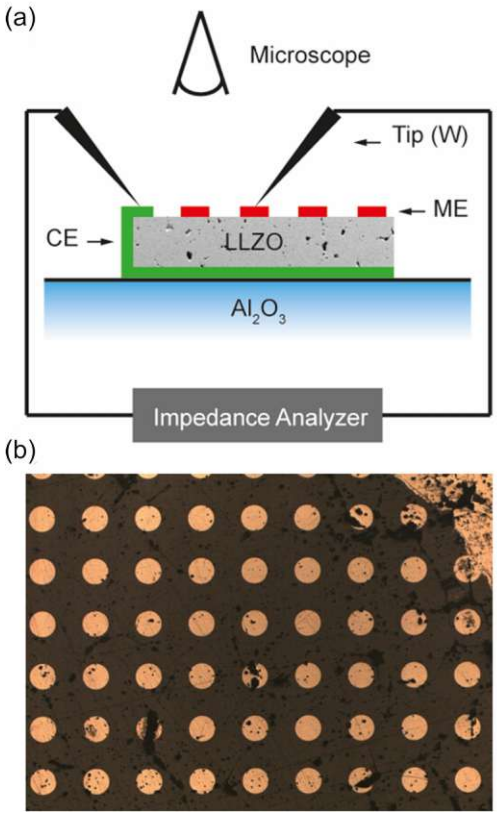

Figure 3.01: (a) A scheme of the microelectrode measurement setup. (b) An optical microscope image showing a part of the microelectrode array on top of a sample.

3.2.4 LA-ICP-OES

Spatially resolved chemical analysis of the samples was performed using LA-ICP-OES. A NWR213 laser ablation system (ESI, USA) equipped with a frequency quintupled 213 nm Nd:YAG laser and a fast-washout ablation cell was used for the measurements. The laser ablation device was coupled to an iCAP 6500 RAD ICP-OES instrument (ThermoFisher Scientific, Germany). A detailed description of the used measurement set-up, instrumental setting, and quantification strategy as well as information about the image processing can be found in Chapter 2 (see Section 2.2).

Two-dimensional elemental distribution images covering the whole sample surfaces were created for all four LLZO pellets. The analysis was performed in sample depths of approx. 5, 50 and 100 µm. This depth (with respect to the original surface) was reached by mechanical polishing the surface with SiC grinding paper (P2000) for certain times. In additional calibration studies these polishing times were related to the amount of removed material. Hence, a kind of three-dimensional compositional map became accessible. This approach also ensured that the measured "local" electrical conductivities (averaging over depths between 0 and 200 µm) could be truly related to the bulk composition within this specific sample region.

3.3 Results and discussion

3.3.1 Sample quality

The geometries of the resulting polycrystalline pellets are listed in Table 3.01. The typical LLZO-grain size is about 100 to 200 µm (Figure 3.02). The relative density of the samples, measured by a pycnometer (Brand GmbH), is about 91 %. The XRD analysis confirmed the cubic structure of the investigated samples (Figure 3.03). Only very minor signals from second phase were found, particularly lithium oxide in sample A.

Table 3.01: Thickness and surface area of the investigated LLZO samples (A, B, C, D)

	Thickness (h) [cm]	Area (A) [cm^2]
A	0.41	0.34
B	0.46	0.35
C	0.10	0.45
D	0.21	0.39

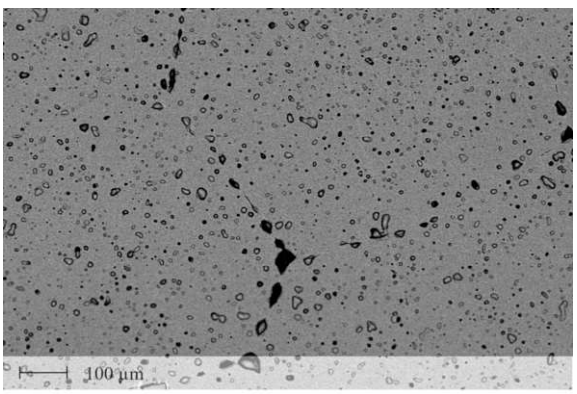

Figure 3.02: SEM image of an Al stabilized LLZO (Al = 0.20) garnet after sintering at 1230 °C for 6 h. Dark spots indicate the existence of some pores.

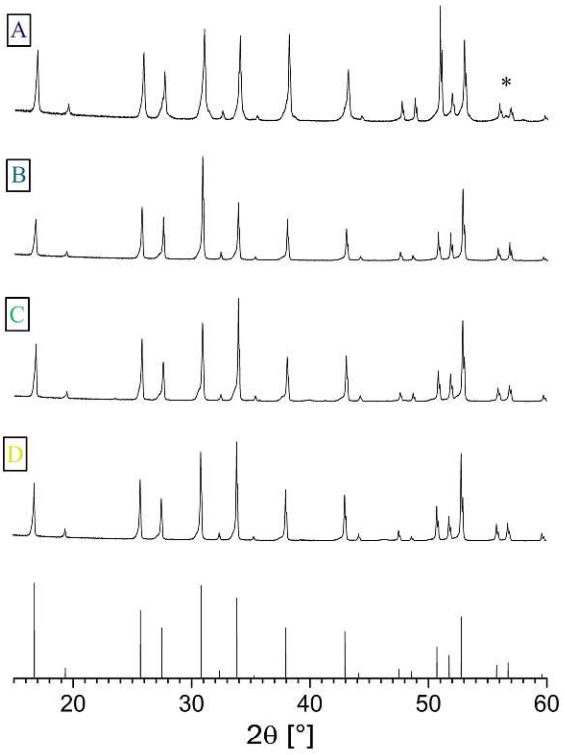

Figure 3.03: XRD patterns of samples A-D as well as the cubic reference pattern (bottom). Very little secondary phases could be found, (*) indicates LiO_2 in sample A.

3.3.2 Macroelectrode measurements

Before microelectrodes were prepared from the deposited Pt thin film, the very same film was used as a macroscopic electrode to measure the effective conductivity of each sample. The geometry-normalized impedance spectra of all Al stabilized LLZO samples at 25.3 °C are plotted in Figure 3.04. They all show a part of a "semicircle" at high frequencies, followed by a well separated low frequency contribution which represents the impedance of the ionically highly resistive electrodes (Ti/Pt). In agreement with earlier studies, the resistance of the high frequency feature is attributed to ion conduction in the bulk.[54,117] Neither contributions from grain boundaries nor clear indication of interfacial layers at the electrodes are visible.

To quantify the impedance spectrum properly, a resistor in parallel to a constant phase element ($R_1\|CPE_1$) is used for the bulk contribution, in series to a constant phase element CPE_2, describing the partially blocking electrode. The impedance of a constant phase element includes the two fit parameters Q and n as well as the angular frequency ω according to $Z_{CPE} = Q^{-1}(i\omega)^{-n}$. The inductance due to wiring was subtracted from all impedance data. The equivalent circuit is also shown in Figure 3.04 and leads to a reliable fit (dashed line) of the impedance spectra. The

fit parameters of the spectra in Figure 3.04 are given in Table 3.02. The resulting relative permittivities (ε_r), calculated from CPE_1 in accordance with Ref.[118], are in the range of 45 to 78. Such a value confirms the bulk-type character of this part of the spectrum.

From the resistance R_1, the effective bulk conductivity σ_{macro} can be calculated by

$$\sigma_{macro} = \frac{h}{A\,R_1}\ [S\ cm^{-1}] \qquad (3.01)$$

with h being the sample thickness and A the surface area. In this case the bulk conductivity lies between 1.6 and 4.8 × 10^{-4} S cm^{-1}, which is within the range typically found for LLZO samples stabilized with 0.2 pfu Al.[42,49,74,88,90,119–121] A CPE exponent $n = 1$ would correspond to an ideal capacitor. There are several possible reasons for $n < 1$, one being a distribution of different bulk relaxation frequencies $\omega = (\sigma\varepsilon)^{-1}$ within the sample (σ = conductivity, ε = permittivity). When assuming rather constant permittivities in the LLZO samples one may thus speculate already from the n-values, that samples C and D might be electrically least homogeneous. Essentially, the local conductivity data presented in the following are in accordance with this speculation.

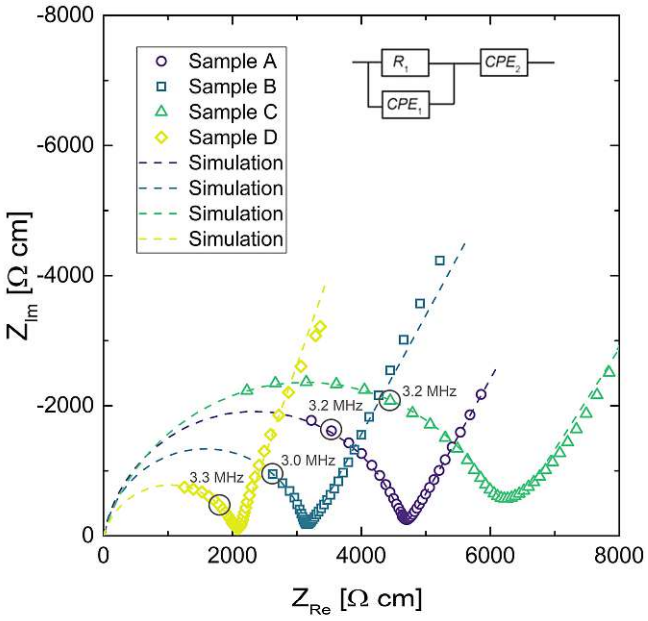

Figure 3.04: The (geometry-normalized) impedance spectra of the Al stabilized LLZO samples at 25.3 °C with macroelectrode measurement data, after subtracting the inductance due to wiring, and the simulation based on the fit to the equivalent circuit shown in the graph.

Table 3.02: Fit parameters R_1, Q_1, n_1 and calculated bulk capacitances C_1, relative permittivities ε_r as well as conductivities of the macroscopic LLZO samples (σ_{macro}).

R_1 [Ω]	σ_{macro} [mS cm^{-1}]	Q_1 [10^{-11} F s^{n-1}]	n_1	C_1 [10^{-12} F]	ε_r
5608	0.21	3.18	0.88	3.82	52
4045	0.32	0.896	0.97	5.27	78
1352	0.16	33.6	0.83	18.0	45
1112	0.48	24.8	0.82	11.5	70

3.3.3 Microelectrode measurements

From measurements with macroscopic electrodes only averaged effective bulk conductivities can be obtained. Microelectrodes, on the other hand, provide a tool to measure spatially resolved conductivities. This becomes possible since most of the voltage between the microelectrode and a spatially extended macroscopic counter electrode drops near to the microelectrode. The resistance measured between a well-defined circular microelectrode of diameter d on top of a typical sample and an extended counter electrode on its bottom side is largely determined by the conductivity of a hemisphere beneath a microelectrode with a radius of about $2d$.[111] It mainly reflects the charge transport resistance of the probed sample volume and is virtually independent of the sample thickness. From this so-called spreading resistance R_{Spread}, the local ionic conductivity of the probed sample volume σ_{Me} can then be calculated from

$$\sigma_{Me} = \frac{1}{2\,d\,R_{Spread}}\ [S\,cm^{-1}], \qquad (3.02)$$

provided the distance between the microelectrode and the extended counter electrode is much larger than the microelectrode diameter.[111–115,122–124]

On each sample an array of circular electrodes with a diameter of 100 µm was applied. By subsequently contacting individual microelectrodes and measuring the impedance spectra between a microelectrode and a macroscopic counter electrode it is thus possible to resolve local conductivity variations on the length scale of a few 100 µm. However, one has to keep in mind that these microelectrode measurements still average over a certain (small) sample volume.

Figure 3.05 displays typical impedance spectra of such microelectrode measurements for all four samples. The impedance spectra are analyzed by the simple equivalent circuit shown in this Figure. The resistive element R_{Spread} describes the ionic charge transport in the probed

LLZO volume. The serial constant phase element (CPE_2) is attributed to the ionically partially blocking electrode material, as for the macroelectrode measurement in Figure 3.04. Parallel to these two elements is a stray capacitance (CPE_1) with a value in the range of 200 fF. This is caused by the measurement setup, particularly by the capacitance between contacting needle and the counter electrode. Actually, such a stray capacitance is also present in macroscopic measurements, but there it can be neglected compared to the other capacitances and thus it is not needed in the circuit of Figure 3.04. On the other hand, an additional constant phase element in parallel to R_{Spread}, reflecting the very small LLZO bulk capacitance (in the 100 fF range), leads to an over-parameterization of the microelectrode equivalent circuit and was therefore avoided. More details on the appropriateness of this approach to analyze microelectrode measurements on LLZO are given in Ref.[89]. The obviously less pronounced separation between electrode spike and bulk arc in microelectrode measurements (cf. Figure 3.04 and Figure 3.05) is simply caused by the additional stray capacitance (CPE_1) and the corresponding peak frequency shift of the bulk arc.

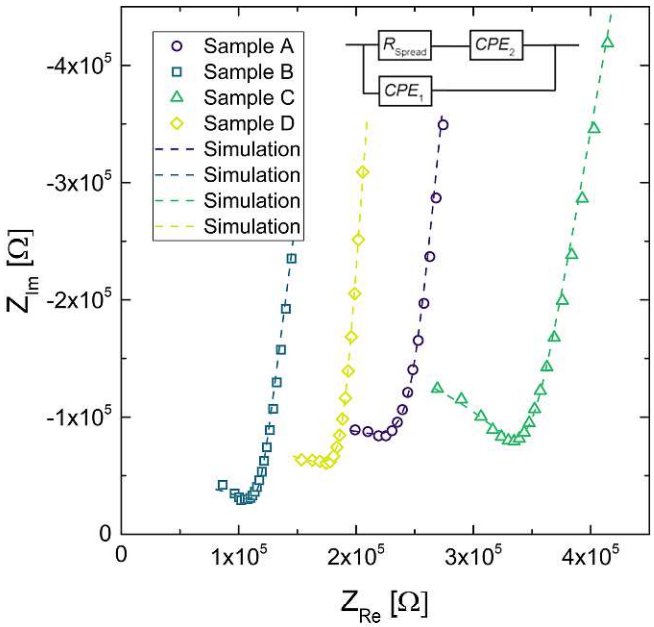

Figure 3.05: Exemplary impedance spectra obtained with microelectrodes of diameter d = 100 µm, for all samples. The corresponding fits (dashed line) are based on the equivalent circuit shown above.

3.3.4 Local conductivities

Figure 3.06a illustrates the location of the microelectrodes on sample A and the corresponding local conductivities beneath the investigated microelectrodes, using a color map. Light colors (yellow, green) indicate areas with a higher ionic conductivity (above 2.0×10^{-4} S cm^{-1} in this

specific sample) and cold colors (blue) represent low conductive areas (below 8.0×10^{-5} S cm^{-1}). In Figure 3.06b, measurements of one row of microelectrodes from the left to the right side of the sample, show a gradient in conductivity. Values vary by more than a factor of six, between 4.2×10^{-5} S cm^{-1} on the right hand side to 2.8×10^{-4} S cm^{-1} on the left hand side. Similar results were obtained for the rows above and beneath the highlighted row.

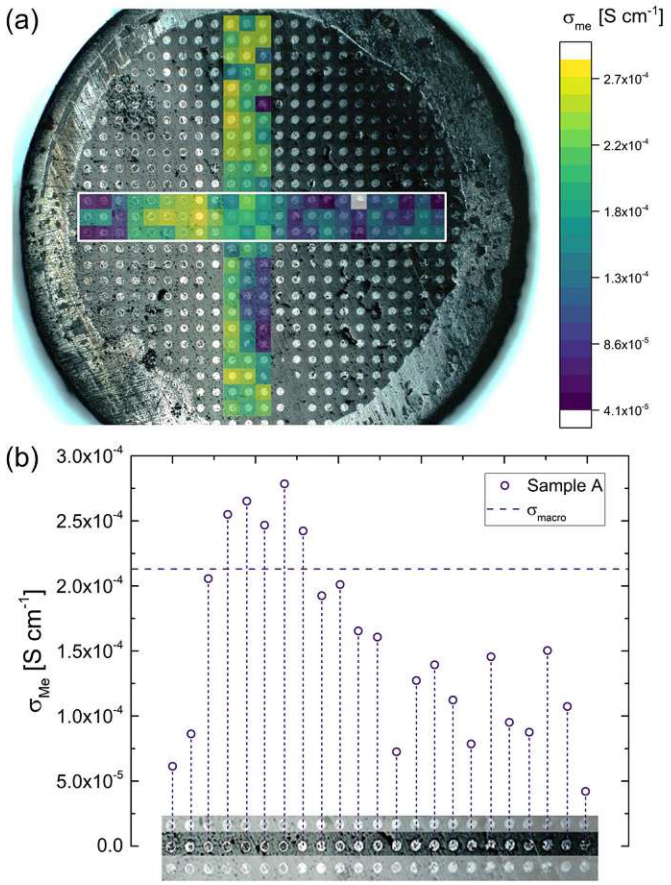

Figure 3.06: (a) Local conductivities obtained from microelectrode measurements (sample A). Colored areas mark the investigated region of the sample and indicate the measured conductivity (yellow represents high conductivity, violet low conductivity). (b) The middle row of microelectrodes highlighted by a white rectangle in (a), displays the given change in conductivity from the left side of the sample to the right side.

This demonstrates that parts of the sample exhibit higher conductivities than the effective σ_{macro} (2.1×10^{-4} S cm^{-1}) while others are less conductive. The corresponding electrical conductivity variation might also be the reason behind the reduced n-value (0.88) of the macroscopic experiment. The existence of a gradient is also in agreement with a previous study, where reducing the size of LLZO samples and repeatedly measuring σ_{macro} also revealed conductivity variations.[88] Measurements from top to the bottom of the sample (vertical colored bar in Figure 3.06) indicate further conductivity fluctuations but not such a clear trend as found for the horizontal measurements.

Similar local conductivity measurements were done on sample B (Figure 3.07). This sample was covered with differently sized microelectrodes (10 to 300 µm), but for the sake of comparability, only electrodes with a diameter of 100 µm were investigated. On average the local conductivities are even slightly higher than σ_{macro} = 3.2 × 10^{-4} S cm^{-1}, but overall little conductivity variations and good agreement with the macro measurements are found. The rather good agreement of microelectrode and macroelectrode experiments in this sample is further supporting the interpretation of microelectrode measurements measuring bulk related properties. Hence, it is assumed that the conductivity gradients observed for sample A truly reflect bulk conductivity inhomogeneities. The rather homogeneous conductivity of sample B might also cause the high n-value of the CPE (0.97, see Table 3.02).

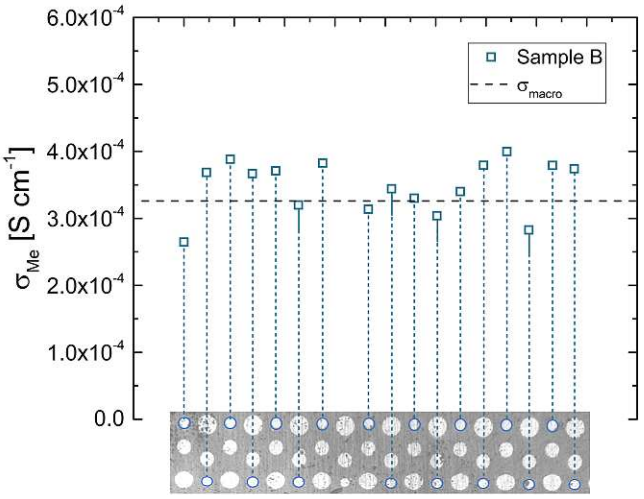

Figure 3.07: Local conductivity measurements obtained from sample B using 100 µm electrodes. The local conductivity does not show very pronounced variations.

The macroelectrode measurement of sample C revealed a lower effective conductivity compared to sample A and B (1.6 × 10^{-4} S cm^{-1}). Microelectrode measurements were performed on both sides of this sample. On *side one* (Figure 3.08 – triangles), measured conductivities are either similar (many spots) or smaller (some spots) than σ_{macro} but did not shown any spatial trend. Compared to sample B much more scattering is present. The measurements on *side two* (Figure 3.08 – circles) resulted in very similar conductivities, again some spots were less conductive, the majority, however, was close to the obtained macroelectrode value. Accordingly, a very reasonable agreement between the effective macroscopic conductivity (probing the entire depth) and typical local conductivities (probing bulk regions only down to about 200 µm depth) can be observed. Thus a comparatively low overall ionic conductivity seems to be present across the entire sample and the low σ_{macro} value is not caused by a low conductive layer close to the surface. Such a layer would have strongly affected the local measurements (probing less depth), which is not seen here.

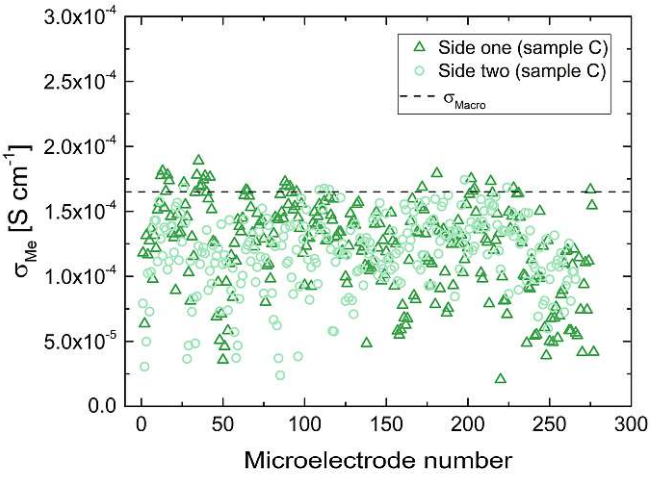

Figure 3.08: Microelectrode measurements on sample C from side one (triangles) and side two (circles) of the sample.

Microelectrode measurements on sample D resemble those on sample B with little spatial variation of the local conductivity (not shown). However, the average local conductivity in the investigated sample parts is in the range of 2.0×10^{-4} S cm^{-1} and thus smaller than the effective macroscopic conductivity, suggesting that at least some conductivity inhomogeneity is present somewhere in the sample. The latter is also in accordance with the lowest n-value of the CPE (0.82).

3.3.5 LA-ICP-OES analysis

Based on existing ideas on a direct relation between cation composition (Al or Li content) and conductivity, we may expect from the microelectrode measurements that some samples should show significant compositional variations (causing conductivity gradients) while other samples with little lateral conductivity gradients should be chemically rather homogeneous. In order to test this hypothesis, a detailed analysis of the local chemical composition using LA-ICP-OES was performed. Large sample regions including those probed by local impedance spectroscopy were examined.

In order to investigate the correlation of local conductivity and local composition it is essential to ensure that both local measurements refer to the same sample region. Microelectrode measurements using d = 100 µm probe spatial regions in the same range; as an estimate, often a hemisphere with radius $2d$ is used as the relevant volume.[111] The probed sample volume of LA-ICP-OES measurements strongly depends on the analyzed material, utilized laser and chosen laser settings, however, it is typically significantly smaller than that. While analyzed areas (defined by laser beam size) with a diameter of a few hundred µm lie in the accessible range of commonly used instruments, the probed depth hardly surpasses more than a few µm.

As a first step chemical analysis of near surface layers on LLZO has to be avoided, since those are well-known to exhibit different chemical compositions and may include different phases.[27,29,33-35] Also Li^+/H^+ exchange caused by water from the air has been reported and should been taken into account.[39,73,125–127] In Ref.[73] proton exchanged surface regions with thicknesses between 1 and 2 µm are reported. Effects of such surface region are avoided by two measures: first, before the first chemical analysis by LA-ICP-OES, approx. 5 µm LLZO are mechanically removed by polishing (grinding), see Experimental. Second, any further reaction products resulting from the contact with ambient air after grinding are removed by a pre-ablation step performed directly before the measurement (approx. 2 µm). Hence, already the very first analysis takes place in a depth of several µm (represented by estimated 5 µm in the following) and thus reflect the bulk composition in this depth rather than any surface effect. However, still the composition in 5 µm depth might differ from the average composition in the ca. 200 µm range probed by the microelectrodes. In Ref.[76], for example, chemical composition changes in the first few µm of LLZO ceramics were found and characterized by LIBS. Therefore, by further grinding the LLZO samples, regions in 50 µm and 100 µm depth (with respect to the original surface) were investigated and a kind of (rudimentary) 3D compositional map of some samples could thus be obtained. The results of this depth dependent analysis are discussed in the following.

The result of the local chemical analysis on sample A, performed by LA-ICP-OES in a depth of approx. 5 µm is shown in Figure 3.09 for Al (a), Li (e) and Zr (g). The measurement data is not smoothened, each pixel represents the stoichiometry, calculated based on the measured atomic ratios (choosing 3 pfu La as the fixed-point).

Most obvious is the gradient in the Al content from top left to bottom right, with values varying by about a factor of two from 0.15 pfu to 0.30 pfu. In accordance with the common model of Al reducing the Li content, this is accompanied by a (scattered) Li gradient with highest Li content in the Al-poor region. The Zr signal shows very little variation and a homogeneous distribution across the sample, as well as a good agreement with the theoretical Zr content of 2.0 pfu. A simple explanation for these Al and Li variations cannot be given yet. During sintering one edge of the sample might have been exposed to a lower local lithium oxide activity in the gas phase. Thus, stronger Li loss might have taken place, which in turn might create a driving force for Al diffusion.

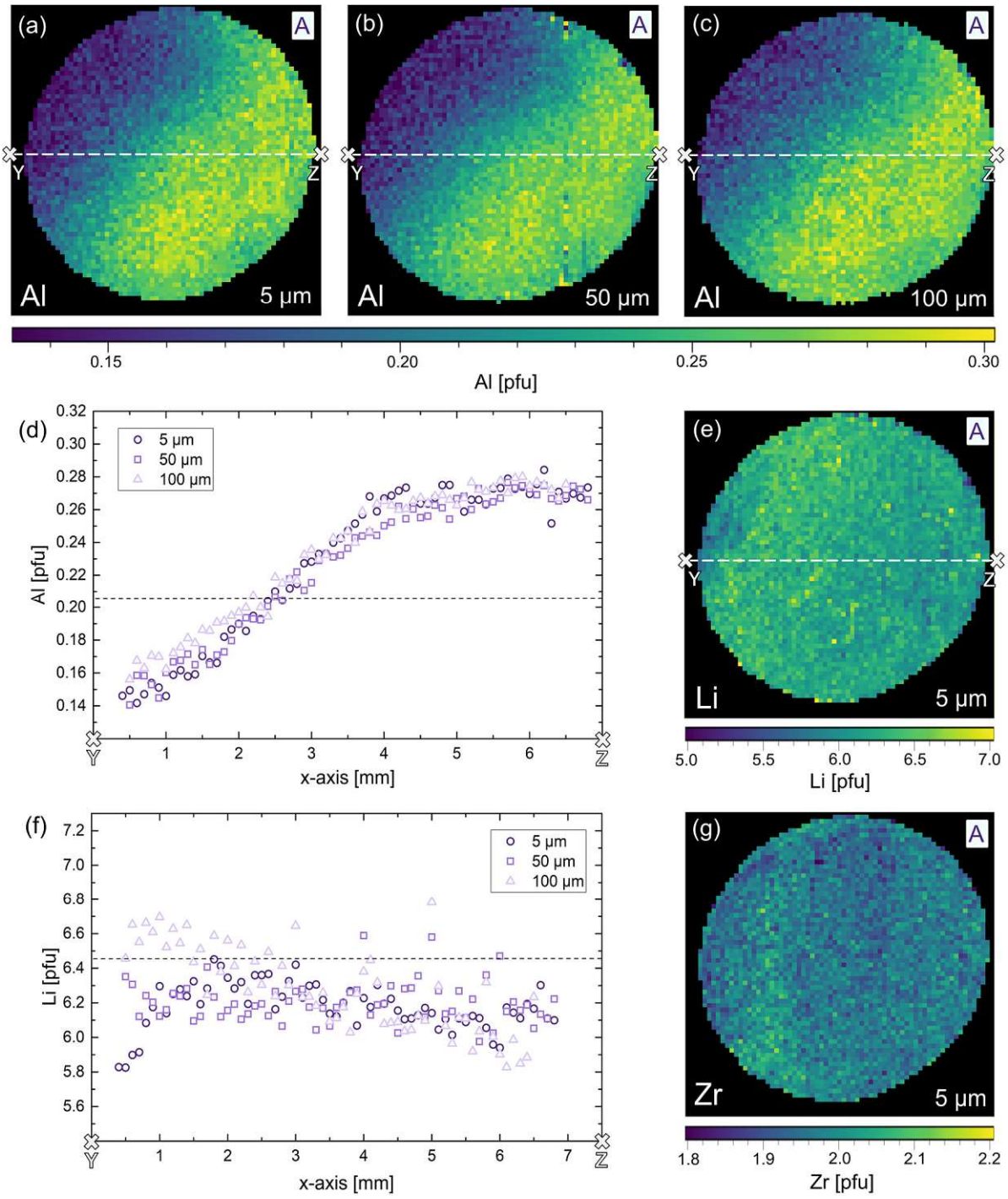

Figure 3.09: LA-ICP-OES measurements on sample A in three different sample depths. Two-dimensional distribution images of Al (a-c), Li (e), and Zr (g) pfu as well as the lateral changes of the Al (d) and Li (f) content in the cross section from Y to Z are shown. Dashed lines indicate the nominal value according to $Li_{6.4}Al_{0.2}La_3Zr_2O_{12}$.

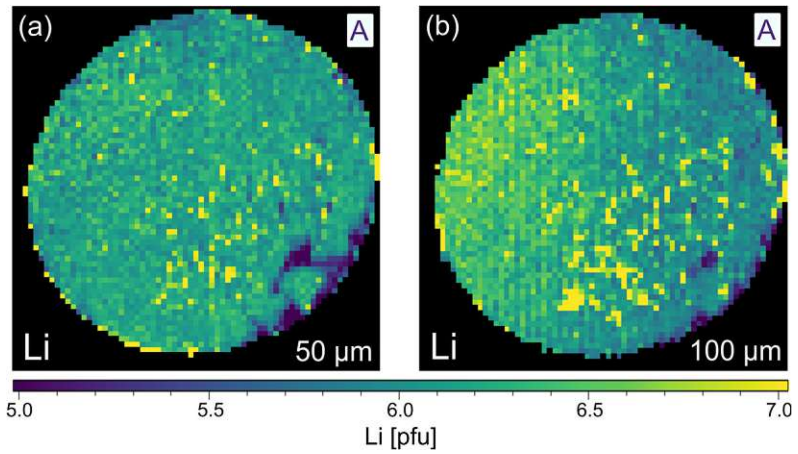

Figure 3.10: LA-ICP-OES distribution images of sample A, illustrating the amount of lithium in (a) 50 µm and (b) 100 µm sample depth.

The same experiment was repeated in 50 µm and 100 µm depth and the distribution images of Al are also shown in Figure 3.09b+c; the corresponding Li distributions are given in Figure 3.10. It is very obvious that the Al gradient is also present in this depth thus indicating absence of strong compositional variation perpendicular to the surface within about 100 µm. This is confirmed quantitatively by comparing the Al and Li content in cross sections (white lines) of the three distribution images, see Figure 3.09d+f. In these cross sections, averaging over six neighboring pixels was performed to better reveal overall trends. Clearly the Al stoichiometry variation is present in all depths.

Also samples B, C and D were chemically analyzed by LA-ICP-OES, for D again in three depths, for C in two depths, and B in a depth of 5 µm only. Al distribution images of all three samples are shown in Figure 3.11a-c.; further Al and all Li distribution images are shown in Figure 3.12 (sample B+C) and Figure 3.13 (sample D). First of all, also the measurements in different depths confirmed that the data found for ca. 5 µm depth already correspond to the bulk composition in much deeper regions. Hence, it can be concluded that the chemical composition found by the LA-ICP-OES measurements represents the chemical composition of the local region probed by microelectrodes, irrespective of the depth used for analysis. It is thus meaningful to use this data for looking at correlations between local chemical composition and local conductivity, with "local" meaning average values in regions with a size of approx. 100 to 200 µm in each direction.

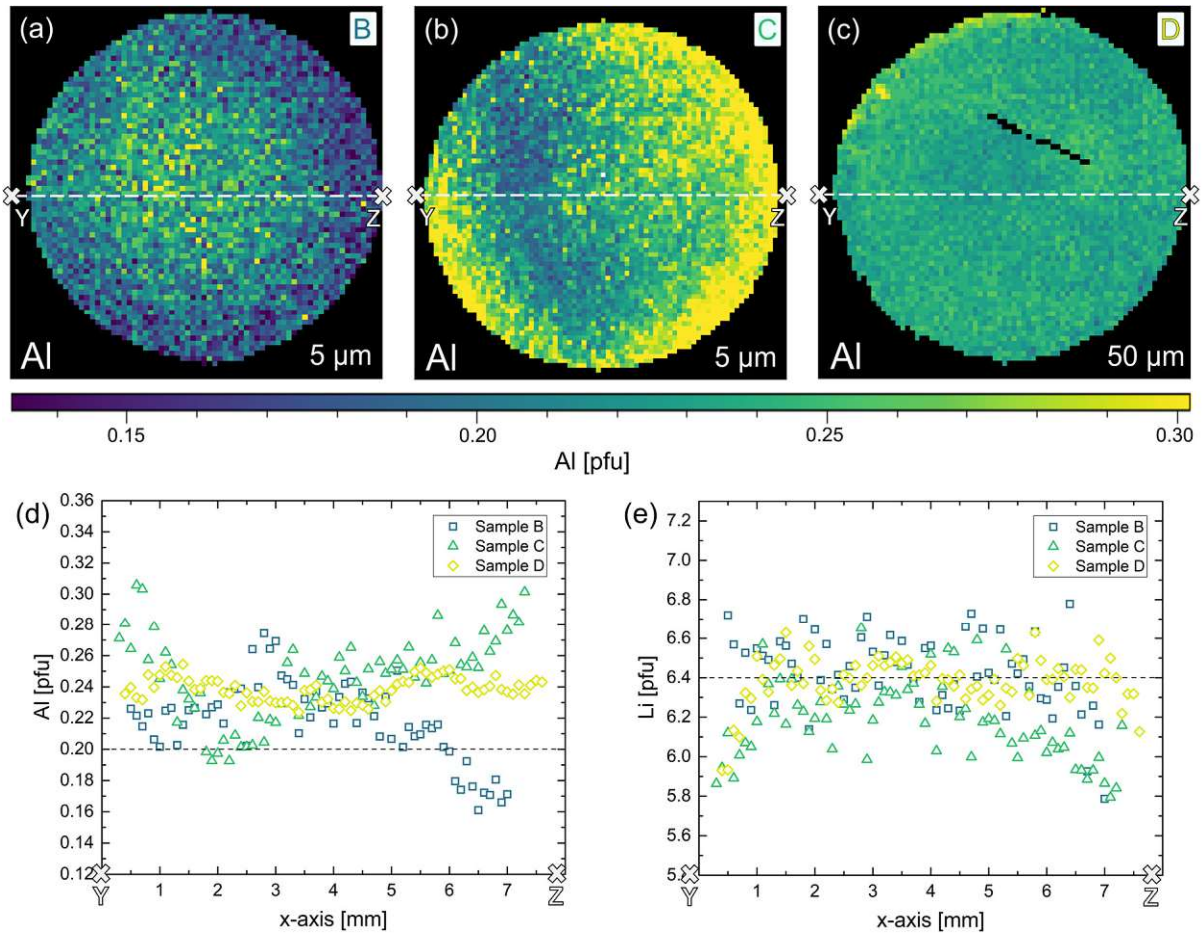

Figure 3.11: Lateral resolved LA-ICP-OES analysis of sample B, C, D, illustrating distribution images of Al in (a) sample B, (b) sample C, (c) and sample D as well as the (d) Al and (e) Li content in the corresponding cross sections. Dashed lines indicate the nominal value according to $Li_{6.4}Al_{0.2}La_3Zr_2O_{12}$.

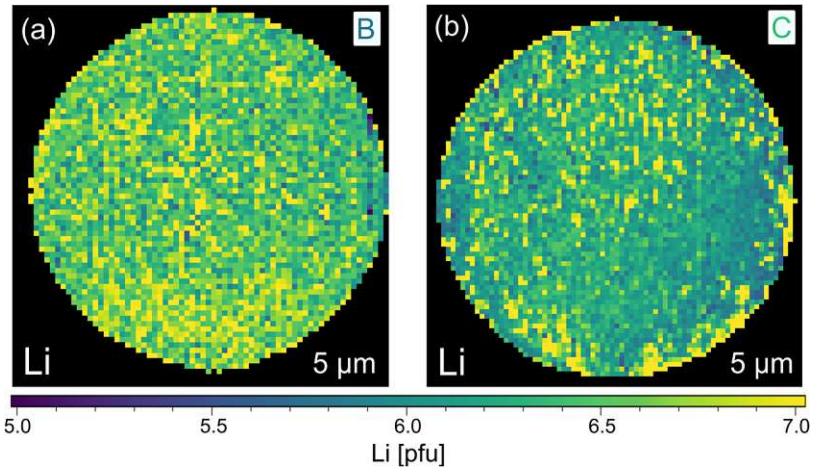

Figure 3.12: LA-ICP-OES images of (a) sample B and (b) sample C, illustrating the amount of Li in 5 µm depth.

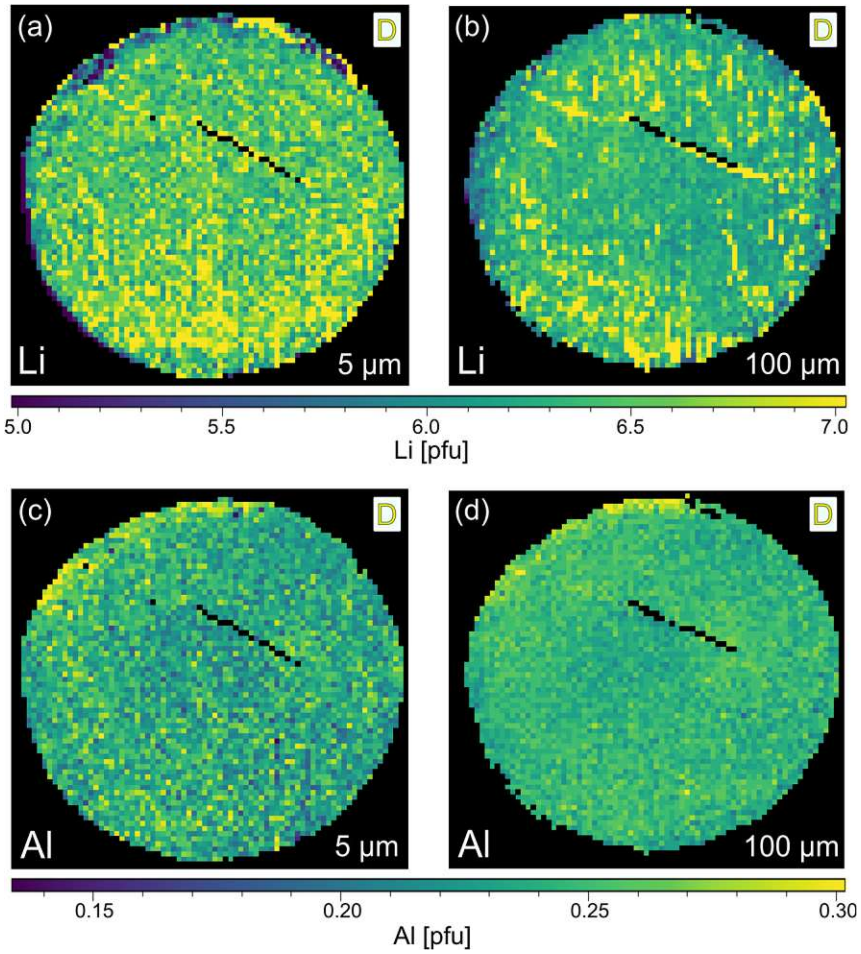

Figure 3.13: LA-ICP-OES images of sample D, illustrating the amount of (a,c) Li and (b,d) Al in 5 µm and 100 µm depth.

Lateral chemical variations of Al are also present in samples B and C with B showing an Al enrichment in the center part of the pellet (see Figure 3.11a+d) and C exhibiting a "scattered" minimum in Al content somewhere in the center (see Figure 3.11b+d). Sample D was the most homogeneous sample with only moderate scatter of Li and Al content (see Figure 3.11c-e and Figure 3.13). In these samples, a correlation between Al and Li content is not visible. This, however, might be due to the fact that a very high precision of the Li determination is required to see the small relative changes of the Li content caused by the Al variations. Moreover, lithium oxide loss during sintering with formation of oxygen vacancies[128] might affect the cation ratios.

From all measured LA-ICP-OES data of a given sample, i.e., by averaging laterally and for different depths, average chemical compositions can be calculated. Those are shown in Table 3.03. In sample A the measured Al content was slightly higher and the measured Li content was lower than expected, leading to a total composition of $Li_{6.20}Al_{0.23}La_3Zr_{2.01}O_{11.95}$ when calculating the oxygen content for fixed cation charges. A lower amount of lithium is not too surprising, due to its volatility during sintering. The behavior of Al is less straightforward

to interpret. Possibly a gradient in Al not only exists laterally, on the mm scale (cf. Figure 3.9), but also across the entire sample with somewhat less Al in the center parts beyond the 100 µm depth probed by LA-ICP-OES. Even though the sample pellets were placed between two additional pellets of pure $Li_7La_3Zr_2O_{12}$ during sintering to avoid contamination, also incorporation of additional Al^{3+} from alumina crucible cannot be ruled out. Sample B–D show slightly increased Al content as well, supporting this hypothesis.

While sample C shows a lower Li content than expected, like sample A, the measured Li amounts of sample D and B are close to the nominal value or higher than expected, indicating that different amounts of lithium oxide were lost during sintering.

Table 3.03: Average chemical composition of sample A–D in a depth between 5 and 100 µm. The values for the oxygen are calculated from the cation composition based on charge balance considerations.

	Li/La	Al/La	Zr/La	composition
A	2.07	0.076	0.669	$Li_{6.20}Al_{0.23}La_3Zr_{2.01}O_{11.95}$
B	2.16	0.069	0.637	$Li_{6.49}Al_{0.21}La_3Zr_{1.91}O_{11.86}$
C	2.10	0.089	0.631	$Li_{6.30}Al_{0.27}La_3Zr_{1.89}O_{11.83}$
D	2.13	0.080	0.682	$Li_{6.39}Al_{0.24}La_3Zr_{1.92}O_{12.15}$

3.3.6 Correlation of conductivity and chemical composition

Based on these conductivity measurements and compositional data it can now be analyzed whether or not simple correlations exist between electrical properties and composition. Sample A exhibits both, a lateral compositional and a lateral conductivity variation and a correlation of both would not be surprising. However, overlaying both results for two cross sections (Figure 3.14a+b) already shows that there is at least not a simple relation. This becomes even clearer when plotting all measured conductivities vs. the corresponding Al or Li content (Figure 3.14c–e, shown for two depths). The dotted lines in these plots represent the nominally expected amounts of Al (0.20 pfu) and Li (6.40 pfu), respectively. Similarly high conductivity values are found over the entire Al range, i.e., from 0.15 to 0.30 pfu. Only the scatter of conductivity values seems to depend on the amount of Al, with less or no low conductive regions around 0.20 to 0.23 pfu Al. The statistical significance of this, however, is not clear. In the plot of conductivity vs. Li content the scatter is the same for all Li contents and essentially all Li contents from 6.1 to 6.6 pfu exhibit some data points with reasonably high conductivities. This is a first strong indication that the conductivity of LLZO does not show a simple correlation to the Li or Al content.

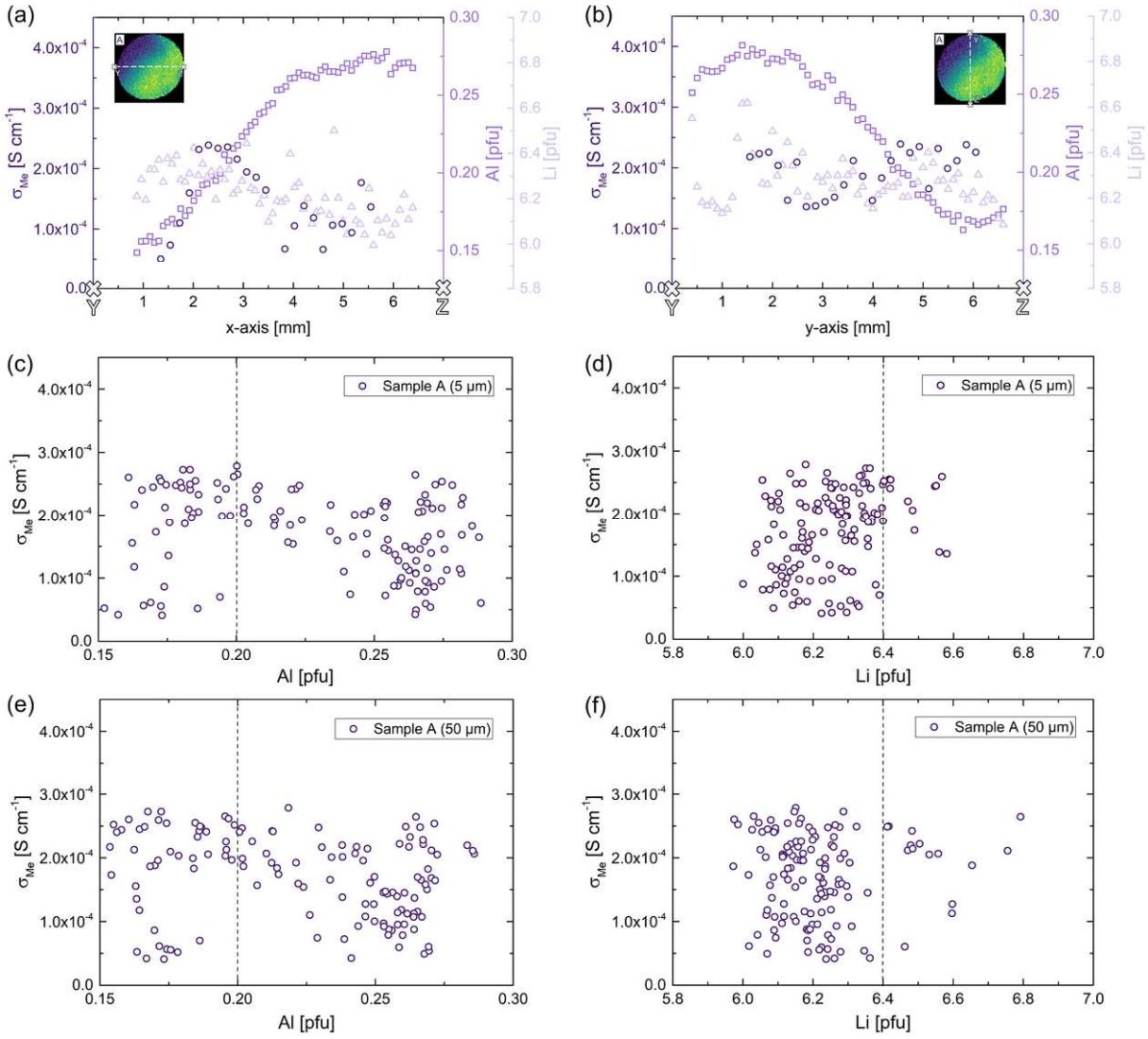

Figure 3.14: Correlation of laterally resolved conductivity and stoichiometry measurements on sample A. (a,b) Conductivity as well as Al and Li content along two cross sections. Conductivity of each measured microelectrode vs. the corresponding amount of Al and Li in (c,d) 5 µm and (e,f) 50 µm depth. Dashed lines indicate the nominal value according to $Li_{6.4}Al_{0.2}La_3Zr_2O_{12}$.

Figure 3.15 displays plots of conductivity vs. composition (Li or Al) for the other samples. Sample B and D show only moderate composition variation with Al as well as Li content in a similar range. Also the conductivity variations are comparatively small, however, sample B shows significantly higher local conductivities (about 3.5×10^{-4} S cm^{-1}) compared to sample D (about 2.0×10^{-4} S cm^{-1}). Sample C, finally, includes a substantial variation of the chemical composition while staying at relatively low conductivity. Hence a broad range of Al and Li content leads to very similar conductivity values.

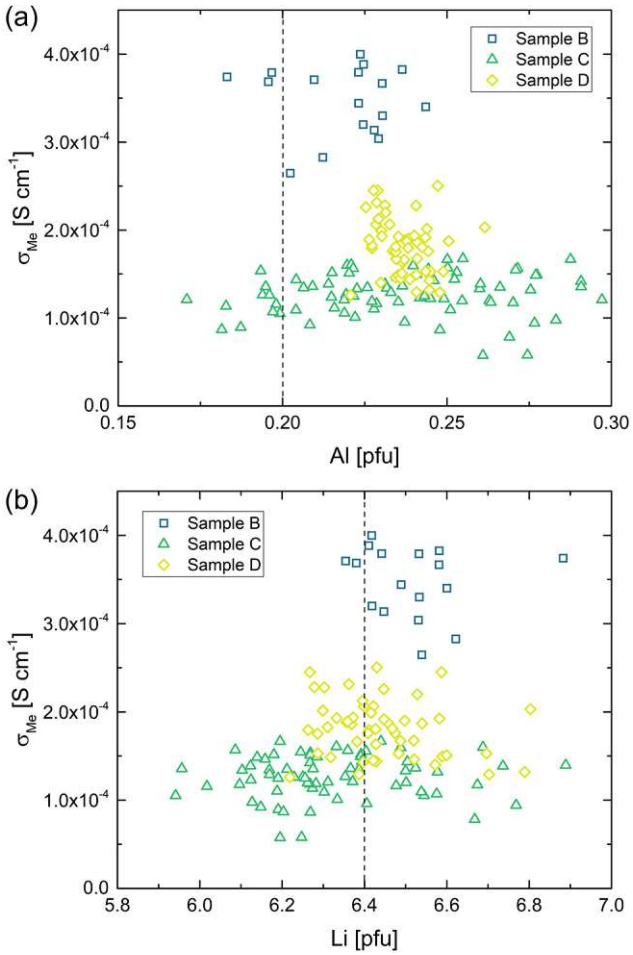

Figure 3.15: The conductivity of each measured microelectrode on sample B–D vs. the corresponding amount of (a) Al and (b) Li averaged over all measured sample depths. The dashed lines represent the intended composition, 0.20 Al pfu and 6.40 Li pfu.

From all these plots it becomes also clear that for the same Al content the conductivity can vary by almost an order of magnitude. The same is true for the Li content. This is exemplified by the conductivity and composition data of four different spots on sample A (Table 3.04). Two of them exhibit a rather high Li amount (6.35 pfu and 6.37 pfu), but conductivities vary from rather low (0.56×10^{-4} S cm^{-1}) to acceptably high (2.42×10^{-4} S cm^{-1}). On the other hand, if the amount of lithium is pretty low (6.12–6.13 pfu) the ionic conductivity can still be either acceptably high (2.54×10^{-4} S cm^{-1}) or more than three times lower. Accordingly, there seems to be no optimal Li content (within the range considered here, i.e., between about 6.0 and 6.7 pfu) in contrast to suggestions in literature.

Overall, it can be concluded that there is no clear and simple relation between ionic conductivity and Al or Li content in Al stabilized LLZO. Hence, other aspects have to be of high relevance for the Li ion conductivity that are not simply reflected by the concentration of the stabilizing cation (Al) or the absolute Li content. Clarifying the true reasons behind varying conductivities

requires detailed further measurements and is beyond the scope of this work. Two possible reasons are suggested: first, Li ion conduction in LLZO is a complex phenomenon with different cation sites being involved.[43,78–80,129] The exact site occupancy in a LLZO sample, and thus also the effective mobility of Li, may depend on preparation and might exhibit gradients within samples. Those are not accessible by mapping local compositions only. Accordingly, the detailed local structure might be more important for the ionic conductivity than the exact Al or Li content.

Second, existence of oxygen vacancies and their effect on the lithium ion conduction might be another important aspect to consider. Recent tracer exchange experiments with subsequent SIMS analysis revealed presence of possibly substantial amounts of oxygen vacancies in various LLZO samples.[128] Also the results of this study are indicating sub-stoichiometric amounts of oxygen: calculating the average oxygen content of the LLZO samples from the measured amounts of cations with fixed charge leads to oxygen contents f< 12 for most samples, see Table 3.03. These oxygen vacancies may also affect the local occupancy of cation sites as well as activation barriers for Li migration.

Hence, a deeper understanding of the Li ion conductivity in Al stabilized LLZO might require much more information than the Al content; rather, detailed information on oxygen vacancy concentrations and local site occupancies might be key for in-depth knowledge.

Table 3.04: Four different spots with two pairs of comparable stoichiometry but different ionic conductivities. Cation compositions are averaged over the measured three depths, the value for the oxygen is calculated based on charge balance considerations.

Spots	σ_{Me} [Scm^{-1}]	composition
Li enriched 1	2.42×10^{-4}	$Li_{6.37}Al_{0.20}La_3Zr_{2.02}O_{12.04}$
Li enriched 2	0.56×10^{-4}	$Li_{6.35}Al_{0.18}La_3Zr_{2.03}O_{12.03}$
Li poor 1	2.54×10^{-4}	$Li_{6.13}Al_{0.28}La_3Zr_{2.01}O_{12.01}$
Li poor 2	0.79×10^{-4}	$Li_{6.12}Al_{0.26}La_3Zr_{2.02}O_{12.00}$

3.4 Conclusion

Several Al stabilized LLZO samples were chemically and electrochemically characterized. Microelectrode measurements revealed the existence of distinct local conductivity variation within individual samples, but also differences between nominally identical samples. Spatially

resolved LA-ICP-OES measurements were used to investigate the local chemical bulk composition. While the same composition was found between 5 and 100 µm depth, samples showed lateral gradients in the Al and Li content as well as deviations from the nominal values (on average too much Al, too little Li). However, no clear trend could be found how the elemental composition and its variation relates to the local ionic conductivity. Neither does a high (or low) Li content (between 6.1 pfu and 6.6 pfu) lead to particularly high ionic conductivities nor does a certain Al amount (between 0.15 pfu and 0.3 pfu) maximize the conductivity. This absence of a simple correlation between composition and conductivity indicates that there have to be other yet unknown parameters that have a pronounced effect on the conductivity. For example, the exact local crystal structure with varying site occupancy or oxygen vacancies might strongly affect the Li conduction paths and local activation barriers and could thus have a higher impact on the ionic conductivity of LLZO than the absolute local cation stoichiometry.

4 Investigating the electrochemical stability of $Li_7La_3Zr_2O_{12}$ solid electrolytes using field stress experiments

The study presented in this chapter has also been submitted as a scientific paper in "Journal of Material Chemistry A" (under review).

4.1 Introduction

One of the most important properties of an electrolyte material is its electrochemical stability. For an ideal solid electrolyte, a very wide electrochemical stability window (0.0–5.0 V vs. Li^+/Li) is required since it enables the highest voltage output of by coupling a lithium metal anode with a high voltage cathode material.

Despite intensive research int the last years, the electrochemical stability of LLZO is still an unsettled matter. Early experimental studies report a very wide electrochemical window ranging from 0 V vs. Li^+/Li to at least 5 V vs. Li^+/Li, implying the possible compatibility with high voltage cathode materials.[44,64,85] In contrast to that, density functional theory (DFT) calculations show a much narrower electrochemical window of 0.05–2.91 V vs. Li^+/Li.[130,131] According to these calculations, LLZO gets oxidized at 2.91 V to form Li_2O_2, $Li_6Zr_2O_7$, and La_2O_3.[130,131] The authors suggest that good stability observed in electrochemical experimental methods originates from kinetic stabilization.[130] In another computational study based on DFT calculations, Richards and et al.[132] report an oxidation potential of approx. 3.4 V vs. Li^+/Li.

Thompson et al.[133] showed that LLZO has a sufficiently large band gap of 6.4 eV to enable its use with high-voltage cathodes by combining direct current (DC) chronoamperometry, alternating current (AC) EIS, optical absorption band gap measurements and first-principles calculations. The authors claim that there is a difference between the intrinsic electrochemical window determined in their work and the narrower stability windows determined in prior calculations[130–132]: while their work examines the electrochemical stability, the earlier studies probed the chemical stability.[133] Furthermore, Thompson et al.[133] highlight that cyclic voltammetry (CV) used in earlier studies[44,64,85] is not suitable to determine the electrochemical stability of solid electrolytes.[133] Due to these controversial reports, it is obvious that more research is necessary to truly understand the stability behavior of LLZO.

In this work, the electrochemical stability of LLZO single crystals is investigated using field stress experiments in combination with subsequent electrochemical, chemical, and structural

analysis. DC voltages up to 3 V were applied in ambient air using ionically blocking Au electrodes in two different geometries. In a first set of experiments, macroscopic stripe electrodes were used to conduct field stress experiments at elevated temperatures. The effects induced by the polarization were investigated using ME-EIS, SEM, and LIBS. The revealed LLZO decomposition was further investigated using another set of experiments, in which individual microelectrodes were positively polarized against a macroscopic counter electrode. After these polarization experiments at elevated temperatures, compositional and structural changes within the material were investigated LA-ICP-MS and microfocus XRD, respectively. Strong Li-depletion beneath the microelectrodes is revealed, leading to the formation of Li-poor phases like $La_2Zr_2O_7$. The LLZO decomposition is still on-going even after several days of polarization and is also observable at room temperature, questioning if LLZO is compatible with high voltage cathode materials.

4.2 Experimental

4.2.1 LLZO synthesis

Two types of LLZO single crystals were used for the experiments: Ta stabilized LLZO (Ta:LLZO) with the nominal composition $Li_6La_3ZrTaO_{12}$ and Ga stabilized LLZO (Ga:LLZO) with the nominal composition $Li_{5.8}Ga_{0.4}La_3Zr_2O_{12}$. The single crystals were grown by the Czochralski method directly from the melt using previously dried high purity (99.99% or better) metal oxides or carbonates (in case of Li).

Ta:LLZO was grown from the stoichiometric melt of nominal composition which would naturally lead to the same composition of the grown crystal only if the compound melted congruently. This crystal was severely defective in its upper, first grown part where it contained expanded white opaque regions and many cracks. The last grown part, however, was transparent and colorless. In contrast, the Ga:LLZO was grown from a melt with 20 mol% Li_2O excess. Also this crystals was of low quality in its first grown part and transparent with yellow color in the last part.

The powder mixtures, either stoichiometric or Li_2O excessive, were pressed isostatically at 500 bar and sintered for 70 hours at 680 °C (Ta:LLZO) or 6 hours at 850 °C, consequently ground and pressed again at 2000 bar and sintered a second time at 1230°C for 6 hours (Ga:LLZO). The sintered material was melted in a 40 ml inductively heated iridium crucible under protective atmosphere (N_2 for Ta:LLZO, Ar for Ga:LLZO). In case of Ta:LLZO growth was initiated at

an Iridium wire that was dipped into the melt serving as a cold finger where formation of crystal nuclei was expected to occur when the melt was undercooled. For Ga:LLZO a roughly [100]-oriented small piece of crystal obtained in a previous experiment was used. In both cases, the wire, respectively the seed, was slowly pulled upwards at rates between 0.4 and 1.0 mm h^{-1} and the power of the generator was used to control the mass growth rate and therewith the diameter of the growing crystal (≈ 15 mm). Growth was stopped when about one third of the melt crystallized. The crystal was withdrawn from the melt and cooled down to room temperature in 15 h.

For the investigation described in this study, samples were prepared from the transparent last parts of both crystals. The chemical composition of the synthesized samples was determined via ICP-OES analysis. Sample compositions of $Li_{6.12}La_3Zr_{0.88}Ta_{1.03}O_{11.9}$ (normalized to 3 La pfu) and $Li_{6.43}Ga_{0.14}La_{2.84}Zr_2O_{11.68}$ (normalized to 2 Zr pfu) were determined for the Ta:LLZO and Ga:LLZO crystal, respectively. Accordingly, only about one third of Ga was incorporated during crystal growth. Details on the instrumental parameters used for the ICP-OES can be found in Table 4.01. More information regarding the chemical analysis of LLZO via ICP-OES can be found in Chapter 2.

Table 4.01: Instrumental settings ICP-OES bulk analysis

	Thermo iCAP 6500 RAD	
RF power	1200 W	
Radial observation height	12 mm	
Plasma gas flow (Ar)	12 l min^{-1}	
Nebulizer gas flow (Ar)	0.6 l min^{-1}	
Auxiliary gas flow (Ar)	0.8 l min^{-1}	
Integration time	5 s	
Replicates per sample	5	
Purge pump rate	1.6 ml min^{-1}	
Sample flow rate	0.8 ml min^{-1}	
Analytical wavelengths		
Eu (Internal standard)	281.396 nm (□)	381.967 nm (△)
Ga	417.206 nm*△	
La	333.749 nm□	412.323 nm*□
Li	610.362 nm△	670.784 nm*△
Ta	240.063 nm*□	268.517 nm*□
Zr	339.198 nm□	343.823 nm*□

* used for quantification
□/△ normalized to Eu 281.396/381.967 nm signal

Crystal slices with a thickness of about 1 mm were used for all experiments. To remove near surface reaction layers, the samples were polished by SiC grinding paper (P4000) directly before electrode preparation. Ionically blocking Au electrodes (100–200 nm thickness) were deposited by DC sputtering (MSC 010, Bal-Tec, Germany) at room temperature. Micro-structuring was performed using two different procedures. As first approach, photolithography in combination with subsequent ion beam etching was used. For the photolithography process, a negative photoresist (ma-N 1420, micro resist technology, Germany) in combination with a tetramethylammoniumhydroxid (TMAH) based, aqueous-alkaline, metal ion free developer (ma-D 533/S, micro resist technology, Germany) was employed. Additionally, the sample came into contact with distilled water (stopping the development process) as well as ethanol p.a. (removing remaining photoresist) during the procedure. As second approach for micro-structuring, direct sputtering using Ni shadow masks (Temicon GmbH, Germany) was applied.

Two different electrode configurations were used, which are illustrated in Figure 4.01. In both cases the bottom side of the samples was completely covered with an Au electrode.

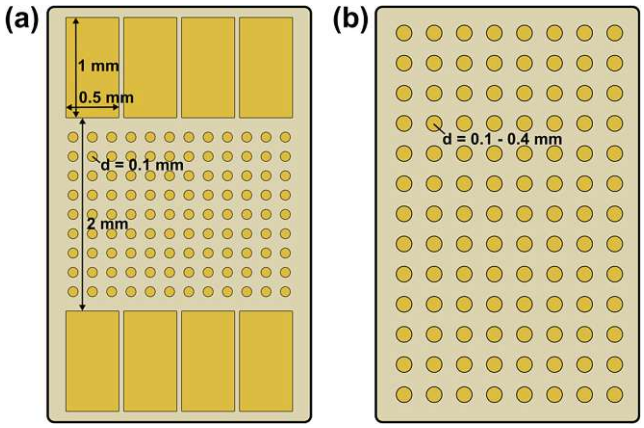

Figure 4.01: Schematic illustration of the used electrode configurations: a) macroscopic stripe electrode with circular microelectrodes in between and b) array of circular microelectrodes.

4.2.2 Field stress experiments

All experiments were performed at ambient air either at elevated temperatures (350–400 °C set) or at room temperature. The sample was heated from below via a lab-built heating unit. Since the temperature is controlled by a thermocouple inside the heating unit, the actual sample temperature is lower than the set temperature by approx. 30–50 °C[134]. The elevated temperature is expected to strongly accelerate decompositional phenomena due to kinetic reasons and can be regarded as a kind of "highly accelerated life test" (HALT) often performed to test the

stability of electronic devices. A 2611 Source Measure Unit (Keithley Instruments, USA) was used as voltage source and measurement unit. Au needles were employed to contact the (micro)electrodes under an optical microscope using micromanipulators to adjust the position of the needles.

Polarization of stripe electrodes

The impact of electric field stress on the electrochemical properties of LLZO was first investigated using the stripe electrode configuration shown in Figure 4.01a. A polarization voltage of 3 V was applied at 400 °C (set temperature) via two opposing macroscopic stripe electrodes on the top side of a Ta:LLZO single crystal. After the polarization voltage was applied for 15 h, the sample was cooled to room temperature by switching off the heating unit. To avoid relaxation of polarization effects, the voltage was still applied during cooling.

Locally resolved EIS measurements were performed to investigate the impact of the field stress on the conductivity behavior of the material. For that purpose, a row of microelectrodes located between the macroscopic polarization electrodes was analyzed before as well as after the polarization experiment. Measurements were performed at room temperature using the Au layer on the bottom side of the sample as counter electrode. An Alpha-A high performance frequency analyzer (Novocontrol Technologies, Germany) and a frequency range of 1 to 500 kHz was used for all EIS measurements. The obtained impedance spectra were fitted according to Ref.[89] analogue to the ME-EIS measurements described in Section 3.3.3. From the spreading resistance R_{spread} and the microelectrode diameter d, the local ionic conductivity of the probed sample volume σ_{Me} was calculated using Equation 3.02.[122]

After polarization, the morphology of the electrodes was investigated via SEM using a Quanata 200 instrument (FEI, USA) operated at 10 kV acceleration voltage. EDX was conducted to investigate the material deposited on the cathode using an Octane Pro Silicon Drift detector (EDAX, USA) equipped on the instrument. To prevent electrostatic charging, the samples were coated with Au prior to the SEM analysis.

LIBS was used to gain spatially resolved information about the chemical composition of the sample. For that purpose, line-scans across the polarization axis were performed after the polarization experiment and EIS measurements were finished. Prior to each experiment, a pre-ablation line-scan removing the electrodes was carried out to avoid that the obtained signals are affected by the Au on top of the sample. Measurements were performed using a commercially

available J200 LIBS system (Applied Spectra Inc., USA) equipped with a 266 nm frequency quadrupled Nd:YAG laser and a six-channel Czerny-Turner type spectrometer covering a wavelength range from 188 to 1048 nm. LIBS data was collected using Axiom 2.0 software provided by the manufacturer. Details on the instrumental parameters used for the LIBS measurements can be found in Table 4.02.

Table 4.02: Instrumental setting LIBS analysis

LIBS instrumentation	J200
Pulse duration	5 ns
Output energy	1.5 mJ
Beam diameter	100 µm
Scan speed	0.1 mm s^{-1}
Repetition rate	10 Hz
Beam geometry	circular
Gate delay	0.5 µs
Gate width	1.05 ms
Atmosphere	Ar

Polarization of microelectrodes

The decomposition behavior of Ta:LLZO as well as Ga:LLZO single crystals was further investigated using the microelectrode configuration shown in Figure 4.01b. Voltages up to 2.4 V was applied on individual microelectrodes using the Au layer on the bottom side of the sample as counter electrode. Field stress experiments with a stepwise voltage increase (0.2 V step size; 1.4 h holding time) as well as constant voltage measurements (2 V polarization voltage; 0.5–336 h holding time) were conducted, primarily at 350 °C (set temperature).

LA-ICP-MS was used to investigate field stress induced changes in the chemical composition. For the investigation, multiple line-scans across the polarized microelectrodes were performed. An untreated electrode was always investigated together with a polarized electrode and was used as reference measurement. An iCAP Qc quadrupole ICP-MS (Thermo Fisher Scientific, Germany) coupled to a NWR213 laser ablation system (ESI, USA) equipped with a 213 nm Nd:YAG laser and a fast-washout ablation cell always positioned above the actual ablation site was employed. Qtegra software provided by the manufacturer of the instrument was used for data acquisition. Prior to the experiments, the tune settings of the MS instrumentation were optimized for maximum ^{115}In signal using a NIST 612 trace metal in glass standard (National

Institute of Standards and Technology, USA). Detailed information about the used instrumental settings can be found in Table 4.03. The sampling depth of the experiment was determined using a DektakXT profilometer (Bruker, USA).

Table 4.03: Instrumental setting LA-ICP-MS analysis

Laser ablation system	ESI NWR213
Average fluence	3.0 J cm^{-2}
Laser diameter	60 µm
Scan speed	15 µm s^{-1}
Repetition rate	20 Hz
Carrier gas flow (He)	0.6 l min^{-1}
Make-up gas flow (Ar)	0.8 l min^{-1}
ICP-MS instrumentation	**Thermo iCAP Q**
Auxiliary gas flow (Ar)	0.8 l min^{-1}
Cool gas flow (Ar)	14 l min^{-1}
Dwell time per isotope	10 ms
RF power	1550 W
Cones	Ni
Mass resolution	m/Δm = 300
Measured isotope	^{7}Li, ^{90}Zr, ^{138}La, ^{181}Ta

XRD measurements were performed using an Empyrean diffractometer (Malvern Panalytical, Germany) equipped with a focusing mirror, a 0.3 mm microfocus, and a GaliPIX3D detector. Cu Kα radiation (45 kV, 40 mA) and a 2θ scan range from 20° to 80° was used. For the measurements, the x-ray beam was focused on individual microelectrodes. All scans were done with a measuring time of 4.5 h per sample. The obtained diffractograms were analyzed using Panalytical Highscore[116].

4.3 Polarization of stripe electrodes

The approach of the first type of field stress experiments is summarized in Figure 4.02. A polarization voltage of 3 V was applied at elevated temperatures (400 °C set) using macroscopic Au stripe electrodes (Figure 4.02a). Before and after the polarization experiment, locally resolved conductivity measurements along the polarization axis were performed via microelectrode EIS measurements at room temperature (Figure 4.02b). In a final step, field stress induced changes in the chemical composition were investigated using LIBS (Figure 4.02c).

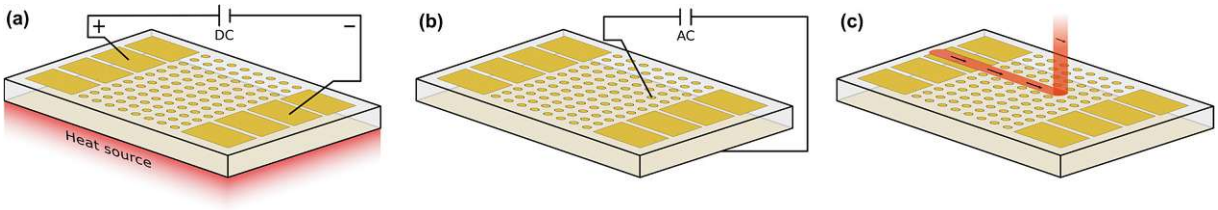

Figure 4.02: Schematic illustration of a polarization experiment with strip electrodes. (a) Application of field stress via two opposing macroscopic Au electrodes, (b) laterally resolved conductivity determination via microelectrode EIS measurements, and (c) laterally resolved chemical analysis via a LIBS line scan analysis.

4.3.1 Morphology changes

During the polarization experiment, the stripe electrodes undergo severe optical changes, indicating that electrochemical reactions take place. Figure 4.03 shows various micrographs of the electrodes before, during, and after the polarization. At the negatively polarized electrode (cathode), a solid is deposited during the polarization. The optical appearance of the electrode changes continuously over the duration of the experiment (Figure 4.03a–d), indicating an on-going reaction. SEM images reveal that a solid is formed beneath as well as on top of the Au layer (Figure 4.03e–g). Most likely, Li_2CO_3 or another Li-containing salt (LiOH, Li_2O) is formed due to the reduction of O_2 from air in presence of CO_2 and H_2O, e.g.:

$$2\ Li^+ + 2\ e^- + CO_2 + ½\ O_2 \rightarrow Li_2CO_3$$

Accordingly, oxygen is reduced at this electrode. This is confirmed by the EDX spectrum of the deposited solid (Figure 4.03h). Beside Au, most likely originating from sample coating prior to the SEM analysis, only C and O can be observed. This shows that the deposited substance does not contain La, Zr, or Ta, leaving only Li as a possible cation (Li cannot be detected by conventional EDX). In principle, this electrochemical reaction is expected to occur close to the triple phase boundaries. The fact that large parts of the electrode surface are covered by reaction products indicates that also the Au layer becomes porous during the field stress experiment.

The positively polarized electrode (anode) shows a rough surface after polarization (Figure 4.03i–k). The roughness appears to be caused by gas bubbles, possibly arising from O_2 formation due to oxidation of oxide ions, lifting parts of the electrode from the sample surface. To compensate the occurring loss of O^{2-} ions, negatively charged Li vacancies need to be created, ultimately leading to either (1) LLZO with a sub-stoichiometric amount of O^{2-} and Li^+:

$$Li_7La_3Zr_2O_{12} \rightarrow Li_{7-2x}La_3Zr_2O_{12-x} + x/2\ O_2 + 2x\ Li^+ + 2x\ e^-$$

or (2) the formation of Li-poor phases such as $La_2Zr_2O_7$ and La_2O_3:

$$Li_7La_3Zr_2O_{12} \rightarrow La_2Zr_2O_7 + ½\ La_2O_3 + 7/4\ O_2 + 7\ Li^+ + 7\ e^-$$

The substitution element is not considered in the given reaction Equations for simplicity reasons. Additional decomposition products might be formed due the presence of a dopant (e.g., $LaTaO_3$ in case of Ta). The formation of $La_2Zr_2O_7$ due to electric field stress is confirmed by XRD later in this work (see Figure 4.13).

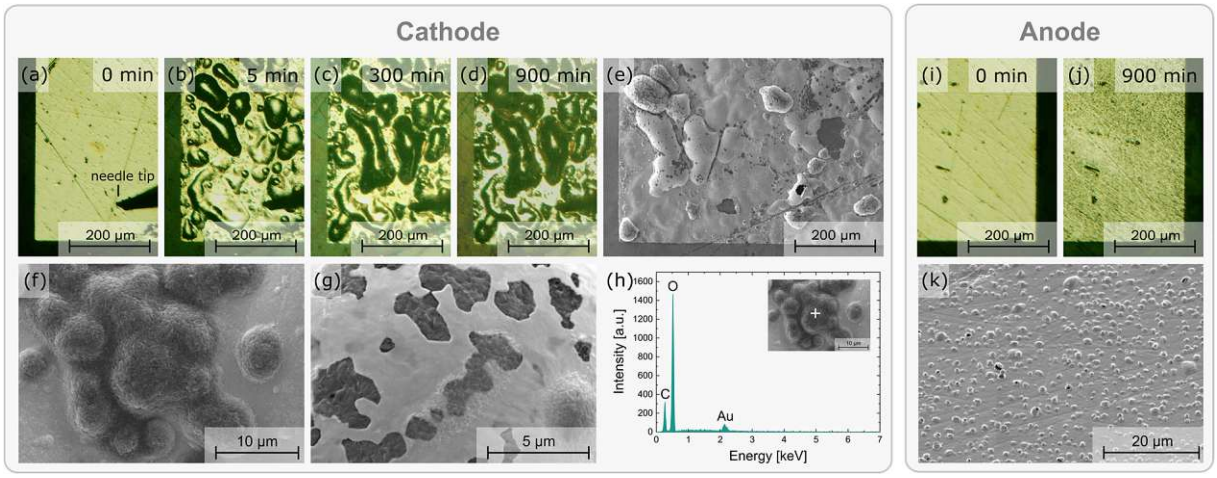

Figure 4.03: Optical microscopy images of a negatively polarized Au electrode (3 V, 400 °C set temperature) before (a), during (b+c), and after (d) the experiment. SEM images (e–g) and EDX spectrum (h) of the deposited solid, most likely Li_2CO_3. Optical microscopy and SEM images of the corresponding positively polarized electrode before (i) and after (j+k) the experiment, indicating gas (O_2) formation beneath the electrode.

The measured current flowing through the sample during polarization (Figure 4.04) is also in accordance with the assumption of a continuous electrochemical reaction. After a rapid decrease within the first minutes of the experiment, the current stabilized and remained at approx. 1 µA for the rest of the measurement. Given the electrode and sample geometry (distance between electrodes = 2 mm; cross section = 0.5 mm^2), an electronic conductivity of about 1.3×10^{-5} S cm^{-1} would be necessary to reach such a high steady-state current, which is unlikely considering the values reported in literature (5×10^{-12} – 2×10^{-9} S cm^{-1} at room temperature[37,77,133] and in the range of 10^{-7} S cm^{-1} at 350 °C[135]). The measured current is therefore attributed to continuous decomposition of the sample caused by field stress, and thus largely Li^+ current.

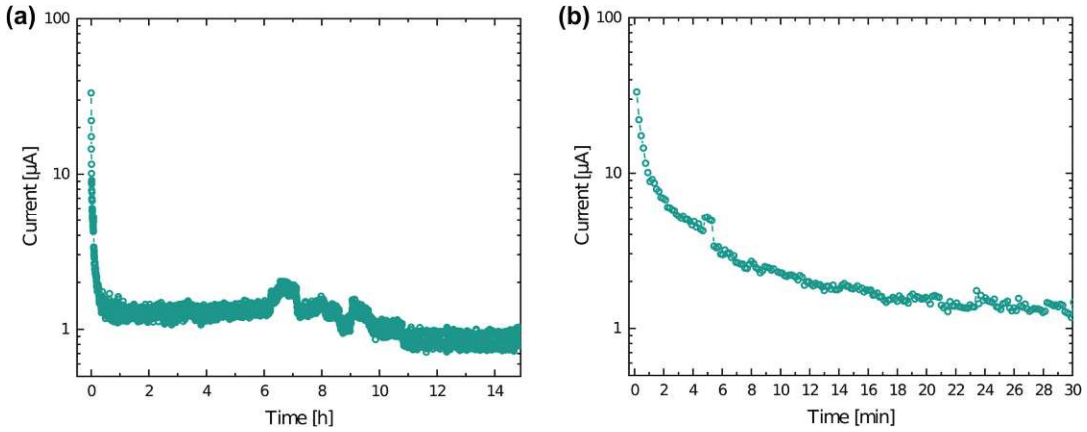

Figure 4.04: Current measured during polarization (3 V) via stripe electrodes at 400 °C (set temperature). While (a) shows the entire experiment, (b) shows a magnified view of the first 30 min. A rapid current drop in the first few minutes of the experiment is observable, which is followed by a stabilization of the current in the 1 µA range. Minor current fluctuations are visible in the time interval between 6 and 11 h, most likely caused by Li_2CO_3 and/or O_2 formation impacting the electrode/electrolyte interface.

4.3.2 (Electro)chemical analysis

In Figure 4.05 the impact of the field stress on the conductivity behavior as well as the chemical composition of the material is visualized. Figure 4.05a shows the local conductivity along the polarization axis before and after the bias was applied. The local conductivity measurements were performed via microelectrode EIS measurements using the Au layer on the bottom side as counter electrode (see Figure 4.02b). To better illustrate the impact of the polarization, the relative differences of these two conductivity measurements are shown in Figure 4.05b.

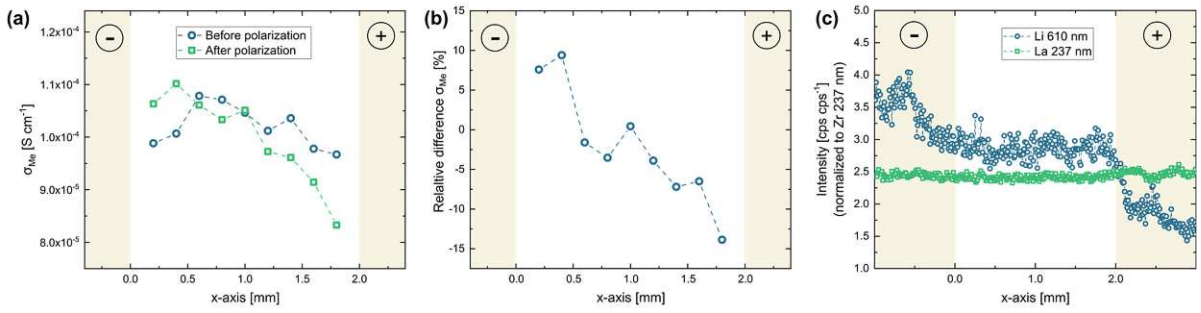

Figure 4.05: Locally resolved investigation of the effects of a stripe electrode polarization experiment (3 V, 400 °C set temperature): (a) local conductivity before and after the experiment probed via microelectrode EIS measurements, (b) relative conductivity change for the individual electrodes, and (c) chemical analysis at and between the electrodes measured via LIBS. The results show significant changes of the conductivity behavior between the electrodes as well as strong Li stoichiometry variations at the electrodes, confirming that an electrochemical reaction takes place.

Since most of the voltage between a microelectrode and a macroscopic counter electrode drops very close to the microelectrode, only the sample volume close to the microelectrode is probed by the measurement, thus providing laterally resolved information.[111] Typical impedance spectra found in these measurements are shown in Figure 4.06. The charge transport in the probed sample corresponds to the high frequency arc visible in the spectra, which is described by a resistive element (R_{Spread}) in the equivalent circuit. Detailed information regarding the evaluation of microelectrode EIS measurements performed on LLZO can be found in Section 3.3.3 and Ref.[89].

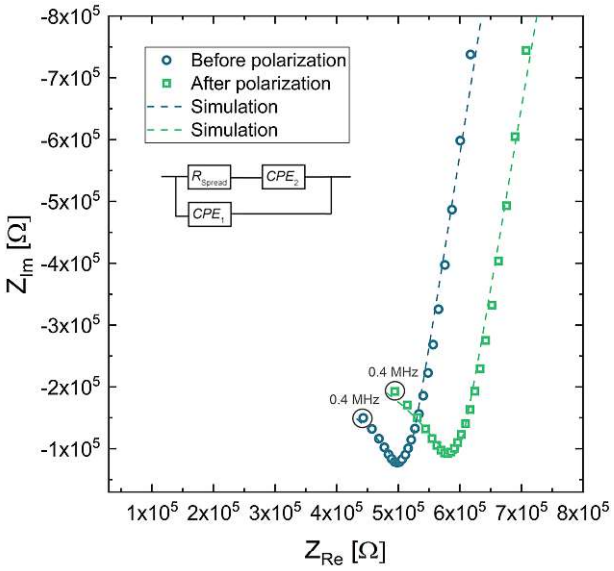

Figure 4.06: Exemplary impedance spectra of microelectrode EIS measurements performed at room temperature on the same electrode before and after a polarization experiment. The corresponding fits (dashed lines) are based on the shown equivalent circuit. The high frequency arc is strongly affected by the applied field stress, which corresponds to changes in the charge transport properties of the sample.

The microelectrode measurements reveal a clear impact of the polarization experiments on the conductivity behavior of the material. While the local ionic conductivity increased close to the cathode, the opposite effect can be observed close the anode: The conductivity decreased up to 15 % (see Figure 4.05a+b). Interestingly, this effect cannot be correlated to changes in the Li stoichiometry, since chemical analysis via LIBS did not reveal any variations of the Li content between the electrodes (Figure 4.05c). The changes in the conductivity behavior were therefore either caused by Li stoichiometry changes too small to be observed via the LIBS measurements, or by other factors like local variations of site occupancies or oxygen vacancies[128]. However, in contrast to the region between the electrodes, the LIBS analysis revealed huge variations in Li very close and/or beneath the stripe electrodes with almost no change in La. While an increased Li content can be observed on the cathode, most likely due to the formation of Li_2CO_3 as already confirmed by EDX (see above), the Li concentration strongly decreased at the anode,

confirming the presence of Li-poor phases and/or LLZO with a Li^+ sub-stoichiometry. The results thus confirm that the applied electric field stress leads to an electrochemical reaction decomposing the material.

To summarize the findings of the experiments, the processes taking place during sample polarization are visualized in Figure 4.07. As already discussed, O-ions of LLZO are oxidized and O_2 from the surrounding air is reduced at anode and cathode, respectively. Overall, Li-ions are transported through the sample, first leaving vacant Li^+ sites as well as O-vacancies in LLZO at the anodic side, and ultimately leading to the formation Li-poor phases like $La_2Zr_2O_7$.

Please note: the conducted experiments shows that LLZO decomposes when a bias of 3 V is applied at 400 °C, but this does not mean that the electrochemical window of LLZO is < 3 V. The reason for this is that the Li chemical potentials of neither the cathode nor the anode is fixed, since ionically blocking Au electrodes are used on both sides.

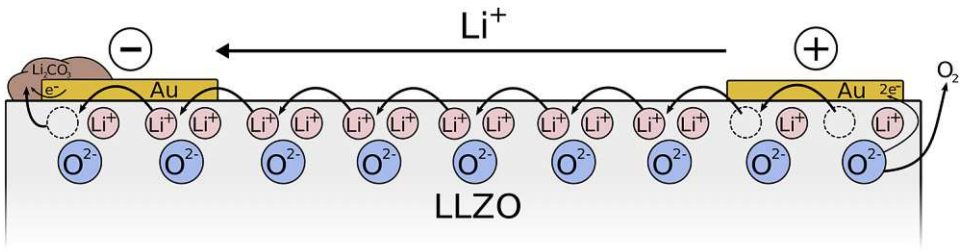

Figure 4.07: Schematic illustration of the processes induced by LLZO polarization via stripe electrodes. Li-containing salts like Li_2CO_3 are deposited at the cathode due to the reduction of O_2 from air in presence of CO_2 and H_2O. On the anode, O_2 is formed due to oxidation of oxide ions, leading to LLZO with sub-stoichiometric amount of O^{2-} and Li^+ and/or Li-poor phases. During the reaction, Li-ions are constantly transported from the anode to the cathode.

4.4 Polarization of microelectrodes

To investigate the decomposition behavior of LLZO under electric field stress in more detail, individual Au microelectrodes on Ta- as well as Ga stabilized single crystals were positively polarized in ambient air under various conditions. The used measurement setup is visualized in Figure 4.08. Since the area of the macroscopic Au counter electrode is several orders of magnitude larger than the area of the microelectrode, only very minor material changes are expected at the macroscopic electrode. It can therefore be assumed, that the chemical potentials of LLZO at the counter electrode does not vary significantly during polarization despite its ionically-blocking character, making the used configuration somehow comparable to the Hebb-Wagner polarization technique with one reversible electrode.

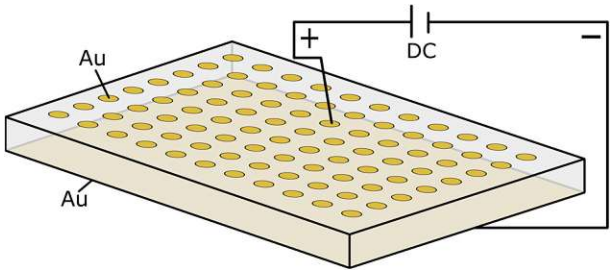

Figure 4.08: Schematic illustration of a polarization experiment using microelectrode configuration. Au microelectrodes with a diameter ranging from 100 to 400 µm were utilized. An Au layer covering the whole bottom side of the sample was used as counter electrode.

4.4.1 Stepwise voltage increase

In a first set of experiments, which were performed at elevated temperature (350 °C set), the applied voltage was stepwise increased until a final voltage of 2.4 V was reached. Figure 4.09 shows the results of such measurements for a Ta- as well as a Ga stabilized LLZO single crystal. For both samples, a strong current increase can be observed at the first few voltage steps. Interestingly, the current behavior changes drastically at 1.2 V and 1.4 V for Ta:LLZO (Figure 4.09a) and Ga:LLZO (Figure 4.09b), respectively. The current stops increasing with the applied voltage and instead becomes more and more voltage independent for the later voltage steps. This significantly different behavior in the two different voltage regimes indicates that fundamentally different processes are limiting the charge transfer. This hypothesis is further confirmed by the time-dependencies within the individual voltage steps, also showing significantly different behavior: while in the low-voltage regime the current decreases very fast at the beginning of each voltage step, quickly leading to a constant "steady-state"-type current (Figure 4.09c), the current decrease is relatively flat in the high-voltage regime.

To better visualize the relationship to the applied voltage, the measured currents for each voltage step are plotted on a logarithmic scale in Figure 4.09d. In this plot, the currents measured at the end of the corresponding voltage step are shown, representing the "stabilized" current obtained when voltage is applied for a certain time. It becomes clear from the time dependencies in Figure 4.09a+b that this does not represent a true steady-state current for the high-voltage regime, but the prevailing trends are well accessible. Interestingly, an almost exponential current increase can be observed for the lower voltages (0.2–1.0 V). The origin of the steady-state current in the regime has not been investigated in detail so far. However, electron conduction is a likely explanation with realistic conductivity values in the 10^{-9} S cm^{-1} range. In the high-voltage regime (1.4–2.4 V), the measured currents are nearly constant for

each voltage step, once more confirming the distinctly different conductivity behavior for higher voltages. Constant voltage experiments presented later in this work reveal that LLZO decomposition is the main source of current if a voltage of 2 V is applied on the material. Most probably the entire constant current regime is characterized by the same electrochemical process which indicates that already at 1.2–1.4 V LLZO decomposition takes place. The two different regimes (electron conduction and LLZO decomposition) are also indicated in Figure 4.09d.

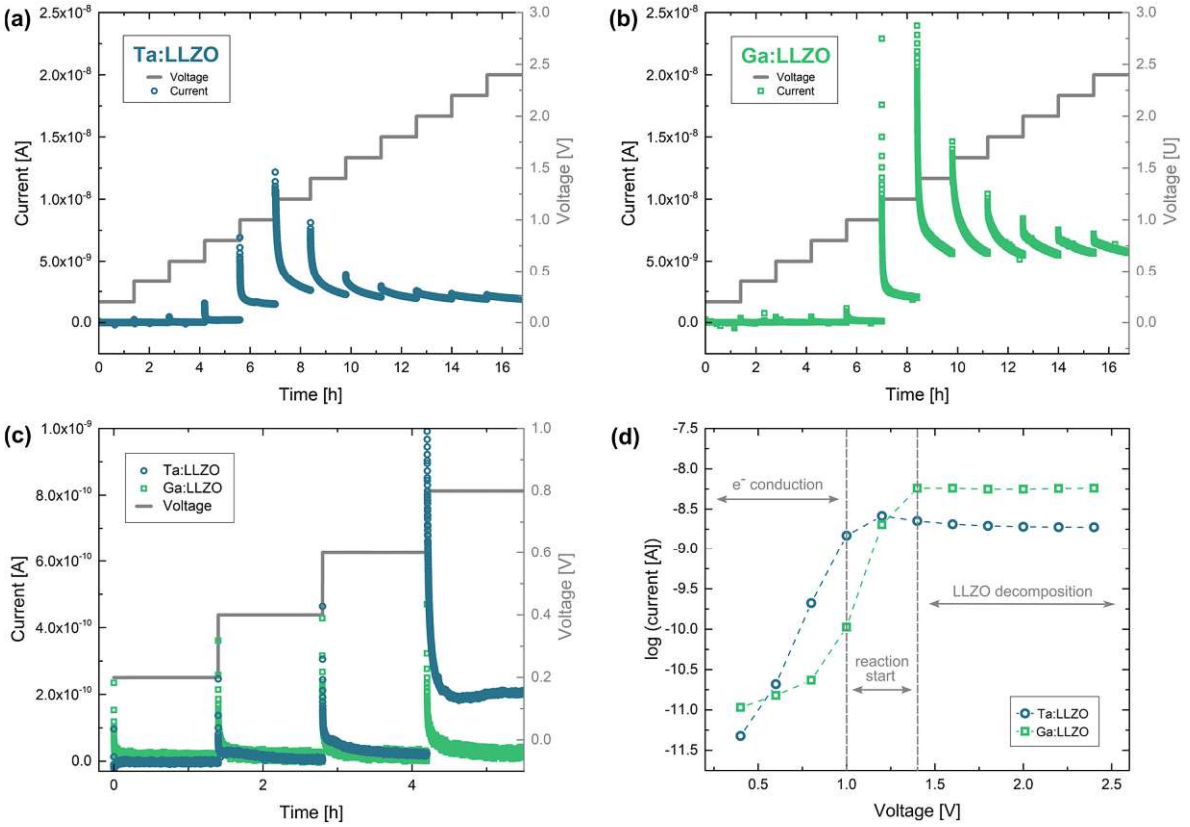

Figure 4.09: Polarization of Au microelectrodes with stepwise voltage increase (0.2 V step size, 1.4 h holding time, 350 °C set temperature, 100 µm electrode diameter). Current-time profiles for (a) Ta:LLZO and (b) Ga:LLZO single crystals as well as (c) a zoomed-in plot for the lowest voltages and (d) the "stabilized" currents at the end of each voltage step, plotted on logarithmic scale. After increasing until 1.2–1.4 V, the measured currents stay constant for higher voltages, indicating a voltage independent decomposition reaction in this range.

To make any conclusion about the electrochemical stability window of the material, it is necessary to know the chemical potential of Li at the ionically blocking counter electrode, which hardly changes in this experiment (see above) but is not truly well defined in this case. This chemical potential has to be estimated. Since during synthesis of the single crystals the material is surrounded by Li_2O in the gas phase, the chemical potential of Li in LLZO is very likely defined by Li_2O (around 2.9 V vs. Li^+/Li[136]). Accordingly, also the counter electrode is

at 2.9 V vs. Li^+/Li. From the experiments a stability limit of 4.1–4.3 vs. Li^+/Li at this elevated temperature can thus be concluded. These finding are in agreement with theoretical studies claiming that the extended electrochemical window of LLZO observed in other experimental studies originates from kinetic stabilization.[130,131]

4.4.2 Constant voltage

To further investigate the decomposition behavior of LLZO, individual Au microelectrodes were polarized with constant voltage for different time intervals (0.5–66 h). 2 V was chosen as fixed voltage, since (1) it ensures a maximum decomposition rate (cf. Figure 4.09), and (2) corresponds to 4.9 V vs. Li^+/Li according to used estimation of the counter electrode's chemical potential and therefore simulates the typical voltage range of high-voltage lithium (ion) batteries. Like in the previous experiments, the electric field stress was applied at elevated temperatures (350 °C set) to enhance the kinetics of the LLZO decomposition. A typical current profile of such a polarization is shown in Figure 4.10. The measured current decreases over time but stays relatively high (> 0.5 nA, i.e., a current density of 6 µA cm^{-2} with respect to the microelectrode) even after several days of polarization, indicating an on-going electrochemical process. Translating the final current to a hypothetical bulk resistivity via the spreading resistance formula (Equation 3.02) a value of 1.5×10^{-8} S cm^{-1} is obtained. Electron conduction is thus a feasible candidate for the remaining current. However, in the following it is shown that a significant part of this current is ionic.

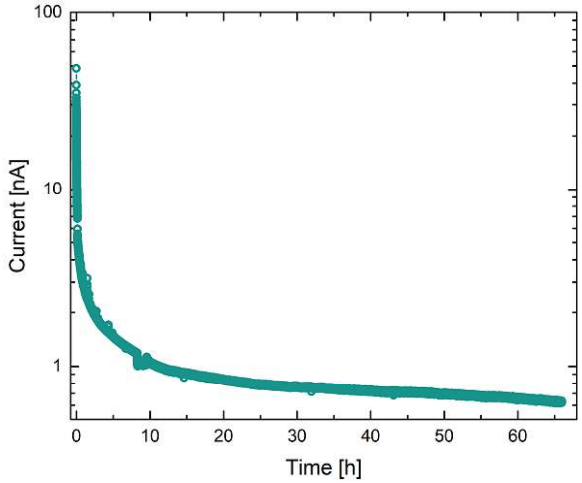

Figure 4.10: Typical current profile for a microelectrode constant voltage polarization experiment (Ta:LLZO single crystal, 2 V voltage, 66 h polarization time, 350 °C set temperature, 100 µm electrode diameter). The measured current decreases over time but stays above 0.5 nA even after several days of polarization, indication an on-going decomposition reaction.

Chemical analysis

After the polarization experiment, the chemical composition beneath the electrodes was probed via LA-ICP-MS. Figure 4.11 shows the results of such an LA-ICP-MS analysis for a Ta:LLZO single crystal. Significant changes of the chemical composition can be observed, confirming that LLZO decomposition was induced by the applied voltage. This is in agreement with the LIBS analysis shown in the previous section, also revealing stoichiometry changes due to electric field stress (cf. Figure 4.05c). For the LA-ICP-MS analysis, line-scans across the microelectrodes were used, whereas each line-scan covered one polarized as well as one untreated electrode. The untreated electrodes served as reference, showing that the analyte signals are not affected by the Au electrode on top of the sample. In contrast to that, a significant decrease of the Li signal can be observed when a polarized electrode is probed, which corresponds to a Li-depletion beneath the electrode. Interestingly, also all other analytes seem to be affected by the polarization, since the signals of La, Zr, and Ta signals increase at the electrode (Figure 4.11a). However, the signal ratios of La, Zr, and Ta stay constant, meaning that only Li-stoichiometry was changed by the polarization. Most likely, the applied field stress induced phase changes which altered the ablation behavior of the material, thereby affecting the signal intensities of all analytes.

In Figure 4.11b+c, the obtained Li signal is normalized to the intensity of the corresponding Zr signal. In the normalized signal, variations in material ablation during the measurement are compensated, making it a good representation of the Li-stoichiometry. A decrease of up to 83 % can be observed for the longest polarization time (66 h), confirming that Li-ions are strongly depleted in the topmost sample layer beneath the electrode. Comparing different polarization times shows that the observed Li-depletion steadily increases over time (Figure 4.11b). This indicates that the induced LLZO decomposition is on-going even after several days of polarization and is not stopped by the formation of an interface layer.

To investigate effects deeper inside the material, each electrode was analyzed two more times after the initial LA measurement. Each ablation pass removed approx. 2 µm material, giving access to (rough) depth-resolved information. In Figure 4.11c, the three measurements of the longest polarized electrode (66 h) are compared. The induced Li-depletion is less pronounced for every subsequent ablation pass, however, even for the third and last sample layer significant effects (30 % decrease) can be observed. This means that even in a sample depth of approx. 4–6 µm material changes have been induced by the applied field stress. Given the fact the effect is relatively small for the third layer and is not observable at all for electrodes with lower polarization times, it still can be assumed that most of the affected sample is probed by the analysis.

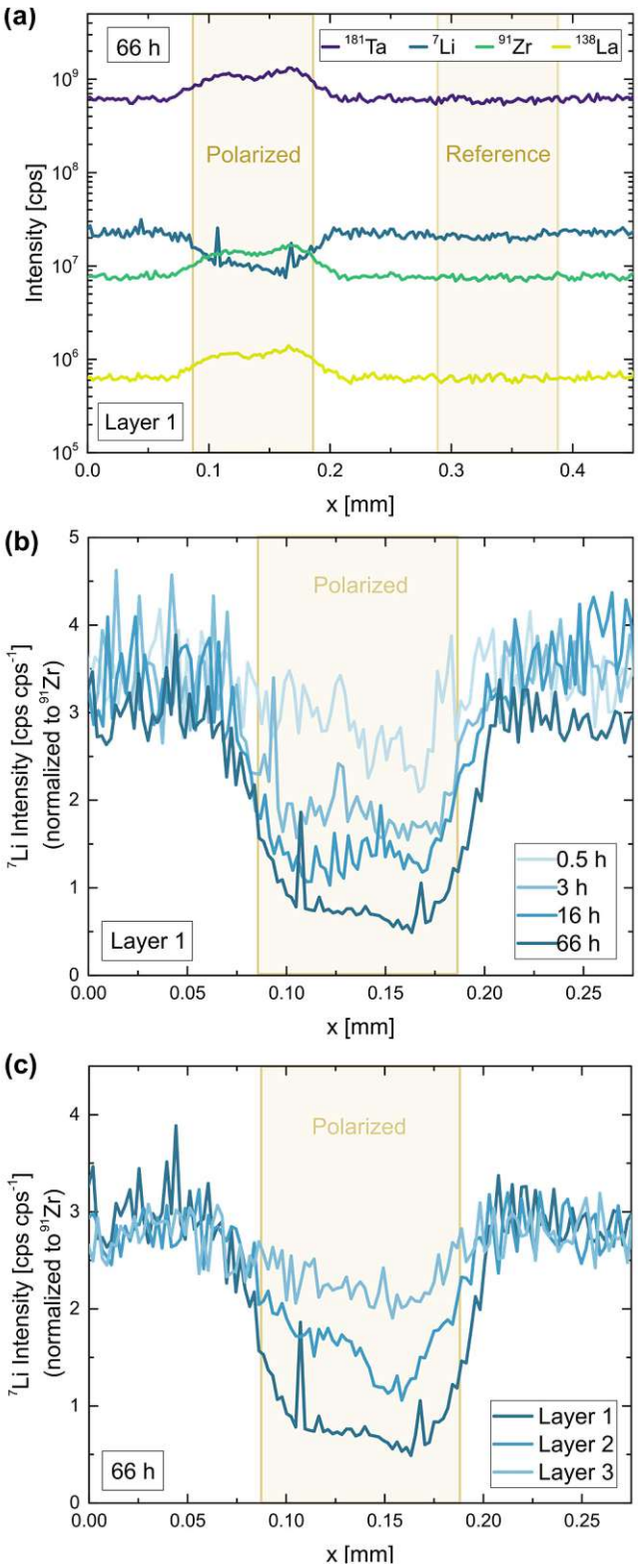

Figure 4.11: LA-ICP-MS analysis of a Ta:LLZO single crystal after a constant voltage experiment (2 V voltage, 0.5–66 h polarization time, 350 °C set temperature, 100 µm electrode diameter). (a) Raw signal intensities corresponding to a polarized (66 h) as well as an untreated electrode. Normalized Li signal for (b) different polarization times and (c) subsequent ablation passes. Significant Li-depletion beneath the electrode is induced by the applied field stress, getting more pronounced even after several days of polarization.

To investigate if the relatively high currents during electrode polarization were indeed caused by the observed Li-depletion, the total amount of transported Li-ions Li^+_{trans} was estimated using the measured stoichiometry changes. The Equation

$$Li^+_{trans} = Li^+_{cell,ref} \cdot \left(1 - \frac{I^{pol}_{6Li/91Zr}}{I^{ref}_{6Li/91Zr}}\right) \cdot \frac{V_{prob}}{V_{cell}} \cdot \frac{1}{N_A} \text{ [mol]} \qquad (4.01)$$

was used for the calculation, where $Li^+_{cell,ref}$ is the number of Li-ions in the cubic LLZO unit cell considering the sample stoichiometries determined via ICP-OES (49.0 Li^+ Ta:LLZO, 51.4 Li^+ Ga:LLZO), $I^{pol\,(ref)}_{7Li/91Zr}$ the normalized Li intensity of the polarized (reference) microelectrode [cps cps^{-1}], V_{prob} the probed sample volume [m^3], V_{cell} the volume of a cubic LLZO unit cell (2.188×10^{-27} m^3 [41]), and N_A Avogadro constant (6.022×10^{23} mol^{-1}). V_{prob} was calculated based on the crater depth and the electrode size, assuming that the Li-ion transport occurs uniformly beneath the electrode. The probed sample depth for the individual line scans was defined using the La signal of the analysis.

Figure 4.12a shows the calculated amounts of transported Li-ions for the already discussed polarization series on Ta:LLZO (cf. Figure 4.11). The LA-ICP-MS determination is compared to values obtained from the corresponding current measurements, calculated under the assumption that all measured current solely originates from irreversible transport of Li-ions. The values obtained from the current profiles are generally higher and the relative difference increases with increasing polarization time. However, the results of both quantification approaches show a very similar trend and are in the same order of magnitude even for the longest polarization experiments. This reasonable agreement thus confirms that a substantial part of the polarization current is indeed caused by LLZO decomposition and the associated Li-depletion beneath the anode. The deviation between the values obtained by LA-ICP-MS and DC measurements might be caused by several reasons, namely (1) contribution of other processes (e.g., electronic conduction) to the total current, (2) inaccuracies of the assumptions used for the calculations (e.g., non-uniform Li-ion transport beneath the electrode), and (3) additional Li-depletion deeper in the material not probed by the LA analysis.

An analogue series of polarization experiments performed on a Ga:LLZO single crystal shows very similar results (Figure 4.12b). The total amount of transported Li-ions is significantly higher compared to Ta:LLZO, which is in agreement with the higher decomposition current found in the polarization experiments with stepwise voltage increase (cf. Figure 4.9). Beside that, the only observable difference was a higher ablation rate for Ga:LLZO during the LA

experiment (about 3 µm per ablation pass). Overall, the substitution element only seems to affect the decomposition rate, not the process itself.

While in all previously shown experiments, micro-structuring was performed using a combination of photolithography and ion beam etching, the microelectrodes used for the experiment series on Ga:LLZO were prepared via direct sputtering using a Ni shadow mask. Since this process is solvent-free, it can be excluded that contact with protic solutions during photolithography (see Experimental), potentially leading to Li^+/H^+ exchange[39,81,137], is the reason for the observed phenomena.

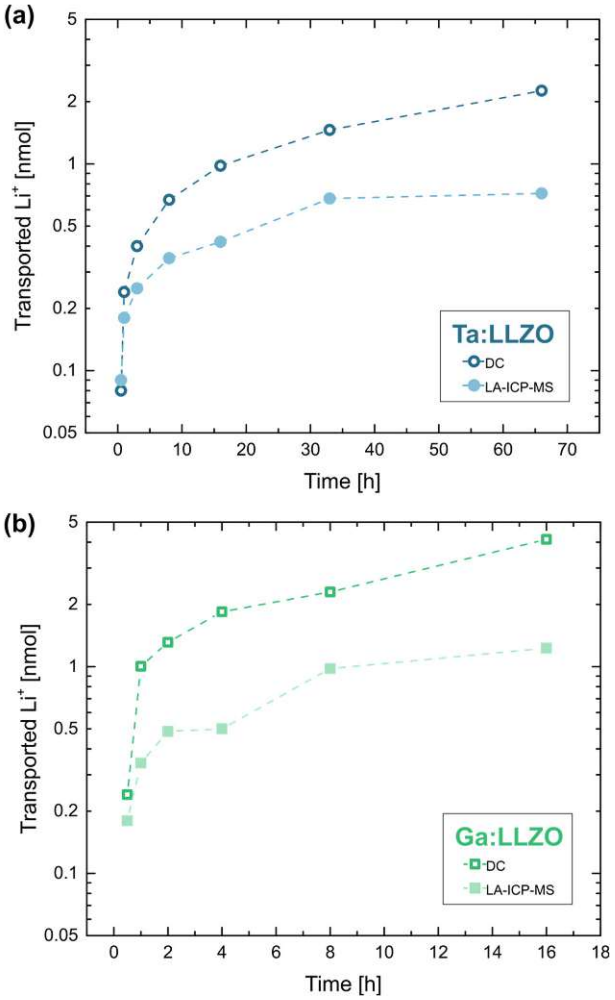

Figure 4.12: Total amount of transported Li-ions during electrode polarization (2 V voltage, 350 °C set temperature, 100 µm electrode diameter) determined via LA-ICP-MS as well as DC measurements, for (a) Ta:LLZO (0.5–66 h polarization time) and (b) Ga:LLZO (0.5–16 h) single crystals. The values obtained from the current profiles are generally higher but are in the same order of magnitude even for the longest polarization experiments, confirming that most of the polarization current is caused by LLZO decomposition.

Structural analysis

Due to the strong Li-depletion beneath the electrode, (cf. Figure 4.11), it is to be expected that Li-poor phases are formed during the polarization. To investigate these structural changes, polarized electrodes were investigated using microfocus XRD and compared to pristine electrodes (Figure 4.13). Additional reflexes can be observed in the diffractogram, showing that $La_2Zr_2O_7$ was formed during the experiment. The results confirm the decomposition reaction proposed in Section 4.3.1: at the anode O^{2-} is oxidized, leading to the formation of $La_2Zr_2O_7$ and La_2O_3. Additionally, also LLZO with a sub-stoichiometric amount of O^{2-} and Li^+ might be formed to some extent.

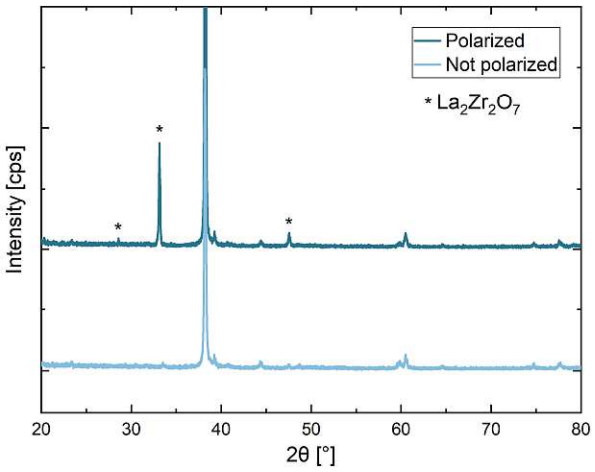

Figure 4.13: Microfocus XRD measurement after a constant voltage polarization experiment (2 V voltage,120 h polarization time, 350°C set temperature, 400 µm electrode diameter). $La_2Zr_2O_7$ was formed due to applied electric field stress.

This also raises the question of the species carrying the current across this zone with decomposition products. This is certainly strongly dependent on the exact 3D distribution of the reaction products in this reaction zone. A simple layer-by-layer structure can hardly be expected. However, we may face a situation where not only Li^+ transport but also oxide ion transport and electron transport may play a role (see sketch in Figure 4.14). Owing to the lack of reducible cations, Li-depletion in LLZO most probably takes place via formation of oxygen vacancies. Substantial oxygen vacancy concentrations and O^{2-} conduction in LLZO was already confirmed in Ref.[128]. Any further depletion of Li within an LLZO phase (forms $Li_{7-2x}La_3Zr_2O_{12-x}$) thus requires oxide ion conduction in LLZO (path 1 in Figure 4.14). Depletion of Li in LLZO without direct contact to the electrode requires further conduction of O^{2-} also in a reaction product (path 2). In parallel to these Faradaic currents with electrochemical reactions we may have a certain e^- leakage current across the entire sample. However, the LA-ICP-MS

measurements clearly showed existence of substantial Faradaic processes which do not stop due to the limited O^{2-} conduction in the reaction zone even after 5 µm thick layers of reaction products have formed.

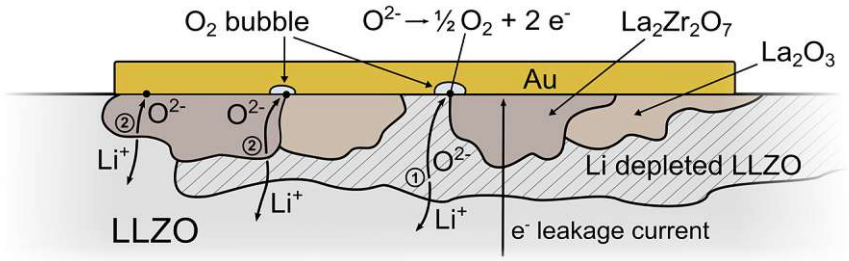

Figure 4.14: Schematic drawing of LLZO decomposition beneath a positively polarized Au electrode including potential reaction paths. $La_2Zr_2O_7$ and La_2O_3 are formed due to the oxidation of O^{2-}, which might be accompanied by the formation of LLZO with a sub-stoichiometric amount of O^{2-} and Li^+ ($Li_{7-2x}La_3Zr_2O_{12-x}$) as intermediate product. To ensure continuous depletion of Li, oxide ion conduction in LLZO (path 1) or in a decomposition product (path 2) is necessary. In addition to the electrochemical reactions, also a certain e^- leakage current across the entire sample might contribute to the total charge carrier transport.

In summary, these experiments clearly show that significant LLZO decomposition is induced at an applied voltage of 2 V, which corresponds to approx. 4.9 V vs. Li^+/Li according to the used estimation (see above). The reaction is on-going even after several days of polarization, meaning that the formed interfacial layers do not block further decomposition, at least under the given experimental conditions. The results therefore question the stability of LLZO against high voltage cathode materials. Moreover, the current-voltage curves in Figure 4.9 strongly suggest that the entire constant current regime between 1.4 V and 2.5 V is characterized by the same electrochemical process. This means that already above 1.2–1.4 V severe decomposition of LLZO takes place, which translates to a stability limit of 4.1–4.3 vs. Li^+/Li at this elevated temperature.

4.4.3 Polarization at room temperature

All experiments shown so far were performed at elevated temperatures, strongly enhancing the kinetics of the occurring processes. At room temperature, at which LIBs are usually operated, the investigated LLZO decomposition might be kinetically hindered and therefore less relevant for the application of LLZO. To investigate this, a single Au electrode on a Ga:LLZO single crystal was polarized for 14 days at room temperature.

The obtained current profile (Figure 4.15) shows the usual rapid decrease at the beginning of the experiment, which is followed by a current in the 0.01–0.1 nA range (approx. 0.1–1.2 µA cm^{-2} with respect to the microelectrode) for the rest of the polarization time.

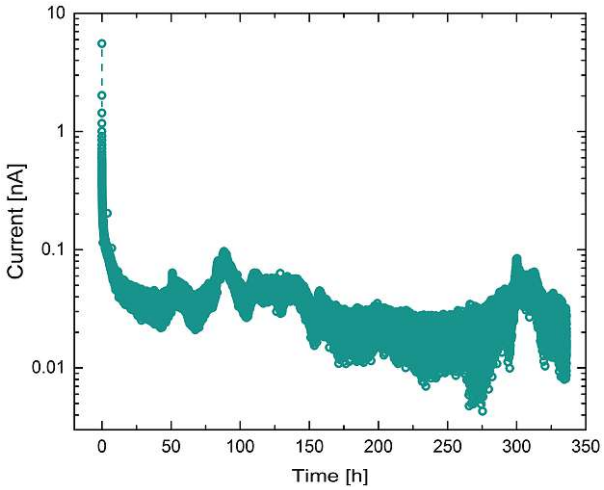

Figure 4.15: Current profile for a microelectrode constant voltage polarization experiment performed at room temperature (Ga:LLZO single crystal, 2 V voltage, 14 day polarization time, 100 µm electrode diameter). After a rapid decrease at the binning of the polarization, the current stays in the 0.01–0.1 nA range for most of the experiment. Significant current fluctuations are visible, indicating changes of the electrode/electrolyte interface caused by the polarization (e.g., O_2 formation leading to gas bubbles beneath the electrode).

Analogue to the experiments above, LA-ICP-MS was used to investigate potential Li-depletion beneath the polarize microelectrode. In Table 4.04, the results of this analysis are shown and compared to amount of charge carrier transport derived from the measured current. As expected, the effects induced by the polarization are significantly less pronounced at room temperature, especially considering the long polarization time. However, also at room temperature Li-depletion can be observed: for the sample layers directly beneath the electrode (i.e., the first ablation pass of the LA experiment), only 82% of the initial Li content was measured (not shown). This corresponds to a total amount of transported Li-ions of 0.130 nmol. Similar amounts were reached at 350 °C (set temperature) already after 30 min. However, the value is again in the same order of magnitude as the value derived from the measured current (see Table 4.04). The relatively good agreement once more shows that the results of the LA-ICP-MS analysis are reasonable. Overall, the experiment confirms that significant LLZO decomposition occurs even at room temperature, further questioning the long-term stability of LLZO with high voltage cathode materials.

Table 4.04: Total amount of transported Li-ions during electrode polarization at room temperature (2 V voltage, 14 days polarization time, 100 µm electrode diameter), determined via LA-ICP-MS as well as DC measurements. The Li-ion depletion observed via LA agrees reasonable with the currents measured during the electrode polarization.

	Total amount of transported Li^+
LA-ICP-MS	0.130 nmol
DC	0.423 nmol
Ratio	30.1 %

4.5 Conclusion

The electrochemical stability behavior of LLZO single crystals was investigated using field stress experiments in ambient air and subsequent electrochemical, chemical, and structural analysis. Different combinations of macro- and microscopic ionically blocking Au electrodes as well as various locally resolved analysis techniques including microelectrode EIS, LIBS, LA-ICP-MS, and microfocus XRD were used for the experiments. These experiments indicate that LLZO decomposes at 4.1–4.3 vs. Li^+/Li at elevated temperature (approx. 300°C). The decomposition leads to the deposition of Li_2CO_3 or other Li-containing salts (LiOH, Li_2O) at the cathodic side due to the reduction of O_2 from air in presence of CO_2 and H_2O. Beneath the anode (positively polarized), $La_2Zr_2O_7$ and La_2O_3 are formed due to the oxidation of O^{2-}, potentially accompanied by the formation of Li-depleted LLZO ($Li_{7-2x}La_3Zr_2O_{12-x}$) as intermediate product. Most likely not only Li^+ but also substantial O^{2-} conduction is involved in the decomposition process, which is on-going even several days after polarization and reaches several µm deep into the material (i.e., no blocking interfacial layer is formed). Interestingly, also at room temperature significant Li-depletion can be observed, questioning the long-term compatibility of LLZO with high voltage cathode materials.

5 Impact of H_2O exposure on $Li_7La_3Zr_2O_{12}$ garnets: Investigate Li^+/H^+ exchange using LIBS depth profiling

5.1 Introduction

With novel battery concepts such as aqueous Li-ion batteries and Li-air systems in mind, stability in humid/aqueous environment is a critical material property of solid electrolytes. While LLZO was initially believed to be chemically stable against moisture,[34] several studies report that LLZO undergoes Li^+/H^+ exchange (i.e., Li^+ in the garnet lattice gets replaced by H^+) in contact with humidity.[39,81,138] The process is accompanied by the formation of $LiOH.H_2O$ on the sample surface, which (partly) reacts to Li_2CO_3 when exposed to air.[95,139] A passivation layer is formed, which protects the material underneath from further degradation to some extent,[95] but is also known to negatively affect the interfacial properties with Li metal electrodes.[57,75,83] Since both LiOH and Li_2CO_3 are water-soluble, these secondary phases formed on the sample surface are removed in contact with water and thus do not (directly) hamper further Li^+/H^+ exchange in aqueous environment.[57]

Early studies show that water treatment promotes the transition from tetragonal LLZO to the cubic polymorph.[39] Cubic LLZO on the other hand seems to be stable even for high Li^+/H^+ exchange up to 75%.[126,140–142] Despite many studies focussing on site occupancy after Li^+/H^+ exchange, which Li sites are preferably vacated is still an unsettled matter.[126,137,141–143] In a recent work Redhammer et al.[137] conclude that the site occupation behaviour of Ta:LLZO, together with exchange rate, exchange capacity, and structural stability, strongly depend on the composition. More precisely, grain boundaries were shown to be more susceptible to moisture than grains.[73,81,82] This is also in agreement with reports of an increased grain boundary resistance after the immersion of LLZO in water.[73,144]

Li^+/H^+ exchange ranging from 29% to 75% has been reported for LLZO powders immersed in H_2O.[138] Although a rapid pH increase indicates high reaction rates within the first seconds,[126,142] the exchange has been shown to continue at reduced rate up to several days[145] or even weeks[137]. Interestingly, the Li^+/H^+ exchange is reversible to some extent by placing the protonated samples in strong basic Li^+ containing solutions.[126,142] Beside immersion time and water temperature, the rate and extent of Li^+/H^+ exchange depends on particle size: samples with high surface area exchange more quickly than samples consisting of large particles.[138] This is in agreement with experiments performed on LLZO pellets by Yow et al.[145], which show an Li^+/H^+ exchange of only 8.8 % even after one week of immersion. The authors conclude that

only a thin layer close to the surface experiences considerable H^+ incorporation and that ion diffusion inside the garnet is the rate-determining step of the ion exchange.[145]

Since Li^+/H^+ exchange only takes place at the surface, depth-resolved information is of major interest to gain insights in the kinetics of the process as well as to determine the true extent of the ion exchange. However, studies providing such information are scare. Brugge et al.[73] conducted SIMS depth-profiling experiments on Ga:LLZO pellets immersed in a H_2O bath at 100 °C for up to 30 min, revealing that the Li^+/H^+ exchanged region extends as far as 1.35 µm into the sample. The H^+ diffusion coefficient determined in this study is in reasonable agreement with results obtained by Hiebl et al.[141], who conducted an long-term XRD study on an Al:LLZO single crystal exposed to humid air.

Among the very few analytical techniques capable of direct H detection is LIBS, which was also has been shown to be a powerful tool for spatially resolved cation determination of (assumably H-free) LLZO.[74–76,97] In contrast to SIMS, which usually only provides semi-quantitative information, LIBS even enables quantitative analysis of H.[146–150] Furthermore, while being inferior to SIMS in terms of depth- and lateral resolution, LIBS is less limited when it comes to sampling depth (i.e., deeper sample layers can be reached) and the analysis of macroscopic areas (i.e., larger areas can be analyzed).

In this study, the Li^+/H^+ exchange behaviour of Ta:LLZO polycrystalline pellets as well as Ga:LLZO single crystals is investigated. For the purpose, the samples were immersed in an ultrapure water bath at 80 °C for 80 min. Subsequently, the chemical composition of the water as well as of the LLZO samples is analysed via ICP-OES and LIBS depth profiling, respectively. The experiments reveal a strongly enhanced Li^+/H^+ exchange for Ta:LLZO pellets compared to Ga:LLZO single crystals.

5.2 Experimental

5.2.1 H_2O exposure

All experiments presented in this chapter were conducted on two kinds of cubic LLZO samples:

- Ta:LLZO polycrystals with a nominal composition of $Li_{6.4}La_3Zr_{1.4}Ta_{0.6}O_{12}$ purchased from Toshima Manufacturing Co., Ltd. (Japan).

- Ga:LLZO single crystals with a composition of $Li_{6.43}Ga_{0.14}La_{2.84}Zr_2O_{11.68}$ (normalized to 2 Zr pfu) synthesized by Dr. Steffen Ganschow at the Leibniz-Institut für Kristallzüchtung (Berlin, Germany) using the procedure described in Section 4.2.1.

In order to ensure a well-defined sample surface as well as to remove potential surface contaminations such as Li_2CO_3[75], all samples were polished using SiC grinding paper (P4000). The samples were stored under Ar atmosphere between all experiments to minimize contact to air, which was kept below 2 min for all samples and thus should not affect the results of this study.

To investigate Li^+/H^+ exchange caused by exposure to H_2O, LLZO samples were immersed in ultrapure water (18.2 MΩ cm^{-1} at room temperature) heated to about 80 °C in polyethylene testing tubes. The ultrapure water was obtained by a Barnstead™ Easypure ™ II (Thermo Fisher Scientific, USA). Individual samples were immersed in about 5 ml H_2O for a total duration of 80 min. The deionized water was replaced three times (after 5 min, 30 min, and 55 min) during the experiment. After the immersion, the samples were quenched by dipping them into H_2O cooled down to 5 °C.

To ensure that the released cations are stabilized in the aqueous solutions (i.e., to prevent adsorption at the testing tube walls), a 1/100 (v/v) mixture of hydrofluoric acid (40 m%, Emsure®, Merck, Germany) and nitric acid (65 m%, Emsure®, Merck, Germany) was added to all water fractions after the Li^+/H^+ exchange experiment, resulting in final nitric acid concentration of 0.65 m%. All samples were stored at 5 °C until chemical analysis as well as between all further measurements.

5.2.2 ICP-OES measurements

To investigate the release of cations, all water fractions used for sample immersion were analysed using ICP-OES. For the measurements, an iCAP 6500 RAD (Thermo Fisher Scientific, USA) was used. More information to the used instrumental setup can be found in Section 2.2.3. Detailed information about the used instrument parameters is given in Table 5.01.

Signal quantification was performed via univariate calibration using certified single element ICP-standard solutions (Certipur®, Merck, Germany). Calibration standards containing Ga, La, Li, Ta, and Zr in concentration ranging from 1 to 1000 µg kg^{-1} were prepared by mixing the corresponding single element standards and diluting the obtained stock solution using a 1/100

(v/v) dilution of nitric acid (0.65 m%). An Eu ICP-standard solution (Certipur®, Merck, Germany) was added to all standard and sample solutions to a final concentration of 200 µg kg^{-1} and acted as internal standard for the analysis.

Table 5.01: Instrumental setting ICP-OES analysis

	Thermo iCAP 6500 RAD	
RF power	1200 W	
Radial observation height	12 mm	
Plasma gas flow (Ar)	12 l min^{-1}	
Nebulizer gas flow (Ar)	0.6 l min^{-1}	
Auxiliary gas flow (Ar)	0.8 l min^{-1}	
Integration time	5 s	
Replicates per sample	5	
Purge pump rate	1.6 ml min^{-1}	
Sample flow rate	0.8 ml min^{-1}	
Analytical wavelengths		
Eu (Internal standard)	381.967 nm	
Ga	294.364 nm	417.206 nm*
La	333.749 nm	412.323 nm*
Li	610.362 nm	670.784 nm*
Ta	240.063 nm	268.517 nm*
Zr	339.198 nm	343.823 nm*

* used for quantification

5.2.3 LIBS measurements

Changes in the H as well as Li content within the LLZO samples were probed using LIBS. Measurements were conducted using a commercially available J200 LIBS system (Applied Spectra Inc., USA) equipped with a 266 nm frequency quadrupled Nd:YAG laser and a six-channel Czerny-Turner type spectrometer covering a wavelength range from 188 to 1048 nm. For data collection, Axiom 2.0 software provided by the manufacturer of the instrument was used. Detailed information about the instrumental parameters used for the analysis is shown in Table 5.02.

Table 5.02: Instrumental setting LIBS analysis

LIBS instrumentation	J200
Pulse duration	5 ns
Output energy	2.3 mJ
Beam diameter	60 µm
Scan speed	0.12 mm s^{-1}
Repetition rate	10 Hz
Beam geometry	circular
Gate delay	0.1 µs
Gate width	1.05 ms
Atmosphere	He
Gas flow	2 l min^{-1}

In addition to samples exposed to H_2O, also samples not treated with hot deionized water were measured and served as reference for the analysis. To check the influence of potential H_2O residues (e.g., in the sample pores), all samples including the reference ones were dipped (again) into 5 °C cold distilled water directly before transfer to the sample chamber, thus ensuring equal measurement conditions (i.e., H signal from excess H_2O is also visible in reference spectra). Before the start of the measurement, the samples were dried inside the sample chamber under He atmosphere (constant gas flow of 2 l min^{-1}) for 2 h at room temperature.

For signal quantification, matrix-matched standards with variable H content (ranging from 0.00 m% to 0.64 m% nominally) were prepared by pressing different mixtures of calcinated Al:LLZO precursors and $La(OH)_3$ (99.9%, Sigma-Aldrich, USA) powder into pellets. The used Al:LLZO precursor powder (nominal composition $Li_{7.04}Al_{0.2}La_3Zr_2O_{12}$ including excess of Li precursor) was synthesized by Dr. Reinhard Wagner at the department of Chemistry and Physics of Materials at the Paris Lodron University of Salzburg (Salzburg, Austria) using the procedure described in Section 2.2.1. For each standard, a total amount of about 1 g powder mixture was homogenized using an agate mortar, transferred into a flexible silicone rubber mould, and cold pressed using a mechanical isostatic press (Paul-Otto Weber, Germany) at a pressure of 300 MPa. The surface of the obtained pellets was mechanically cleaned using SiC grinding paper (P2000) to remove potential contaminations from the pressing mould. In addition to in-house prepared pressed pellets, a pristine Ga:LLZO single crystal, which was assumed to be hydrogen free, was used as calibration standard. All standards were polished using SiC grinding paper (P4000) directly before transfer into the sample chamber of the LIBS instrument.

Ablation patterns consisting of one line scan with a length of 1.2 mm were used for all measurements. By ablating such a pattern, 101 individual spectra are obtained, which were accumulated for further data processing. The integrated signals of the atomic emission lines H 656.3 nm (H-alpha), La 654.3 nm, and Li 610.4 nm were evaluated. For line integration, the software OriginPro 2016 (OriginLab Corporation, USA) was used. Signal normalization was performed using the integrated La signal, whereas differences in the La content were considered and corrected accordingly.

Calibration of the LIBS analysis was conducted using five ablation patterns on each calibration standard (single ablation). Since contact with air could not be avoided during preparation of the standards, potential H_2O adsorption and/or H^+ incorporation in the used LLZO powder has to be considered and the absolute H content of the pressed pellets is thus not directly known. To enable absolute signal quantification, the amount of additional H (i.e., the H content of the used LLZO powder) was determined via standard addition approach using additional H signal introduced by the added $La(OH)_3$. To determine the H background originating from the instrument and correct the analysis accordingly, the signal of the pristine (H-free) Ga:LLZO single crystal calibration standard was used.

Depth profiling experiments were conducted by ablating the same area (represented by laser pattern) 15 times in a row. Per sample one depth profiling measurement was performed. After the experiments, the sampling depths were determined using a DektakXT profilometer (Bruker, USA). A constant ablation rate was assumed to calculate how much material was removed with each individual layer.

5.2.4 EIS

The ionic conductivity of the LLZO samples was measured by EIS before and after the Li^+/H^+ exchange experiment. As electrodes, 200 nm thick Au layers were deposited on the top and bottom side of the samples using a MED 020 coating system (Bal-Tec AG, Liechtenstein). For the measurements, which were performed at room temperature (25 °C), an Alpha-A high performance frequency analyzer (Novocontrol Technologies, Germany) in the frequency range from 10 Hz or 1 kHz to 10 MHz was used.

5.3 Results and discussion

5.3.1 H_2O analysis via ICP-OES

To investigate moisture-induced chemical degradation and Li^+/H^+ exchange of LLZO, a Ga:LLZO single crystal as well as a Ta:LLZO polycrystalline pellet were immersed in a H_2O bath at 80 °C for 80 min. After the experiment, the concentration of Ga, La, Li, Ta, and Zr in the used H_2O were determined via ICP-OES, giving access to the amounts of cations released from the samples during the exposure.

Table 5.03: Amounts of cations released into the H_2O used for sample exposure determined via ICP-OES, including LOD (= $\bar{x}_{blank} + 3 \times s_{blank}$; n = 8) and LOQ (= $\bar{x}_{blank} + 6 \times s_{blank}$, n = 8) of the analysis. The stated measurement uncertainties correspond to the confidence intervals of the mean values derived from replicate measurements (α = 0.05, n = 3). Relatively large amounts of Li were released, confirming Li^+/H^+ exchange during the experiment.

Ga:LLZO single crystal

	LOD [µg]	LOQ [µg]	Analyte mass [µg] 0-5 min	5-30 min	30-55 min	55-80 min	total	Analyte released from sample [%]
Ga	0.12	0.25	< LOD	< LOD	< LOD	< LOD	-	-
La	0.07	0.11	< LOD	< LOD	< LOD	0.127 ± 0.017	0.127 ± 0.017	0.00118 ± 0.00016
Li	0.05	0.09	1.667 ± 0.006	1.349 ± 0.008	0.787 ± 0.014	0.570 ± 0.008	4.372 ± 0.019	0.3591 ± 0.0019
Ta	0.11	0.29	-	-	-	-	-	-
Zr	0.03	0.06	0.092 ± 0.007	< LOQ	< LOD	< LOQ	0.092 ± 0.007	0.00185 ± 0.00014

Ta:LLZO polycrystalline pellet

	LOD [µg]	LOQ [µg]	Analyte mass [µg] 0-5 min	5-30 min	30-55 min	55-80 min	total	Analyte released from sample [%]*
Ga	0.12	0.25	-	-	-	-	-	-
La	0.07	0.11	0.598 ± 0.006	0.503 ± 0.009	< LOQ	0.252 ± 0.009	1.353 ± 0.014	0.00157 ± 0.00002
Li	0.05	0.09	22.83 ± 0.05	41.39 ± 0.26	28.87 ± 0.06	19.59 ± 0.04	112.7 ± 0.27	1.226 ± 0.003
Ta	0.11	0.29	< LOD	< LOD	< LOD	< LOD	-	-
Zr	0.03	0.06	0.177 ± 0.006	0.140 ± 0.014	< LOD	< LOQ	0.316 ± 0.015	0.00119 ± 0.00008

*using the nominal sample composition as reference

The results of the ICP-OES analysis are summarized in Table 5.03. Relatively large amounts of Li^+ were released during the immersion, for both the Ga:LLZO single crystal as well as the Ta:LLZO polycrystalline pellet (approx. 4.4 and 113 µg, respectively). Also La and Zr could be detected in the solutions, however, compared to Li the measured amounts are very small and thus negligible (difference is at least a factor of 30). Since LLZO dissolution can therefore be excluded as reason for the increased Li concentrations, the ICP-OES analysis confirms that significant Li^+/H^+ exchange took place during the H_2O exposure.

During the immersion experiment, the water bath was replaced with fresh deionized water three times (after 5 min, 30 min, and 55 min) and all fractions were analyzed individually. Under the assumption that replacing the water does not significantly change the kinetics of the ion exchange, this gives access to rough time-resolved information about the occurring reaction. It can be observed that also during the last segment of the experiment a significant amount of Li^+ was released, indicating an on-going Li^+/H^+ exchange even after 55 min. This is in agreement with Yow et al.[145], who shows that the ion exchange continues (at a reduced rate) up to one week when LLZO sample are immersed in water.

This continuous ion exchange is also visible in Figure 5.01, where the total amount of released Li^+ is plotted against the exposure time. In this plot, all values are normalized to the corresponding sample surface area (counting all sides), enabling a meaningful comparison of the two samples. It can be observed that significantly more Li^+ was released from the Ta:LLZO polycrystalline pellet. At the end of the experiment, the difference to the Ga:LLZO single crystal is more than a factor of 7.5, indicating a strongly enhanced Li^+/H^+ exchange for the polycrystalline pellet.

If we treat the used samples as initially homogeneous semi-infinite media whose surface is maintained at a Li^+ concentration of zero (i.e., 100% Li^+/H^+ exchange at the sample surface layer), the total amount $M_t^{Li^+}$ of diffusing Li^+ leaving the LLZO during the experiment can be mathematically described by Equation 5.01[151]:

$$M_t^{Li^+} = 2c_0^{Li^+}\sqrt{\frac{Dt}{\pi}}\ [g\ m^{-2}] \qquad (5.01)$$

Here, $c_0^{Li^+}$ is the initial Li^+ concentration throughout [g m^{-3}], which can easily be derived from the sample stoichiometry and the volume of a cubic LLZO unit cell (2.188×10^{-27} m^3 [41]), D the diffusion coefficient [m^2 s^{-1}], and t the exposure time [s]. With LLZO being a fast Li-ion conductor, the Li^+/H^+ exchange is limited by the diffusion of H^+ within the material, and D thus

describes the H^+ (and not the Li^+) diffusivity. It is also important to mention that the condition of a zero surface concentration is not entirely accurate for the exchange experiment since Li^+ accumulates in the surrounding water. However, since the Li^+ concentration stays very low, the resulting error should be minor.

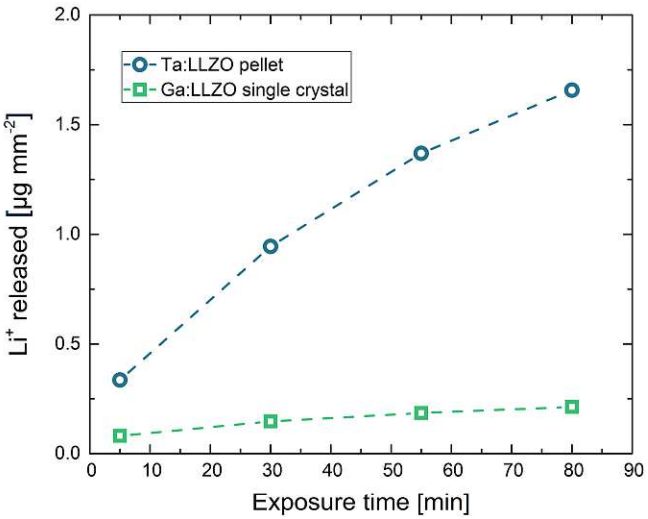

Figure 5.01: Amount of Li^+ released during the Li^+/H^+ exchange experiment, normalized to the total sample surface. Confidence intervals of the measurement ($\alpha = 0.05$, $n = 3$) were calculated, but are too small to be visible in the plot. Significantly higher Li^+ release for the Ta:LLZO polycrystalline pellet can be observed.

According to Equation 5.01, the total amount of released Li^+ shown in Figure 5.01, which is normalized to the total sample surface and thus corresponds to $M_t^{Li^+}$, should be directly proportional to the square root of the exposure time. To better visualize the exact relation for the LLZO samples, the corresponding plots are shown in Figure 5.02. For the Ga:LLZO single crystal (Figure 5.02a), indeed a distinct linear correlation between the released Li^+ and the square root of the exposure time can be observed, confirming the diffusion driven Li^+ release described by the model. However, the plot shows a significantly positive intercept, indicating that another process is involved in the first segment of the experiment. Possibly, Li^+ containing secondary phases (LiOH and/or Li_2CO_3), formed on the sample surface before the experiment due to contact with air, acted as additional Li^+ source, despite cleaning the crystal surface by polishing directly before the analysis and minimizing contact with air (see Experimental). Since both LiOH and Li_2CO_3 are highly soluble, only the first water fraction is affected by their dissolution (showing an increased Li^+ content). Accordingly, the rest of the experiment (i.e., the remaining water fraction) is only affected by Li^+/H^+ exchange and therefore purely driven by ion diffusion. Since the Li^+ release follows Equation 5.01 between minute 5 and 80, the slope of the linear fit can be used to calculate the diffusion coefficient of the material. The calculation

yields in a LLZO bulk diffusion coefficient D_{bulk} of 6.9×10^{-17} m^2 s^{-1} at 80 °C, which is in good agreement with the H^+ diffusivities determined by Brugge et al.[73] (order of 10^{-16} m^2 s^{-1} at 100 °C) and Hiebl et al.[141] (approx. 2×10^{-17} m^2 s^{-1} at room temperature).

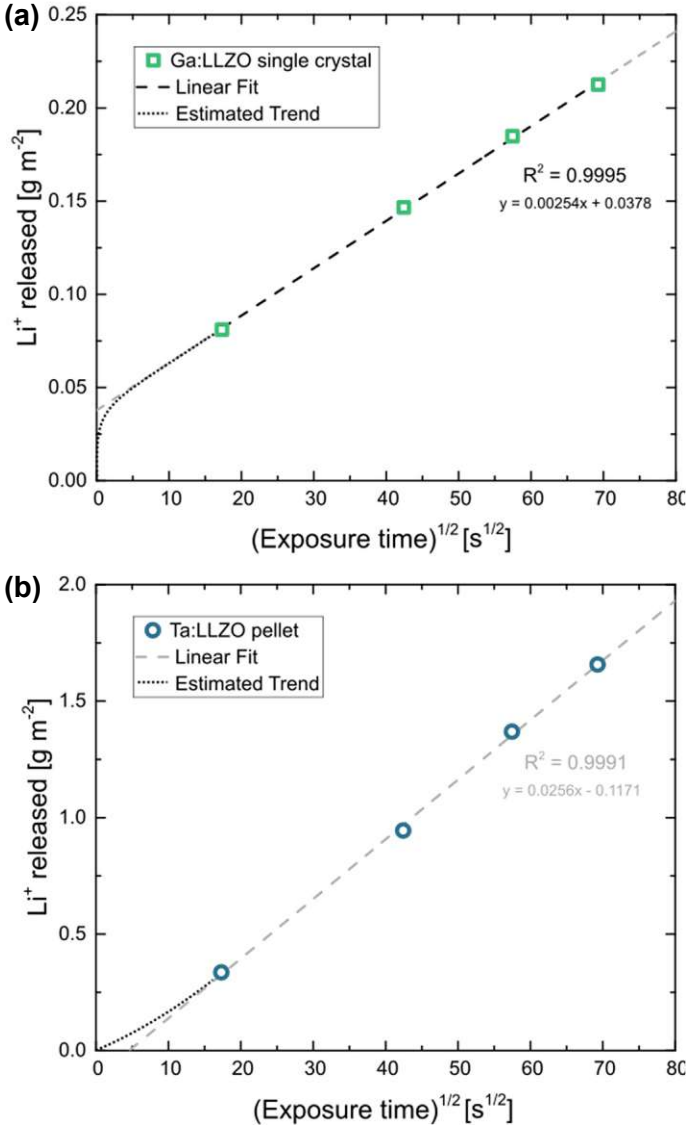

Figure 5.02: Released Li^+ vs. square root of the exposure time for (a) the Ga:LLZO single crystal and (b) the Ta:LLZO polycrystalline pellet. In case of the single crystal, the slope of the linear fit can be used to calculate the (hydrogen) bulk diffusion coefficient of LLZO.

At first glance also for the Ta:LLZO polycrystalline pellet a linear correlation between the released Li^+ and the square root of the exposure time can be observed (Figure 5.02b). Similar to the single crystal, the linear fit yields in an intercept differing significantly from zero, but in this case the offset is negative. The total amounts of exchanged Li^+ are much higher than for the single crystal, which could explain that the positive y-axis intercept due to supposed soluble

Li-containing phases is no longer visible. However, the negative offset can only be explained by a reduced ion diffusion rate at the beginning of the experiment, strongly indicating that the Li^+/H^+ exchange does not follow Equation 5.01. Accordingly, another (more complex) diffusion process seems to be decisive for polycrystalline LLZO, and it is thus not possible to calculate the diffusion coefficient like above. Experiments shown later in this chapter indicate a strongly enhanced H^+ diffusion along the grain boundaries of LLZO, which explains the different diffusion behavior of the Ta:LLZO polycrystalline pellet as well as its significantly increased Li^+ release compared to the Ga:LLZO single crystal.

5.3.2 LLZO analysis via LIBS

H^+ uptake of the LLZO samples during the H_2O exposure as well as its effect on the corresponding Li contents were analyzed using LIBS. Since concentration gradients are generated during the occurring Li^+/H^+ exchange, depth-resolved information is necessary for a meaningful chemical analysis. Accordingly, LIBS depth profiling experiments were conducted.

LIBS calibration

To enable signal quantification, in-house prepared matrix-matched calibration standards with variable H content were used. To obtain such standards, calcinated Al:LLZO precursors were mixed with $La(OH)_3$, acting as hydrogen source, and pressed into pellets. Additionally, a pristine and thus presumably hydrogen free Ga:LLZO single crystal was used as blank standard for background determination.

The obtained calibration curves are shown in Figure 5.03. Distinct linear correlations were achieved for the H signal (Figure 5.03a+b, $R^2 = 0.987$) as well as the Li signal (Figure 5.03c, $R^2 = 0.970$). In Figure 5.03a the nominal H content of the prepared matrix-matched standard is plotted on the x-axis. Since calcinated LLZO powder was used for the standard preparation and contact with air could not be avoided during the procedure, H_2O adsorption and/or H^+ incorporation are to be expected, affecting the actual H contents of the standards. This is confirmed by the measurement, which shows a significantly enhanced H signal. To compensate this phenomenon, the excess H was determined using the slope of the calibration curve (i.e., via standard addition method), resulting in a H content of 0.47 m% ± 0.08 m% (95% confidence interval) for the nominally H-free standard. The H contents of the standards were corrected accordingly (Figure 5.03b), enabling reliable quantification of the H signal.

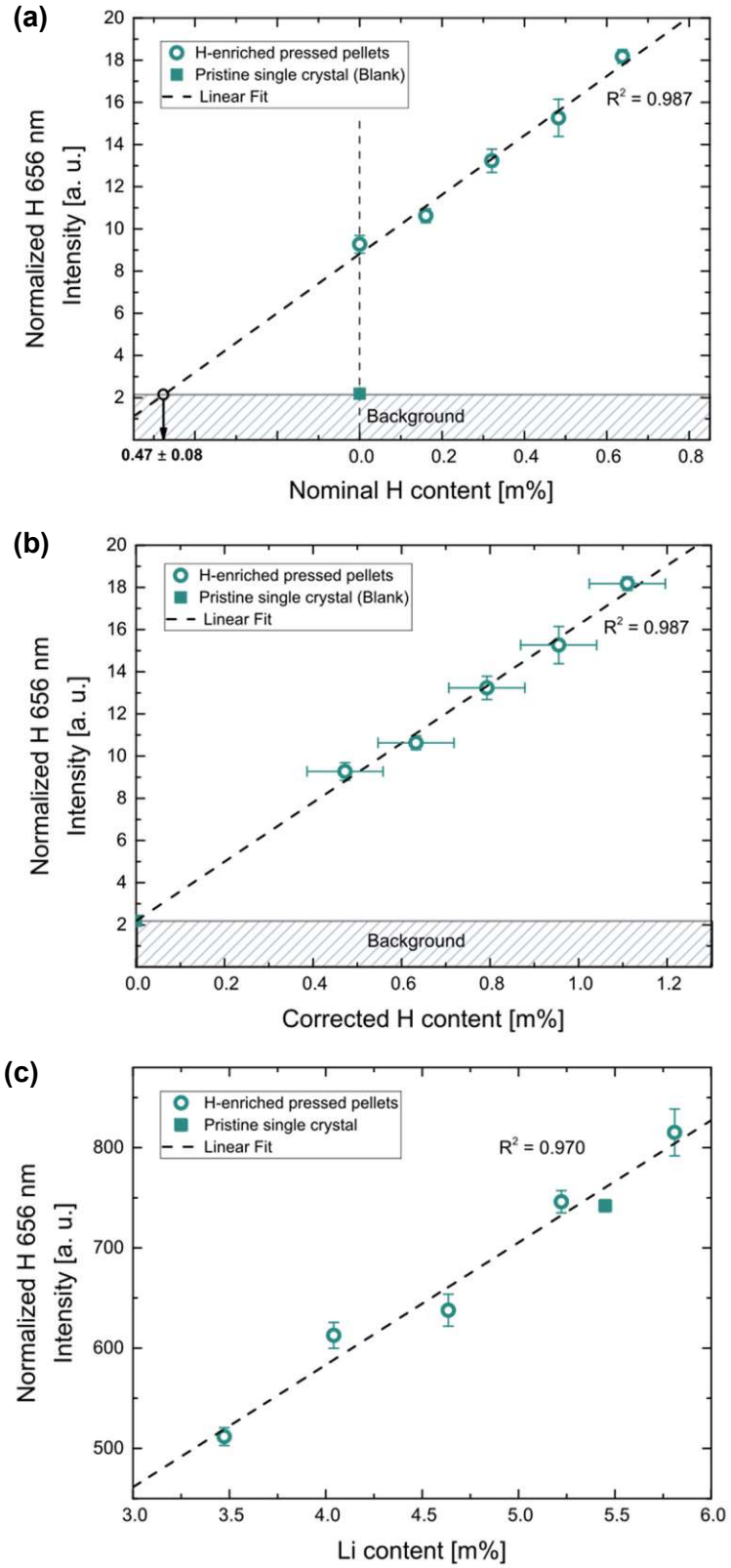

Figure 5.03: LIBS calibrations of the H signal, using nominal (a) and corrected (b) H content of the prepared matrix-matched standards, as well as corresponding calibration of the Li signal (c). The vertical error bars represent the confidence intervals of the mean values derived from the measurement of multiple ablation patterns (α = 0.05, n = 5); the horizontal error bars in (b) represent the confidence intervals of the correction of the H content (α = 0.05). Suitable signal quantification for H as well as Li could be achieved.

Depth profiling

LIBS depth profiling experiments were conducted on the samples exposed to H_2O as well as corresponding reference samples. Quantitative concentration values were derived from the recorded signal using the calibrations shown above, leading to the depth profiles displayed in Figure 5.04. The measurements confirm an enhanced Li^+/H^+ exchange for the polycrystalline pellet, as already shown by the ICP-OES analysis (cf. Section 5.3.1), with H^+ incorporation much deeper into the material.

Figure 5.04a and Figure 5.04b show the H depth profiles for the Ga:LLZO single crystal as well as the Ta:LLZO polycrystalline pellet, respectively. In addition to the absolute H content, the corresponding percentage of Li^+/H^+ exchange is shown on the secondary y-axis. On this scale, 100% indicates that all Li^+ within the material was replaced with H^+. Since in case of the Ta:LLZO pellet only the nominal sample composition is known, the average Li content of the reference sample was used as reference for the calculation.

In case of the Ga:LLZO single crystal, only for the first layer (0.0–1.4 µm) a significantly increased H content can be observed. This is in agreement with the hydrogen diffusivity determined from the measured amount of released Li^+ (see Section 5.3.1): using the relationship

$$l_D = \sqrt{2Dt}\ [m] \qquad (5.02)$$

the (hydrogen) bulk diffusion length l_D is 0.8 µm. Interestingly, no significant difference to the reference sample can be observed, which also shows an increased H content for the first layer. It is important to point out that since not only the sample itself but also the sample surface is probed at the first ablation layer of the LIBS measurement, H-rich species such as LiOH as well as H_2O residues at the sample surface would lead to increased H content and therefore an overestimation of the H^+ incorporation. However, the Li depth profile of the sample (Figure 5.04c) shows a decreased Li content for the first layer, which confirms that the increased H signal is caused by Li^+/H^+ exchange and not by such H-rich surface species. Since all samples including the reference ones were dipped into cold (ultrapure) water directly before the analysis (to ensure equal measurement conditions, see Experimental) and then dried inside the sample chamber under inert atmosphere, it is not surprising that the influence of H-rich surface species was minimized. Since significant H^+ uptake can be observed, apparently either significant ion exchange occurred during the short air exposure and/or contact with water, or the cleaning of the sample surfaces via polishing before the experiments was incomplete and residues of old surface layers were probed. This is in agreement with the results of the H_2O analysis via ICP-OES, indicating that LiOH and/or Li_2CO_3 was formed on the surface of the

Ga:LLZO single crystal before the actual experiment (cf. Section 5.3.1), which must be accompanied by an Li^+/H^+ exchange reaction. However, when probing Li a difference between reference and exposed sample is found, indicating a contribution due to true Li^+/H^+ exchange during the H_2O exposure at 80 °C.

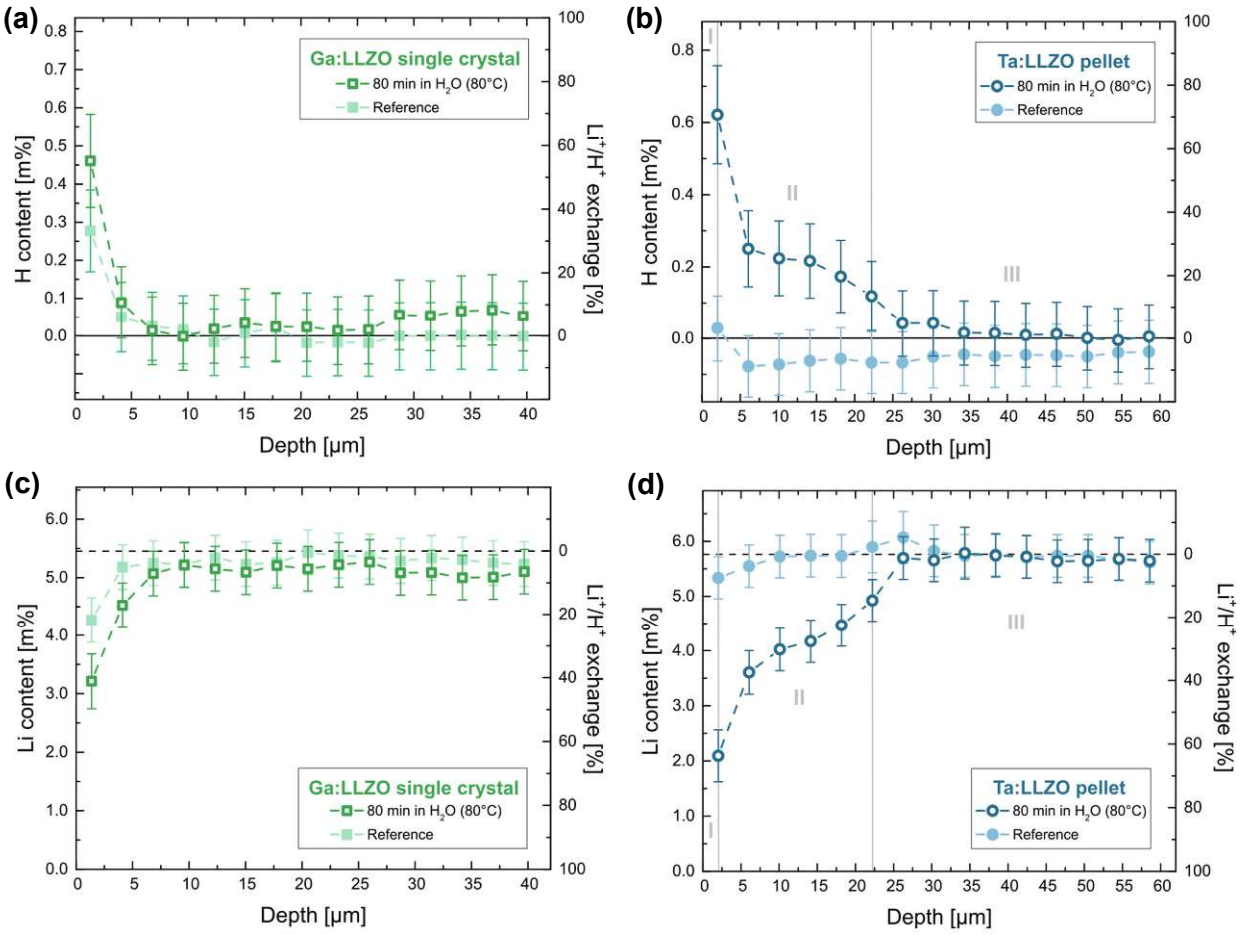

Figure 5.04: H (a+b) and Li (c+d) depth profiles obtained by LIBS analysis of LLZO samples exposed to H_2O as well as correspond reference samples. Error bars represent the confidence intervals of measurements (α = 0.05). While for the Ta:LLZO polycrystalline pellet (b+d) up to a sampling depth of 22.2 µm significant Li^+/H^+ exchange can be observed, effects are much less pronounced and limited to the near surface region in case of the Ga:LLZO single crystal (a+c).

For the H depth profile of the Ta:LLZO polycrystalline pellet (Figure 5.04b), strong differences between immersed sample and reference can be seen. The depth profile can be divided into three zones:

- Zone I (0.0–2.0 µm): Strong H^+ incorporation (~70% Li^+/H^+ exchange)
- Zone II (2.0–22.2 µm): Significant H^+ incorporation (5–40 % Li^+/H^+ exchange)
- Zone III (>22.2 µm): No significant H^+ incorporation

Zone I corresponds to the first layer of the LIBS measurement, meaning that also the sample surface might affect the analysis. However, these surface effects should be also visible for the reference sample, which does not show a significant H signal. It thus can be assumed that the sample surface did not significantly affect the analysis and the measured H signal solely originates from Li^+/H^+ exchange. Accordingly, the analysis shows that in the first 2 µm of the sample the majority of Li^+ was replaced by H^+. Even more interestingly, the zone in which significant H^+ incorporation can be observed (zone II), reaches 22.2 µm deep into the material. This is by far the highest H^+ penetration depth after immersion in H_2O reported in literature. As comparison, Brugge et al.[73] found that the protonated region extends as far as 1.35 µm into a Ga:LLZO pellet after exposure at comparable conditions (100 °C, 30 min).

The Li depth profile of the Ta:LLZO pellet (Figure 5.04d) confirms these findings. In agreement with theoretical considerations, the Li content is negatively correlated to the H content (i.e., a high H content leads to a low Li content). The Li^+/H^+ exchange rates calculated from the determined Li contents (approx. 60% and 45–10% for zone I and II, respectively) agree with the ones derived from the H profile, further confirming the results of the analysis. Compared to the Ga:LLZO single crystal, where the degradation effects of the H_2O exposure are only moderate and limited to the first few µm of the sample (cf. Figure 5.04c), the Li profile once more confirms that the degradation effects are much more pronounced for the Ta:LLZO polycrystalline pellet, reaching more than 20 µm deep into the sample.

To put the LIBS measurements in perspective to the H_2O analysis via ICP-OES, the total amount of Li^+ released from the Ta:LLZO pellet was calculated from the corresponding Li profile under the assumption of a uniform Li^+/H^+ exchange over the whole sample surface. According to this calculation, 1.39 % ± 0.20 % (95% confidence interval) of all Li^+ within the material was released, which is in excellent agreement with the value derived from the ICP-OES analysis (cf. Table 5.03). This once more indicates that the results of the LIBS analysis are accurate and thus confirms the findings of this study.

Since the Ta:LLZO polycrystalline pellet is evidently more prone to enhanced Li^+/H^+ exchange than the Ga:LLZO single crystal, two possible reasons for the different behavior can be identified:

- Stabilization element (Ta vs. Ga)
- Crystallinity (polycrystalline pellet vs. single crystal)

According to the ICP-OES analysis of the different water fractions, both samples show fundamentally different diffusion behavior (cf. Figure 5.02), indicating that the grain

boundaries are the more likely reason for the enhanced ion exchange. Multiple studies have shown that grain boundaries are more reactive with H_2O than grains,[73,81,82] further supporting the hypothesis of an increased H^+ incorporation at the grain boundaries. At first glance, this is in contradiction to the depth-resolved SIMS study by Brugge et al.[73], in which a significantly smaller H^+ penetration depth is reported for Ga:LLZO polycrystalline pellets. However, in this experiment the probed sample area was selected in a way that only individual grains are probed, avoiding that grain boundaries contribute to recorded signal. In the very same study, it is shown via EIS measurements that grain boundary resistance increases by several orders of magnitude after immersion in H_2O, also indicating a deeper degradation of grain boundaries compared to grains.[73] It thus seems to be a reasonable conclusion, that H diffusion is enhanced along the grain boundaries, enabling H^+ incorporation much deeper into the material. From the (H-enriched) grain boundaries, H^+ can then diffuse into the grains, ultimately leading to significantly more pronounced Li^+/H^+ exchange for polycrystalline LLZO samples.

Assuming a bulk diffusion length being smaller than the grain size, this is described be the so-called Harrison type B regime[152,153] (Figure 5.05). Such a situation leads to a depth profile with a steep zone close to the surface (related to bulk diffusion) and a shallower part which reflects grain boundary diffusion (cf. model of Whipple and Le Claire[154,155]). This is exactly what we see in the measured profiles of the Ta:LLZO polycrystalline pellet (cf. Figure 5.04b+d), and further supports the assumption of fast grain boundary diffusion.

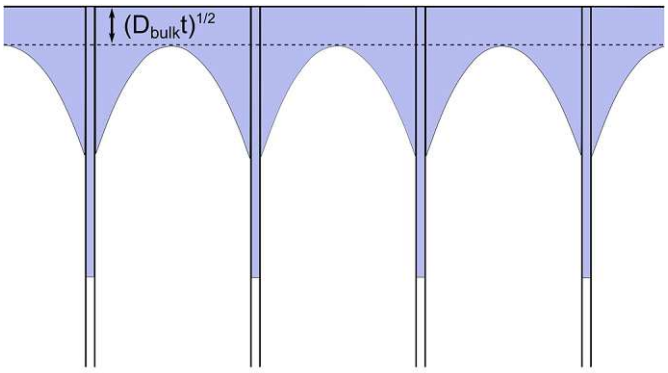

Figure 5.05: Schematic illustration of a type B diffusion kinetics according to Harrison's[152] classification.

5.3.3 Impact on the conductivity behavior

To monitor the conductivity behavior of the LLZO samples, room temperature EIS measurements were performed before and after the H_2O exposure. In Figure 5.06, impedance

spectra of the pristine (freshly polished) samples are compared with the spectra obtained after the Li^+/H^+ exchange experiment (80 min in H_2O at 80 °C), including measurements of the reference samples (dipped into 5 °C cold H_2O before the LIBS analysis, stored in Ar atmosphere between the experiments). For both the Ga:LLZO single crystal as well as the Ta:LLZO polycrystalline pellet, a significant impact of the H_2O exposure can be observed, however, only in case of the Ta:LLZO pellet a large difference to the reference sample is visible.

The impedance spectra of both pristine LLZO samples (Figure 5.06a) show part of a slightly depressed semicircle at high frequencies, which can be attributed to the ion conduction of the bulk in agreement with earlier studies.[54,117] In case of the Ta:LLZO polycrystal, a second semicircle-like feature is visible at the intermediate frequencies, which is most likely the grain boundary contribution. Following the grain (and grain boundary) feature(s), a well separated low frequency contribution representing the impedance of the ionically blocking Au electrodes.

Bulk resistance R_b and grain boundary resistance R_{gb} could be obtained by fitting the experimental data with the equivalent circuit shown in Figure 5.06a. From the total resistance R_{total} (= R_b + R_{gb}, whereas R_{gb} = 0 in case of the Ga:LLZO single crystal), the effective ion conductivity σ_{ion} was calculated via Equation 3.01. For the Ga:LLZO single crystal and the Ta:LLZO polycrystalline pellet, a total ionic conductivity at room temperature of 7.8×10^{-4} S cm^{-1} and 5.5×10^{-4} S cm^{-1} was obtained, respectively. These are typical values for cubic LLZO.[26,48]

In Figure 5.06b+c and Figure 5.06d–f, the impedance spectra of the Ga:LLZO single crystal and the Ta:LLZO polycrystalline pellet after the Li^+/H^+ exchange experiment are shown, respectively. To enable a meaningful comparison with the corresponding pristine samples, the spectra are shown multiple times on different scale. Since the individual features are poorly separated, no quantitative information can be extracted from the data, however, the spectra still provide valuable (qualitative) insights. For both the single crystal and the pellet, the bulk contribution is still visible (see Figure 5.06b and 5.06d, respectively), and no significant change in the bulk conductivity is apparent. In contrast to the pristine samples, the individual features are not clearly separated, indicating a new contribution at intermediate frequencies which is overlapping with the other features and thus distorts the spectra. A possible explanation for this phenomenon is the formation of a thin interfacial layer on the sample surface due to the contact with water. Apparently, already short H_2O exposure is enough to cause this contribution since it is also visible in the reference spectra. In addition to the poor feature separation, the contact with H_2O caused a strongly enhanced electrode impedance at low frequencies (see Figure 5.06c+e+f).

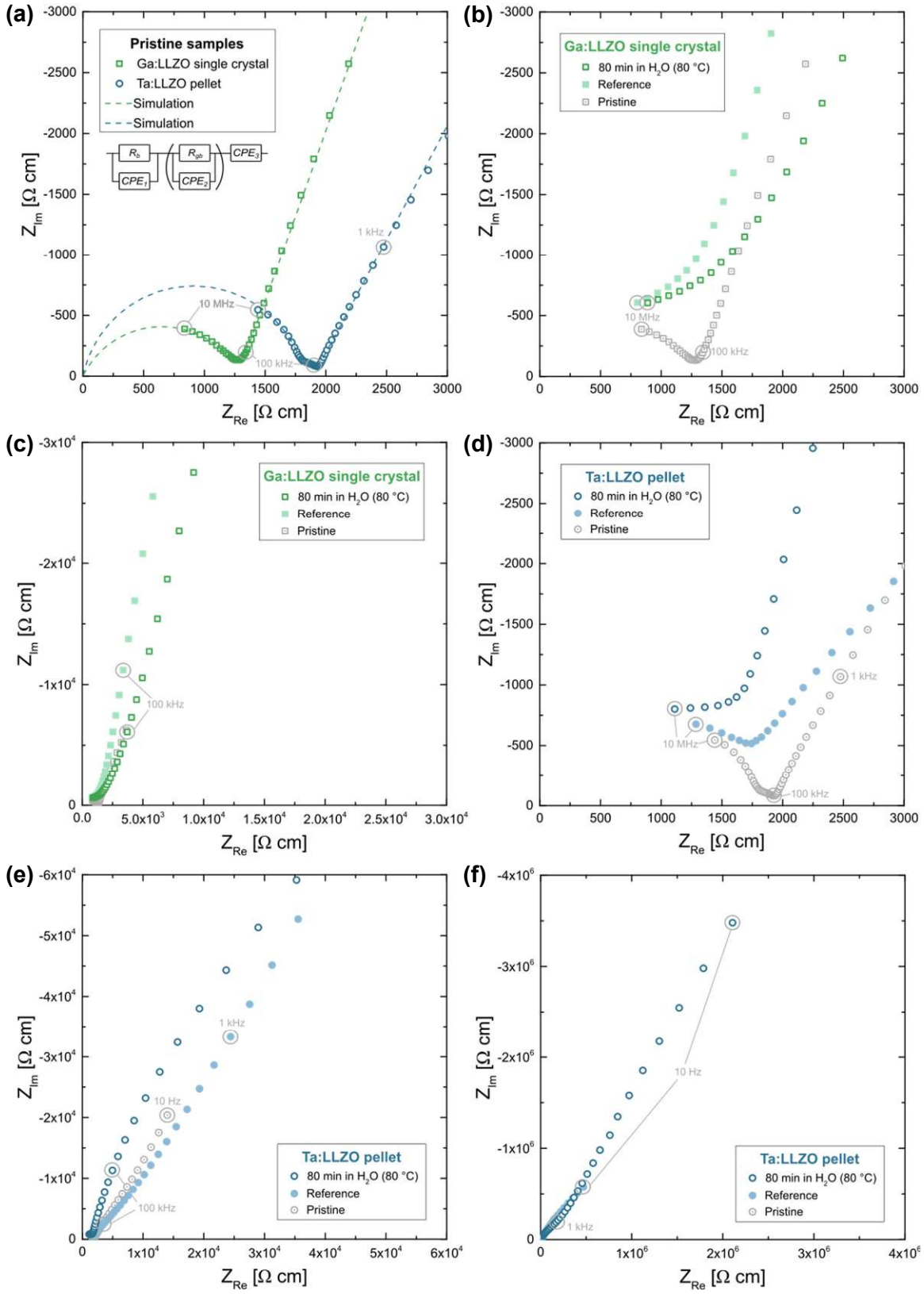

Figure 5.06: Geometry-normalized impedance spectra of the LLZO samples recorded at 25 °C. Spectra of pristine samples including simulations (a) as well as their comparison with corresponding measurements after H_2O exposure for the Ga:LLZO single crystal (b+c) and the Ta:LLZO polycrystalline pellet (d–f). The same spectra are plotted multiple times on different scale to enable a better comparison. A strong impact of H_2O exposure can be observed, especially for the Ta:LLZO pellet.

Interestingly, relatively small differences to the references sample are observable for the Ga:LLZO single crystal after Li^+/H^+ exchange (see Figure 5.06b+c). This is in agreement with the recorded LIBS depth profile, showing very similar concentration gradients withing the material for both sample and reference (cf. Figure 5.04). A much higher impact of the Li^+/H^+ exchange experiments is visible for the Ta:LLZO polycrystalline pellet (see Figure 5.06d-f), which shows much more pronounced effects compared to the reference sample. Additionally, in contrast to Ga:LLZO single crystal a "kink" in the capacitive increase of the electrode feature can be observed for the Ta:LLZO pellet, indicating another (overlapped) semicircle, potentially being the grain boundary contribution shifted due to a strong increase of the grain boundary resistance. Overall, the EIS measurements are another indication of a fundamentally different Li^+/H^+ exchange behavior of the Ga:LLZO single crystal and the Ta:LLZO polycrystalline pellet, and thus confirm the finding of the chemical analysis.

5.4 Conclusion

Moisture-induced chemical degradation and Li^+/H^+ exchange of Ta:LLZO polycrystalline pellets as well as Ga:LLZO single crystals was investigated using water exposure followed by thorough (electro-)chemical analysis. Water analysis via ICP-OES in combination with direct solid analysis via LIBS depth profiling reveal strong differences in the Li^+/H^+ exchange behavior of the two LLZO variants. While in case of the Ga:LLZO single crystal, H^+ incorporation is limited to the region very close to sample surface, not extending more than 1–2 µm deep into the material, significant Li^+/H^+ exchange ranging from 70% to 5% and extending as far as 22 µm deep can be observed for the Ta:LLZO polycrystalline pellet. Most likely, a higher reactivity of the grain boundaries with H_2O in combination with an increased H^+ diffusion compared to the grains leads to a deeper degradation of polycrystalline LLZO. This enhanced H^+ penetration along the grain boundaries might negatively affect the compatibility of LLZO with aqueous electrolytes as well as ambient air, potentially limiting the application of the material.

6 Summary

A combination of electrochemical measurements and chemical analysis techniques was used to investigate various LLZO samples. Three key aspects of LLZO – all crucial for the application of the material – were studied:

- Conductivity fluctuations and their relation to stoichiometry changes
- Electrochemical stability and decomposition behavior
- Li^+/H^+ exchange due to contact with H_2O

As a first step, methods for the reliable and accurate chemical analysis of LLZO were developed. High-precision bulk analysis was achieved via ICP-OES using borax fusion for sample digestion, external calibration, internal-standard correction, and multiple measurement replications. Various Al:LLZO pellets were analyzed, revealing strong deviations to the intended compositions, which is most likely caused by (varying) loss of Li_2O at the high-temperature treatment during the LLZO synthesis. Interestingly, Li_2O loss seems to depend on the Al content, with less loss for Al-rich samples.

Access to locally resolved chemical information was gained by LA-ICP-OES and 2D elemental images of whole LLZO pellets were created, revealing strong Al inhomogeneities as well as significant variations of the local Li content. Reliable signal quantification was achieved by using in-house prepared matrixed-matched standards in combination with an internal-standard independent calibration strategy based on 100 m% normalization. The accuracy of the developed analysis was validated by comparing the derived average stoichiometry of a sample with the corresponding bulk composition, showing excellent agreement with relative deviations below 2 % for Al/La, Li/La as well as Zr/La atomic ratios. The precision of the Li determination was significantly improved compared to analogue LA-ICP-MS measurements, in which light elements such as Li suffer from matrix-induced suppression in the ion beam, confirming that LA-ICP-OES is more reliable for the analysis of LLZO.

To investigate the relationship between chemical composition and conductivity behavior, LA-ICP-OES imaging experiments were combined with macroscopic as well as microscopic conductivity measurements performed via (microelectrode) EIS. The analyzed nominally identical Al:LLZO pellets show significantly different (macroscopic) bulk conductivity with values ranging from 1.6×10^{-4} S cm^{-1} to 4.8×10^{-4} S cm^{-1} at room temperature. To determine the local ionic conductivity, microelectrodes with a diameter of 100 µm were used, probing the bulk conductivity of a similarly sized region beneath. In addition to confirming differences

between the nominally identical samples, the analysis revealed the existence of distinct conductivity inhomogeneities within individual pellets.

Spatially resolved chemical analysis showed that also strong stoichiometry variations can be observed for the very same LLZO samples. The LA-ICP-OES images were recorded in three different sampling depths (5 µm, 50 µm, and 100 µm), showing very similar results and thus confirming that no surface effects but bulk properties were probed by the analysis. Although conductivity as well stoichiometry inhomogeneities could be detected on the investigated samples, no clear correlation between the local chemical composition and the local ionic conductivity could be found. Neither a high (or low) Li content (between 6.1 pfu and 6.6 pfu) nor a certain amount of Al (between 0.15 pfu and 0.30 pfu) does lead to particularly high ionic conductivity. Since – in contrast to many common interpretations – the ionic conductivity of LLZO does not seem to correlate to Li stoichiometry or substitution amount, another yet unknown factor must have a pronounced effect on the conductivity behavior. For example, the Li conduction paths and local activation barriers might be strongly affected by the exact local crystal structure with varying site occupancy. Also the existence of oxygen vacancies and their effect on the Li-ion conduction might have a higher impact than the absolute local cation stoichiometry.

The electrochemical stability of LLZO was analyzed by means of electric field stress experiments on Ta:LLZO and Ga:LLZO single crystals. Changes in morphology, conductivity behavior, composition, and structure were examined to determine the impact of the DC voltages, which were applied in ambient air using ionically blocking Au electrodes in two different geometries.

In a first set of experiments, macroscopic stripe electrodes were used to apply a voltage of 3 V at elevated temperatures (approx. 350 °C). During the polarization, a solid is deposited on the negatively polarized electrode (cathode); most likely Li_2CO_3 or other Li-containing salts (LiOH, Li_2O) is formed due reduction of O_2 from air in presence of CO_2 and H_2O. The positively polarized electrode (anode) shows a rough surface after the polarization, indicating that O_2 is released due to the oxidation of oxide ions, leading to the formation of gas bubbles beneath the electrode. Also between the electrodes material changes can be observed: the local ionic conductivity of the LLZO single crystal, probed via ME-EIS before and after the polarization, increases close to the cathode and decreased close to the anode. Interestingly, also in this case the conductivity changes cannot be correlated to stoichiometry variations since chemical analysis via LIBS did not reveal any composition variations between the electrodes.

However, very close and/or beneath the stripe electrodes huge changes in the Li-stoichiometry were found, with an increase Li content on the cathodic side (due to the formation of Li-containing salts) and a strong Li-depletion on the anodic side.

For investigating the decomposition behavior of LLZO further, individual microelectrodes were positively polarized against a macroscopic counter electrode in another set of experiments. Increasing the applied voltage stepwise at elevated temperature (approx. 300 °C) revealed that LLZO decomposition starts at 1.2–1.4 V, which corresponds to stability limit of 4.1–4.3 V vs. Li^+/Li according to estimation of the counter electrode's chemical potential (2.9 V vs. Li^+/Li, defined by Li_2O during synthesis). Constant voltage experiments combined with subsequent LA-ICP-MS analysis showed that the Li-depletion beneath the polarized electrode, and thus the LLZO decomposition, reaches several µm deep into the material and is on-going even after several days of polarization. This means that no blocking interfacial layer is formed, which questions the compatibility of LLZO with high voltage cathode materials, especially because also at room temperature significant Li-depletion can be observed. To examine structural changes of the material, microfocus XRD measurements were performed, revealing the formation of $La_2Zr_2O_7$ at the polarized electrode. Most likely, LLZO decomposes to $La_2Zr_2O_7$ and La_2O_3 (in addition to Li_2CO_3 formation on the cathodic side), which is potentially accompanied by the formation of Li-depleted LLZO ($Li_{7-2x}La_3Zr_2O_{12-x}$) as intermediate product. In addition to transport of Li-ions, also substantial O^{2-} conduction is probably involved in the decomposition process.

In order to study the Li^+/H^+ exchange behavior of LLZO, Ta:LLZO polycrystalline pellets and Ga:LLZO single crystals were immersed in a hot (80°C) water bath for 80 min. Subsequently, the chemical composition of the used water as well as the LLZO samples was determined.

Water analysis was performed via ICP-OES, revealing that only Li^+ was released from the material in relevant amounts and thus confirming than indeed an Li^+/H^+ exchange reaction took place. The measurements show that significantly more ion exchange occurs for Ta:LLZO pellets compared to the Ga:LLZO single crystals. Furthermore, the analysis indicates an ongoing Li^+/H^+ exchange even after 55 min.

Changes of the H and Li content within the LLZO samples were investigated using LIBS depth profiling. Reliable signal quantification was achieved using pressed pellets with variable H content (prepared from calcinated LLZO precursors and $La(OH)_3$ powder) as matrix-matched calibration standards.

Using the obtained calibrations, quantitative H and Li depth profiles were recorded, which are consistent with each other (i.e., the Li content is negatively correlated to the H content) as well as the results of the ICP-OES analysis. Only little Li^+/H^+ exchange can be observed for Ga:LLZO single crystals, with the affected zone extending not more than 1–2 µm deep into the material. In contrast to that, strong Li^+/H^+ exchange is observable for Ta:LLZO pellets, with 60–70 % exchange for the first sample layer (0.0–2.0 µm sampling depth). This is followed by a zone of significant H^+ incorporation (40–5 %) up to a sampling depth of 22.2 µm, which is the highest H^+ penetration depth after H_2O immersion reported in literature so far. These strong differences in Li^+/H^+ exchange behavior of Ta:LLZO pellets and Ga:LLZO single crystals is probably caused by an increased H^+ incorporation and H^+ diffusion at/along the grain boundaries of LLZO, leading to a deeper degradation of polycrystalline samples. This additional degradation introduced by the grain boundaries indicates that LLZO is not stable in contact with aqueous electrolytes and/or ambient air, which might limit the application of the material.

List of abbreviations and symbols

Abbreviation	Meaning
AC	Alternating current
Al:LLZO	Aluminum stabilized LLZO ($Li_{7-3x}Al_xLa_3Zr_2O_{12}$)
CPE	Constant phase element
CV	Cyclic voltammetry
DC	Direct current
EDX	Energy-dispersive x-ray spectroscopy
EIS	Electrochemical impedance spectroscopy
Ga:LLZO	Gallium stabilized LLZO ($Li_{7-3x}Ga_xLa_3Zr_2O_{12}$)
ICP-MS	Inductively coupled plasma mass spectrometry
ICP-OES	Inductively coupled plasma optical emission spectroscopy
LA	Laser ablation
LA-ICP-MS	Laser ablation inductively coupled plasma mass spectrometry
LA-ICP-OES	Laser ablation inductively coupled plasma optical emission spectroscopy
LCO	$LiCoO_2$
LFP	$LiFePO_4$
LIB	Li-ion battery
LIBS	Laser induced breakdown spectroscopy
LLTO	$Li_{3x}La_{2/3-x}TiO_3$
LLZO	$Li_7La_3Zr_2O_{12}$
LMO	$LiMn_2O_4$
LOD	Limit of detection
LTO	$Li_4Ti_5O_{12}$
ME-EIS	Microelectrode electrochemical impedance spectroscopy
NASICON	Sodium super ionic conductor
NCA	$LiNi_{0.8}Co_{0.15}Al_{0.05}O_2$
NMC	$LiNi_{1/3}Mn_{1/3}Co_{1/3}O_2$
Pfu	Per formula unit

SEM	Scanning electron microscopy
SIMS	Secondary ion mass spectrometry
Ta:LLZO	Tantalum stabilized LLZO ($Li_{7-x}La_3Zr_{2-x}Ta_xO_{12}$)
XPS	X-ray photoelectron spectroscopy
XRD	X-ray diffraction
YSZ	Yttria-stabilized zirconia

Symbol	Total amount of transported Li^+
C	Capacitance
c	Concentration
D	Diffusion coefficient
d	Diameter
I	(Signal) intensity
l_D	Diffusion length
M_t	Total amount of (diffusing) substance
N_A	Avogadro constant (6.022×10^{23} mol^{-1})
R	Resistance
s	Sample standard deviation
R_{Spread}	Spreading resistance
t	Time
V	Volume
$\bar{x}$	Mean
Z	Impedance
ε	Permittivity
ε_r	Relative permittivity
ρ	Relative density
σ	(Ionic) conductivity
σ_{macro}	Bulk conductivity
σ_{Me}	Local conductivity (probed via microelectrode)
ω	Angular frequency

References

1 B. Dunn, H. Kamath and J.-M. Tarascon, Electrical energy storage for the grid: a battery of choices, *Science*, 2011, **334**, 928–935.

2 Q. Liu, Z. Geng, C. Han, Y. Fu, S. Li, Y.-b. He, F. Kang and B. Li, Challenges and perspectives of garnet solid electrolytes for all solid-state lithium batteries, *J. Power Sources*, 2018, **389**, 120–134.

3 S. Chu and A. Majumdar, Opportunities and challenges for a sustainable energy future, *Nature*, 2012, **488**, 294–303.

4 B. Diouf and R. Pode, Potential of lithium-ion batteries in renewable energy, *Renewable Energy*, 2015, **76**, 375–380.

5 M. M. Thackeray, C. Wolverton and E. D. Isaacs, Electrical energy storage for transportation—approaching the limits of, and going beyond, lithium-ion batteries, *Energy Environ. Sci.*, 2012, **5**, 7854.

6 J. M. Tarascon and M. Armand, Issues and challenges facing rechargeable lithium batteries, *Nature*, 2001, **414**, 359–367.

7 N. A. Kaskhedikar and J. Maier, Lithium Storage in Carbon Nanostructures, *Adv. Mater.*, 2009, **21**, 2664–2680.

8 G.-N. Zhu, Y.-G. Wang and Y.-Y. Xia, Ti-based compounds as anode materials for Li-ion batteries, *Energy Environ. Sci.*, 2012, **5**, 6652.

9 Z. Chen, I. Belharouak, Y.-K. Sun and K. Amine, Titanium-Based Anode Materials for Safe Lithium-Ion Batteries, *Adv. Funct. Mater.*, 2013, **23**, 959–969.

10 N. Nitta and G. Yushin, High-Capacity Anode Materials for Lithium-Ion Batteries: Choice of Elements and Structures for Active Particles, *Part. Part. Syst. Charact.*, 2014, **31**, 317–336.

11 J. Cabana, L. Monconduit, D. Larcher and M. R. Palacín, Beyond intercalation-based Li-ion batteries: the state of the art and challenges of electrode materials reacting through conversion reactions, *Adv. Mater.*, 2010, **22**, E170-92.

12 C.-M. Park, J.-H. Kim, H. Kim and H.-J. Sohn, Li-alloy based anode materials for Li secondary batteries, *Chem. Soc. Rev.*, 2010, **39**, 3115–3141.

13 N. Nitta, F. Wu, J. T. Lee and G. Yushin, Li-ion battery materials, *Materials Today*, 2015, **18**, 252–264.

14 K. Mizushima, P. C. Jones, P. J. Wiseman and J. B. Goodenough, Li_xCoO_2 (0<x<-1): A new cathode material for batteries of high energy density, *Mat. Res. Bull.*, 1980, **15**, 783–789.

15 T. Ohzuku and Y. Makimura, Layered Lithium Insertion Material of $LiCo_{1/3}Ni_{1/3}Mn_{1/3}O_2$ for Lithium-Ion Batteries, *Chem. Lett.*, 2001, **30**, 642–643.

16 C. J. Han, J. H. Yoon, W. I. Cho and H. Jang, Electrochemical properties of $LiNi_{0.8}Co_{0.2-x}Al_xO_2$ prepared by a sol–gel method, *J. Power Sources*, 2004, **136**, 132–138.

17 J. M. Tarascon, E. Wang, F. K. Shokoohi, W. R. McKinnon and S. Colson, The Spinel Phase of $LiMn_2O_4$ as a Cathode in Secondary Lithium Cells, *J. Electrochem. Soc.*, 1991, **138**, 2859–2864.

18 A. K. Padhi, K. S. Nanjundaswamy and J. B. Goodenough, Phospho-olivines as Positive-Electrode Materials for Rechargeable Lithium Batteries, *J. Electrochem. Soc.*, 1997, **144**, 1188–1194.

19 K. Xu, Nonaqueous Liquid Electrolytes for Lithium-Based Rechargeable Batteries, *Chem. Rev.*, 2004, **104**, 4303–4418.

20 M. Hu, X. Pang and Z. Zhou, Recent progress in high-voltage lithium ion batteries, *J. Power Sources*, 2013, **237**, 229–242.

21 J. Janek and W. G. Zeier, A solid future for battery development, *Nat. Energy*, 2016, **1**, 1–4.

22 M. Armand and J.-M. Tarascon, Building better batteries, *Nature*, 2008, **451**, 652–657.

23 Q. Wang, P. Ping, X. Zhao, G. Chu, J. Sun and C. Chen, Thermal runaway caused fire and explosion of lithium ion battery, *J. Power Sources*, 2012, **208**, 210–224.

24 D. Lisbona and T. Snee, A review of hazards associated with primary lithium and lithium-ion batteries, *Process Saf. Environ. Prot.*, 2011, **89**, 434–442.

25 K. Takada, Progress and prospective of solid-state lithium batteries, *Acta Materialia*, 2013, **61**, 759–770.

26 S. Ramakumar, C. Deviannapoorani, L. Dhivya, L. S. Shankar and R. Murugan, Lithium garnets: Synthesis, structure, Li^+ conductivity, Li^+ dynamics and applications, *Prog. Mater. Sci.*, 2017, **88**, 325–411.

27 A. Manthiram, X. Yu and S. Wang, Lithium battery chemistries enabled by solid-state electrolytes, *Nat. Rev. Mater.*, 2017, **2**, 294.

28 Y. Meesala, A. Jena, H. Chang and R. S. Liu, Recent Advancements in Li-Ion Conductors for All-Solid-State Li-Ion Batteries, *ACS Energy Lett.*, 2017, **2**, 2734–2751.

29 V. Thangadurai, S. Narayanan and D. Pinzaru, Garnet-type solid-state fast Li ion conductors for Li batteries: critical review, *Chem. Soc. Rev.*, 2014, **43**, 4714–4727.

30 F. Zheng, M. Kotobuki, S. Song, M. O. Lai and L. Lu, Review on solid electrolytes for all-solid-state lithium-ion batteries, *J. Power Sources*, 2018, **389**, 198–213.

31 P. Knauth, Inorganic solid Li ion conductors, *Solid State Ion.*, 2009, **180**, 911–916.

32 A.D. Robertson, A.R. West and A.G. Ritchie, Review of crystalline lithium-ion conductors suitable for high temperature battery applications, *Solid State Ion.*, 1997, **104**, 1–11.

33 X.-B. Cheng, R. Zhang, C.-Z. Zhao and Q. Zhang, Toward Safe Lithium Metal Anode in Rechargeable Batteries: A Review, *Chem. Rev.*, 2017, **117**, 10403–10473.

34 R. Murugan, V. Thangadurai and W. Weppner, Fast lithium ion conduction in garnet-type $Li_7La_3Zr_2O_{12}$, *Angew. Chem. Int. Ed.*, 2007, **46**, 7778–7781.

35 V. Thangadurai, D. Pinzaru, S. Narayanan and A. K. Baral, Fast Solid-State Li Ion Conducting Garnet-Type Structure Metal Oxides for Energy Storage, *J. Phys. Chem. Lett.*, 2015, **6**, 292–299.

36 J. Awaka, N. Kijima, H. Hayakawa and J. Akimoto, Synthesis and structure analysis of tetragonal $Li_7La_3Zr_2O_{12}$ with the garnet-related type structure, *J. Solid State Chem.*, 2009, **182**, 2046–2052.

37 H. Buschmann, J. Dölle, S. Berendts, A. Kuhn, P. Bottke, M. Wilkening, P. Heitjans, A. Senyshyn, H. Ehrenberg, A. Lotnyk, V. Duppel, L. Kienle and J. Janek, Structure and dynamics of the fast lithium ion conductor "$Li_7La_3Zr_2O_{12}$", *Phys. Chem. Chem. Phys.*, 2011, **13**, 19378–19392.

38 J. Wolfenstine, E. Rangasamy, J. L. Allen and J. Sakamoto, High conductivity of dense tetragonal $Li_7La_3Zr_2O_{12}$, *J. Power Sources*, 2012, **208**, 193–196.

39 G. Larraz, A. Orera and M. L. Sanjuán, Cubic phases of garnet-type $Li_7La_3Zr_2O_{12}$: The role of hydration, *J. Mater. Chem. A*, 2013, **1**, 11419–11428.

40 C. A. Geiger, E. Alekseev, B. Lazic, M. Fisch, T. Armbruster, R. Langner, M. Fechtelkord, N. Kim, T. Pettke and W. Weppner, Crystal chemistry and stability of "$Li_7La_3Zr_2O_{12}$" garnet, *Inorg. Chem.*, 2011, **50**, 1089–1097.

41 J. Awaka, A. Takashima, K. Kataoka, N. Kijima, Y. Idemoto and J. Akimoto, Crystal Structure of Fast Lithium-ion-conducting Cubic $Li_7La_3Zr_2O_{12}$, *Chem. Lett.*, 2011, **40**, 60–62.

42 Y. Li, J.-T. Han, C.-A. Wang, S. C. Vogel, H. Xie, M. Xu and J. B. Goodenough, Ionic distribution and conductivity in lithium garnet $Li_7La_3Zr_2O_{12}$, *J. Power Sources*, 2012, **209**, 278–281.

43 D. Wang, G. Zhong, W. K. Pang, Z. Guo, Y. Li, M. J. McDonald, R. Fu, J.-X. Mi and Y. Yang, Toward Understanding the Lithium Transport Mechanism in Garnet-type Solid Electrolytes, *Chem. Mater.*, 2015, **27**, 6650–6659.

44 Y. Li, J.-T. Han, C.-A. Wang, H. Xie and J. B. Goodenough, Optimizing Li^+ conductivity in a garnet framework, *J. Mater. Chem.*, 2012, **22**, 15357–15361.

45 E. J. Cussen, Structure and ionic conductivity in lithium garnets, *J. Mater. Chem.*, 2010, **20**, 5167–5173.

46 N. Bernstein, M. D. Johannes and K. Hoang, Origin of the structural phase transition in $Li_7La_3Zr_2O_{12}$, *Phys. Rev. Lett.*, 2012, **109**, 205702.

47 D. Rettenwander, P. Blaha, R. Laskowski, K. Schwarz, P. Bottke, M. Wilkening, C. A. Geiger and G. Amthauer, DFT Study of the Role of Al^{3+} in the Fast Ion-Conductor $Li_{7-3x}Al_{3+x}La_3Zr_2O_{12}$ Garnet, *Chem. Mater.*, 2014, **26**, 2617–2623.

48 A. J. Samson, K. Hofstetter, S. Bag and V. Thangadurai, A bird's-eye view of Li-stuffed garnet-type $Li_7La_3Zr_2O_{12}$ ceramic electrolytes for advanced all-solid-state Li batteries, *Energy Environ. Sci.*, 2019, **12**, 2957–2975.

49 E. Rangasamy, J. Wolfenstine and J. Sakamoto, The role of Al and Li concentration on the formation of cubic garnet solid electrolyte of nominal composition $Li_7La_3Zr_2O_{12}$, *Solid State Ion.*, 2012, **206**, 28–32.

50 S. Mukhopadhyay, T. Thompson, J. Sakamoto, A. Huq, J. Wolfenstine, J. L. Allen, N. Bernstein, D. A. Stewart and M. D. Johannes, Structure and Stoichiometry in Supervalent Doped $Li_7La_3Zr_2O_{12}$, *Chem. Mater.*, 2015, **27**, 3658–3665.

51 J. Wolfenstine, J. Sakamoto and J. L. Allen, Electron microscopy characterization of hot-pressed Al substituted $Li_7La_3Zr_2O_{12}$, *J. Mater. Sci.*, 2012, **47**, 4428–4431.

52 J. L. Allen, J. Wolfenstine, E. Rangasamy and J. Sakamoto, Effect of substitution (Ta, Al, Ga) on the conductivity of $Li_7La_3Zr_2O_{12}$, *J. Power Sources*, 2012, **206**, 315–319.

53 H. El-Shinawi, G. W. Paterson, D. A. MacLaren, E. J. Cussen and S. A. Corr, Low-temperature densification of Al-doped $Li_7La_3Zr_2O_{12}$, *J. Mater. Chem. A*, 2017, **5**, 319–329.

54 R. Wagner, G. J. Redhammer, D. Rettenwander, G. Tippelt, A. Welzl, S. Taibl, J. Fleig, A. Franz, W. Lottermoser and G. Amthauer, Fast Li-Ion-Conducting Garnet-Related $Li_{7-3x}Fe_xLa_3Zr_2O_{12}$ with Uncommon $I\bar{4}3d$ Structure, *Chem. Mater.*, 2016, **28**, 5943–5951.

55 J.-F. Wu, E.-Y. Chen, Y. Yu, L. Liu, Y. Wu, W. K. Pang, V. K. Peterson and X. Guo, Gallium-Doped $Li_7La_3Zr_2O_{12}$ Garnet-Type Electrolytes with High Lithium-Ion Conductivity, *ACS Appl. Mater. Interfaces*, 2017, **9**, 1542–1552.

56 S. Qin, X. Zhu, Y. Jiang, M.'e. Ling, Z. Hu and J. Zhu, Growth of self-textured Ga^{3+} - substituted $Li_7La_3Zr_2O_{12}$ ceramics by solid state reaction and their significant enhancement in ionic conductivity, *Appl. Phys. Lett.*, 2018, **112**, 113901.

57 R. H. Brugge, J. A. Kilner and A. Aguadero, Germanium as a donor dopant in garnet electrolytes, *Solid State Ion.*, 2019, **337**, 154–160.

58 E. Hanc, W. Zając and J. Molenda, Synthesis procedure and effect of Nd, Ca and Nb doping on structure and electrical conductivity of $Li_7La_3Zr_2O_{12}$ garnets, *Solid State Ion.*, 2014, **262**, 617–621.

59 A. Dumon, M. Huang, Y. Shen and C.-W. Nan, High Li ion conductivity in strontium doped $Li_7La_3Zr_2O_{12}$ garnet, *Solid State Ion.*, 2013, **243**, 36–41.

60 E. Rangasamy, J. Wolfenstine, J. Allen and J. Sakamoto, The effect of 24c-site (A) cation substitution on the tetragonal–cubic phase transition in $Li_{7-x}La_{3-x}A_xZr_2O_{12}$ garnet-based ceramic electrolyte, *J. Power Sources*, 2013, **230**, 261–266.

61 Y. Jiang, X. Zhu, S. Qin, M.'e. Ling and J. Zhu, Investigation of Mg^{2+}, Sc^{3+} and Zn^{2+} doping effects on densification and ionic conductivity of low-temperature sintered $Li_7La_3Zr_2O_{12}$ garnets, *Solid State Ion.*, 2017, **300**, 73–77.

62 S. Song, B. Chen, Y. Ruan, J. Sun, L. Yu, Y. Wang and J. Thokchom, Gd-doped $Li_7La_3Zr_2O_{12}$ garnet-type solid electrolytes for all-solid-state Li-Ion batteries, *Electrochim. Acta*, 2018, **270**, 501–508.

63 G. T. Hitz, E. D. Wachsman and V. Thangadurai, Highly Li-Stuffed Garnet-Type $Li_{7+x}La_3Zr_{2-x}Y_xO_{12}$, *J. Electrochem. Soc.*, 2013, **160**, A1248-A1255.

64 S. Ohta, T. Kobayashi and T. Asaoka, High lithium ionic conductivity in the garnet-type oxide $Li_{7-x}La_3(Zr_{2-x}, Nb_x)O_{12}$ (x=0–2), *J. Power Sources*, 2011, **196**, 3342–3345.

65 S. Ramakumar, L. Satyanarayana, S. V. Manorama and R. Murugan, Structure and Li^+ dynamics of Sb-doped $Li_7La_3Zr_2O_{12}$ fast lithium ion conductors, *Phys. Chem. Chem. Phys.*, 2013, **15**, 11327–11338.

66 Y. Li, C.-A. Wang, H. Xie, J. Cheng and J. B. Goodenough, High lithium ion conduction in garnet-type $Li_6La_3ZrTaO_{12}$, *Electrochem. Commun.*, 2011, **13**, 1289–1292.

67 H. Buschmann, S. Berendts, B. Mogwitz and J. Janek, Lithium metal electrode kinetics and ionic conductivity of the solid lithium ion conductors "$Li_7La_3Zr_2O_{12}$" and $Li_{7-x}La_3Zr_{2-x}Ta_xO_{12}$ with garnet-type structure, *J. Power Sources*, 2012, **206**, 236–244.

68 C. Shao, Z. Yu, H. Liu, Z. Zheng, N. Sun and C. Diao, Enhanced ionic conductivity of titanium doped $Li_7La_3Zr_2O_{12}$ solid electrolyte, *Electrochim. Acta*, 2017, **225**, 345–349.

69 X. Liu, Y. Li, T. Yang, Z. Cao, W. He, Y. Gao, J. Liu, G. Li and Z. Li, High lithium ionic conductivity in the garnet-type oxide $Li_{7-2x}La_3Zr_{2-x}M_xO_{12}$ (x =0-0.3) ceramics by sol-gel method, *J. Am. Ceram. Soc.*, 2017, **100**, 1527–1533.

70 C. Deviannapoorani, L. Dhivya, S. Ramakumar and R. Murugan, Lithium ion transport properties of high conductive tellurium substituted $Li_7La_3Zr_2O_{12}$ cubic lithium garnets, *J. Power Sources*, 2013, **240**, 18–25.

71 L. Dhivya, N. Janani, B. Palanivel and R. Murugan, Li^+ transport properties of W substituted $Li_7La_3Zr_2O_{12}$ cubic lithium garnets, *AIP Adv.*, 2013, **3**, 82115.

72 B. Xu, H. Duan, W. Xia, Y. Guo, H. Kang, H. Li and H. Liu, Multistep sintering to synthesize fast lithium garnets, *J. Power Sources*, 2016, **302**, 291–297.

73 R. H. Brugge, A. K. O. Hekselman, A. Cavallaro, F. M. Pesci, R. J. Chater, J. A. Kilner and A. Aguadero, Garnet Electrolytes for Solid State Batteries, *Chem. Mater.*, 2018, **30**, 3704–3713.

74 L. Cheng, J. S. Park, H. Hou, V. Zorba, G. Chen, T. Richardson, J. Cabana, R. Russo and M. Doeff, Effect of microstructure and surface impurity segregation on the electrical and electrochemical properties of dense Al-substituted $Li_7La_3Zr_2O_{12}$, *J. Mater. Chem. A*, 2014, **2**, 172–181.

75 L. Cheng, E. J. Crumlin, W. Chen, R. Qiao, H. Hou, S. Franz Lux, V. Zorba, R. Russo, R. Kostecki, Z. Liu, K. Persson, W. Yang, J. Cabana, T. Richardson, G. Chen and M. Doeff, The origin of high electrolyte-electrode interfacial resistances in lithium cells containing garnet type solid electrolytes, *Phys. Chem. Chem. Phys.*, 2014, **16**, 18294–18300.

76 H. Hou, L. Cheng, T. Richardson, G. Chen, M. Doeff, R. Zheng, R. Russo and V. Zorba, Three-dimensional elemental imaging of Li-ion solid-state electrolytes using fs-laser induced breakdown spectroscopy (LIBS), *J. Anal. At. Spectrom.*, 2015, **30**, 2295–2302.

77 L. Cheng, H. Hou, S. Lux, R. Kostecki, R. Davis, V. Zorba, A. Mehta and M. Doeff, Enhanced lithium ion transport in garnet-type solid state electrolytes, *J. Electroceram. (Journal of Electroceramics)*, 2017, **38**, 168–175.

78 M. Xu, M. S. Park, J. M. Lee, T. Y. Kim, Y. S. Park and E. Ma, Mechanisms of Li^+ transport in garnet-type cubic $Li_{3+x}La_3M_2O_{12}$ (M = Te, Nb, Zr), *Phys. Rev. B*, 2012, **85**, 52301.

79 J. Han, J. Zhu, Y. Li, X. Yu, S. Wang, G. Wu, H. Xie, S. C. Vogel, F. Izumi, K. Momma, Y. Kawamura, Y. Huang, J. B. Goodenough and Y. Zhao, Experimental visualization of lithium conduction pathways in garnet-type $Li_7La_3Zr_2O_{12}$, *Chem. Commun.*, 2012, **48**, 9840–9842.

80 R. Jalem, Y. Yamamoto, H. Shiiba, M. Nakayama, H. Munakata, T. Kasuga and K. Kanamura, Concerted Migration Mechanism in the Li Ion Dynamics of Garnet-Type $Li_7La_3Zr_2O_{12}$, *Chem. Mater.*, 2013, **25**, 425–430.

81 Y. Jin and P. J. McGinn, $Li_7La_3Zr_2O_{12}$ electrolyte stability in air and fabrication of a Li/$Li_7La_3Zr_2O_{12}$/$Cu_{0.1}V_2O_5$ solid-state battery, *J. Power Sources*, 2013, **239**, 326–331.

82 W. Xia, B. Xu, H. Duan, Y. Guo, H. Kang, H. Li and H. Liu, Ionic Conductivity and Air Stability of Al-Doped $Li_7La_3Zr_2O_{12}$ Sintered in Alumina and Pt Crucibles, *ACS Appl. Mater. Interfaces*, 2016, **8**, 5335–5342.

83 A. Sharafi, S. Yu, M. Naguib, M. Lee, C. Ma, H. M. Meyer, J. Nanda, M. Chi, D. J. Siegel and J. Sakamoto, Impact of air exposure and surface chemistry on Li–$Li_7La_3Zr_2O_{12}$ interfacial resistance, *J. Mater. Chem. A*, 2017, **5**, 13475–13487.

84 C. Sun, J. Liu, Y. Gong, D. P. Wilkinson and J. Zhang, Recent advances in all-solid-state rechargeable lithium batteries, *Nano Energy*, 2017, **33**, 363–386.

85 M. Kotobuki, K. Kanamura, Y. Sato and T. Yoshida, Fabrication of all-solid-state lithium battery with lithium metal anode using Al_2O_3-added $Li_7La_3Zr_2O_{12}$ solid electrolyte, *J. Power Sources*, 2011, **196**, 7750–7754.

86 J. Wolfenstine, J. Ratchford, E. Rangasamy, J. Sakamoto and J. L. Allen, Synthesis and high Li-ion conductivity of Ga-stabilized cubic $Li_7La_3Zr_2O_{12}$, *Mater. Chem. Phys.*, 2012, **134**, 571–575.

87 S. Smetaczek, M. Bonta, A. Wachter-Welzl, S. Taibl, R. Wagner, D. Rettenwander, J. Fleig and A. Limbeck, Spatially resolved stoichiometry determination of $Li_7La_3Zr_2O_{12}$ solid-state electrolytes using LA-ICP-OES, *J. Anal. At. Spectrom.*, 2020, **35**, 972–983.

88 A. Wachter-Welzl, J. Kirowitz, R. Wagner, S. Smetaczek, G. C. Brunauer, M. Bonta, D. Rettenwander, S. Taibl, A. Limbeck, G. Amthauer and J. Fleig, The origin of conductivity variations in Al-stabilized $Li_7La_3Zr_2O_{12}$ ceramics, *Solid State Ion.*, 2018, **319**, 203–208.

89 A. Wachter-Welzl, R. Wagner, D. Rettenwander, S. Taibl, G. Amthauer and J. Fleig, Microelectrodes for local conductivity and degradation measurements on Al stabilized $Li_7La_3Zr_2O_{12}$ garnets, *J. Electroceram.*, 2017, **38**, 176–181.

90 C.-L. Tsai, E. Dashjav, E.-M. Hammer, M. Finsterbusch, F. Tietz, S. Uhlenbruck and H. P. Buchkremer, High conductivity of mixed phase Al-substituted $Li_7La_3Zr_2O_{12}$, *J. Electroceram.*, 2015, **35**, 25–32.

91 X. X. Pan, J. X. Wang, X. H. Chang, Y. D. Li and W. B. Guan, A novel solid-liquid route for synthesizing cubic garnet Al-substituted $Li_7La_3Zr_2O_{12}$, *Solid State Ion.*, 2018, **317**, 1–6.

92 K. H. Kim, T. Hirayama, C. A.J. Fisher, K. Yamamoto, T. Sato, K. Tanabe, S. Kumazaki, Y. Iriyama and Z. Ogumi, Characterization of grain-boundary phases in $Li_7La_3Zr_2O_{12}$ solid electrolytes, *Mater. Charact.*, 2014, **91**, 101–106.

93 L. Cheng, C. H. Wu, A. Jarry, W. Chen, Y. Ye, J. Zhu, R. Kostecki, K. Persson, J. Guo, M. Salmeron, G. Chen and M. Doeff, Interrelationships among Grain Size, Surface Composition, Air Stability, and Interfacial Resistance of Al-Substituted $Li_7La_3Zr_2O_{12}$ Solid Electrolytes, *ACS Appl. Mater. Interfaces*, 2015, **7**, 17649–17655.

94 M. Zarabian, M. Bartolini, P. Pereira-Almao and V. Thangadurai, X-ray Photoelectron Spectroscopy and AC Impedance Spectroscopy Studies of Li-La-Zr-O Solid Electrolyte Thin Film/$LiCoO_2$ Cathode Interface for All-Solid-State Li Batteries, *J. Electrochem. Soc.*, 2017, **164**, A1133.

95 S. Uhlenbruck, C. Dellen, S. Möller, S. Lobe, C.-L. Tsai, M. Finsterbusch, M. Bram and O. Guillon, Reactions of garnet-based solid-state lithium electrolytes with water — A depth-resolved study, *Solid State Ion.*, 2018, **320**, 259–265.

96 F. M. Pesci, R. H. Brugge, A. K. O. Hekselman, A. Cavallaro, R. J. Chater and A. Aguadero, Elucidating the role of dopants in the critical current density for dendrite formation in garnet electrolytes, *J. Mater. Chem. A*, 2018, **6**, 19817–19827.

97 D. Rettenwander, R. Wagner, A. Reyer, M. Bonta, L. Cheng, M. M. Doeff, A. Limbeck, M. Wilkening and G. Amthauer, Interface Instability of Fe-Stabilized $Li_7La_3Zr_2O_{12}$ versus Li Metal, *J. Phys. Chem. C*, 2018, **122**, 3780–3785.

98 A. Limbeck, M. Bonta and W. Nischkauer, Improvements in the direct analysis of advanced materials using ICP-based measurement techniques, *J. Anal. At. Spectrom.*, 2017, **32**, 212–232.

99 J. S. Becker, Applications of inductively coupled plasma mass spectrometry and laser ablation inductively coupled plasma mass spectrometry in materials science, *Spectrochim. Acta Part B At. Spectrosc.*, 2002, **57**, 1805–1820.

100 M. Kalapsazova, R. Stoyanova, E. Zhecheva, G. Tyuliev and D. Nihtianova, Sodium deficient nickel–manganese oxides as intercalation electrodes in lithium ion batteries, *J. Mater. Chem. A*, 2014, **2**, 19383–19395.

101 T. Schwieters, M. Evertz, M. Mense, M. Winter and S. Nowak, Lithium loss in the solid electrolyte interphase: Lithium quantification of aged lithium ion battery graphite electrodes by means of laser ablation inductively coupled plasma mass spectrometry and inductively coupled plasma optical emission spectroscopy, *J. Power Sources*, 2017, **356**, 47–55.

102 T. Schwieters, M. Evertz, A. Fengler, M. Börner, T. Dagger, Y. Stenzel, P. Harte, M. Winter and S. Nowak, Visualizing elemental deposition patterns on carbonaceous anodes from lithium ion batteries: A laser ablation-inductively coupled plasma-mass spectrometry study on factors influencing the deposition of lithium, nickel, manganese and cobalt after dissolution and migration from the $Li_1[Ni_{1/3}Mn_{1/3}Co_{1/3}]O_2$ and $LiMn_{1.5}Ni_{0.5}O_4$ cathode, *J. Power Sources*, 2018, **380**, 194–201.

103 P. Harte, M. Evertz, T. Schwieters, M. Diehl, M. Winter and S. Nowak, Adaptation and improvement of an elemental mapping method for lithium ion battery electrodes and separators by means of laser ablation-inductively coupled plasma-mass spectrometry, *Anal. Bioanal. Chem.*, 2019, **411**, 581–589.

104 T. Dagger, J. Kasnatscheew, B. Vortmann-Westhoven, T. Schwieters, S. Nowak, M. Winter and F. M. Schappacher, Performance tuning of lithium ion battery cells with area-oversized graphite based negative electrodes, *J. Power Sources*, 2018, **396**, 519–526.

105 A. Limbeck, P. Galler, M. Bonta, G. Bauer, W. Nischkauer and F. Vanhaecke, Recent advances in quantitative LA-ICP-MS analysis: challenges and solutions in the life sciences and environmental chemistry, *Anal. Bioanal. Chem.*, 2015, **407**, 6593–6617.

106 R. Wagner, G. J. Redhammer, D. Rettenwander, A. Senyshyn, W. Schmidt, M. Wilkening and G. Amthauer, Crystal Structure of Garnet-Related Li-Ion Conductor $Li_{7-3x}Ga_xLa_3Zr_2O_{12}$: Fast Li-Ion Conduction Caused by a Different Cubic Modification?, *Chem. Mater.*, 2016, **28**, 1861–1871.

107 Y. Liu, Z. Hu, S. Gao, D. Günther, J. Xu, C. Gao and H. Chen, In situ analysis of major and trace elements of anhydrous minerals by LA-ICP-MS without applying an internal standard, *Chem. Geol.*, 2008, **257**, 34–43.

108 E. H. Evans and J. J. Giglio, Interferences in inductively coupled plasma mass spectrometry. A review, *J. Anal. At. Spectrom.*, 1993, **8**, 1.

109 S. Smetaczek, A. Wachter-Welzl, R. Wagner, D. Rettenwander, G. Amthauer, L. Andrejs, S. Taibl, A. Limbeck and J. Fleig, Local Li-ion conductivity changes within Al stabilized $Li_7La_3Zr_2O_{12}$ and their relationship to three-dimensional variations of the bulk composition, *J. Mater. Chem. A*, 2019, **7**, 6818–6831.

110 Y. Zhang, F. Chen, R. Tu, Q. Shen and L. Zhang, Field assisted sintering of dense Al-substituted cubic phase $Li_7La_3Zr_2O_{12}$ solid electrolytes, *J. Power Sources*, 2014, **268**, 960–964.

111 J. Fleig and J. Maier, Local conductivitiy measurements on AgCl surfaces using microelectrodes, *Solid State Ion.*, 1996, **85**, 9–15.

112 J. Fleig and J. Maier, Microcontact impedance measurements of individual highly conductive grain boundaries, *Phys. Chem. Chem. Phys.*, 1999, **1**, 3315–3320.

113 J.-S. Lee, J. Fleig, J. Maier, T.-J. Chung and D.-Y. Kim, Microcontact impedance spectroscopy in nitrogen-graded zirconia, *Solid State Ion.*, 2005, **176**, 1711–1716.

114 D. Rettenwander, A. Welzl, S. Pristat, F. Tietz, S. Taibl, G. J. Redhammer and J. Fleig, A microcontact impedance study on NASICON-type $Li_{1+x}Al_xTi_{2-x}(PO_4)_3$ ($0 \leq x \leq 0.5$) single crystals, *J. Mater. Chem. A*, 2016, **4**, 1506–1513.

115 J. Fleig, Microelectrodes in solid state ionics, *Solid State Ion.*, 2003, **161**, 279–289.

116 T. Degen, M. Sadki, E. Bron, U. König and G. Nénert, The HighScore suite, 2014.

117 D. Rettenwander, A. Welzl, L. Cheng, J. Fleig, M. Musso, E. Suard, M. M. Doeff, G. J. Redhammer and G. Amthauer, Synthesis, Crystal Chemistry, and Electrochemical Properties of $Li_{7-2x}La_3Zr_{2-x}Mo_xO_{12}$ (x = 0.1-0.4), *Inorg. Chem.*, 2015, **54**, 10440–10449.

118 J. Fleig, The grain boundary impedance of random microstructures: numerical simulations and implications for the analysis of experimental data, *Solid State Ion.*, 2002, **150**, 181–193.

119 Y. Zhang, J. Cai, F. Chen, R. Tu, Q. Shen, X. Zhang and L. Zhang, Preparation of cubic $Li_7La_3Zr_2O_{12}$ solid electrolyte using a nano-sized core–shell structured precursor, *J. Alloys and Compd.*, 2015, **644**, 793–798.

120 Y. Matsuda, K. Sakamoto, M. Matsui, O. Yamamoto, Y. Takeda and N. Imanishi, Phase formation of a garnet-type lithium-ion conductor $Li_{7-3x}Al_xLa_3Zr_2O_{12}$, *Solid State Ion.*, 2015, **277**, 23–29.

121 W. E. Tenhaeff, E. Rangasamy, Y. Wang, A. P. Sokolov, J. Wolfenstine, J. Sakamoto and N. J. Dudney, Resolving the Grain Boundary and Lattice Impedance of Hot-Pressed $Li_7La_3Zr_2O_{12}$ Garnet Electrolytes, *ChemElectroChem*, 2014, **1**, 375–378.

122 F. Llewellyn-Jones, *The physics of electrical contacts*, Clarendon Press, Oxford, 1957.

123 R. Holm, *Electric contacts handbook*, Springer, Berlin, 3rd edn., 1958.

124 J. Newman, Resistance for Flow of Current to a Disk, *J. Electrochem. Soc.*, 1966, **113**, 501.

125 A. Orera, G. Larraz, J. A. Rodríguez-Velamazán, J. Campo and M. L. Sanjuán, Influence of Li^+ and H^+ Distribution on the Crystal Structure of $Li_{7-x}H_xLa_3Zr_2O_{12}$ ($0 \leq x \leq 5$) Garnets, *Inorg. Chem.*, 2016, **55**, 1324–1332.

126 C. Ma, E. Rangasamy, C. Liang, J. Sakamoto, K. L. More and M. Chi, Excellent stability of a lithium-ion-conducting solid electrolyte upon reversible Li^+/H^+ exchange in aqueous solutions, *Angw. Chem. Int. Ed.*, 2015, **54**, 129–133.

127 E. Yi, W. Wang, J. Kieffer and R. M. Laine, Key parameters governing the densification of cubic-$Li_7La_3Zr_2O_{12}$ Li^+ conductors, *J. Power Sources*, 2017, **352**, 156–164.

128 M. Kubicek, A. Wachter-Welzl, D. Rettenwander, R. Wagner, S. Berendts, R. Uecker, G. Amthauer, H. Hutter and J. Fleig, Oxygen Vacancies in Fast Lithium-Ion Conducting Garnets, *Chem. Mater.*, 2017, **29**, 7189–7196.

129 X. He, Y. Zhu and Y. Mo, Origin of fast ion diffusion in super-ionic conductors, *Nat. Commun.*, 2017, **8**, 15893.

130 Y. Zhu, X. He and Y. Mo, Origin of Outstanding Stability in the Lithium Solid Electrolyte Materials: Insights from Thermodynamic Analyses Based on First-Principles Calculations, *ACS Appl. Mater. Interfaces*, 2015, **7**, 23685–23693.

131 F. Han, Y. Zhu, X. He, Y. Mo and C. Wang, Electrochemical Stability of $Li_{10}GeP_2S_{12}$ and $Li_7La_3Zr_2O_{12}$ Solid Electrolytes, *Adv. Energy Mater.*, 2016, **6**, 1501590.

132 W. d. Richards, L. J. Miara, Y. Wang, J. C. Kim and G. Ceder, Interface Stability in Solid-State Batteries, *Chem. Mater.*, 2016, **28**, 266–273.

133 T. Thompson, S. Yu, L. Williams, R. D. Schmidt, R. Garcia-Mendez, J. Wolfenstine, J. L. Allen, E. Kioupakis, D. J. Siegel and J. Sakamoto, Electrochemical Window of the Li-Ion Solid Electrolyte $Li_7La_3Zr_2O_{12}$, *ACS Energy Lett.*, 2017, **2**, 462–468.

134 T. M. Huber, A. K. Opitz, M. Kubicek, H. Hutter and J. Fleig, Temperature gradients in microelectrode measurements: Relevance and solutions for studies of SOFC electrode materials, *Solid State Ion.*, 2014, **268**, 82–93.

135 X. Zhan, S. Lai, M. P. Gobet, S. G. Greenbaum and M. Shirpour, Defect chemistry and electrical properties of garnet-type $Li_7La_3Zr_2O_{12}$, *Phys. Chem. Chem. Phys.*, 2018, **20**, 1447–1459.

136 K. C. Lau, L. A. Curtiss and J. Greeley, Density Functional Investigation of the Thermodynamic Stability of Lithium Oxide Bulk Crystalline Structures as a Function of Oxygen Pressure, *J. Phys. Chem. C*, 2011, **115**, 23625–23633.

137 G. J. Redhammer, P. Badami, M. Meven, S. Ganschow, S. Berendts, G. Tippelt and D. Rettenwander, Wet-Environment-Induced Structural Alterations in Single- and Polycrystalline LLZTO Solid Electrolytes Studied by Diffraction Techniques, *ACS Appl. Mater. Interfaces*, 2021, **13**, 350–359.

138 K. Hofstetter, A. J. Samson, S. Narayanan and V. Thangadurai, Present understanding of the stability of Li-stuffed garnets with moisture, carbon dioxide, and metallic lithium, *J. Power Sources*, 2018, **390**, 297–312.

139 W. Xia, B. Xu, H. Duan, X. Tang, Y. Guo, H. Kang, H. Li and H. Liu, Reaction mechanisms of lithium garnet pellets in ambient air, *J. Am. Ceram. Soc.*, 2017, **100**, 2832–2839.

140 X. Liu, Y. Chen, Z. D. Hood, C. Ma, S. Yu, A. Sharafi, H. Wang, K. An, J. Sakamoto, D. J. Siegel, Y. Cheng, N. H. Jalarvo and M. Chi, Elucidating the mobility of H^+ and Li^+ ions in $(Li_{6.25-x}H_xAl_{0.25})La_3Zr_2O_{12}$ via correlative neutron and electron spectroscopy, *Energy Environ. Sci.*, 2019, **12**, 945–951.

141 C. Hiebl, D. Young, R. Wagner, H. M. R. Wilkening, G. J. Redhammer and D. Rettenwander, Proton Bulk Diffusion in Cubic $Li_7La_3Z_2O_{12}$ Garnets as Probed by Single X-ray Diffraction, *J. Phys. Chem. C*, 2019, **123**, 1094–1098.

142 C. Liu, K. Rui, C. Shen, M. E. Badding, G. Zhang and Z. Wen, Reversible ion exchange and structural stability of garnet-type Nb-doped $Li_7La_3Zr_2O_{12}$ in water for applications in lithium batteries, *J. Power Sources*, 2015, **282**, 286–293.

143 Y. Li, J.-T. Han, S. C. Vogel and C. an Wang, The reaction of $Li_{6.5}La_3Zr_{1.5}Ta_{0.5}O_{12}$ with water, *Solid State Ion.*, 2015, **269**, 57–61.

144 Y. Shimonishi, A. Toda, T. Zhang, A. Hirano, N. Imanishi, O. Yamamoto and Y. Takeda, Synthesis of garnet-type $Li_{7-x}La_3Zr_2O_{12-1/2x}$ and its stability in aqueous solutions, *Solid State Ion.*, 2011, **183**, 48–53.

145 Z. F. Yow, Y. L. Oh, W. Gu, R. P. Rao and S. Adams, Effect of Li^+/H^+ exchange in water treated Ta-doped $Li_7La_3Zr_2O_{12}$, *Solid State Ion.*, 2016, **292**, 122–129.

146 K. H. Kurniawan, M. O. Tjia and K. Kagawa, Review of Laser-Induced Plasma, Its Mechanism, and Application to Quantitative Analysis of Hydrogen and Deuterium, *Appl. Spectrosc. Rev.*, 2014, **49**, 323–434.

147 S. Imashuku, T. Kamimura, S. Kashiwakura and K. Wagatsuma, Quantitative Analysis of Hydrogen in High-Hydrogen-Content Material of Magnesium Hydride via Laser-Induced Breakdown Spectroscopy, *Anal. Chem.*, 2020, **92**, 11171–11176.

148 K. H. Kurniawan, M. Pardede, R. Hedwig, Z. S. Lie, T. J. Lie, D. P. Kurniawan, M. Ramli, K.-i. Fukumoto, H. Niki, S. N. Abdulmadjid, N. Idris, T. Maruyama, K. Kagawa and M. O. Tjia, Quantitative hydrogen analysis of zircaloy-4 using low-pressure laser plasma technique, *Anal. Chem.*, 2007, **79**, 2703–2707.

149 K. H. Kurniawan, T. J. Lie, N. Idris, T. Kobayashi, T. Maruyama, K. Kagawa, M. O. Tjia and A. N. Chumakov, Hydrogen analysis of zircaloy tube used in nuclear power station using laser plasma technique, *J. Appl. Phys.*, 2004, **96**, 6859–6862.

150 W. Rapin, P.-Y. Meslin, S. Maurice, R. C. Wiens, D. Laporte, B. Chauviré, O. Gasnault, S. Schröder, P. Beck, S. Bender, O. Beyssac, A. Cousin, E. Dehouck, C. Drouet, O. Forni, M. Nachon, N. Melikechi, B. Rondeau, N. Mangold and N. H. Thomas, Quantification of water content by laser induced breakdown spectroscopy on Mars, *Spectrochim. Acta Part B At. Spectrosc.*, 2017, **130**, 82–100.

151 J. Crank, *The mathematics of diffusion*, Clarendon Press, Oxford, 2nd edn., 1976.

152 L. G. Harrison, Influence of dislocations on diffusion kinetics in solids with particular reference to the alkali halides, *Trans. Faraday Soc.*, 1961, **57**, 1191.

153 Y. Mishin, C. Herzig, J. Bernardini and W. Gust, Grain boundary diffusion: fundamentals to recent developments, *Int. Mater. Rev.*, 1997, **42**, 155–178.

154 R.T.P. Whipple, Concentration contours in grain boundary diffusion, *Phil. Mag.*, 1954, **45**, 1225–1236.

155 A. D. Le Claire, The analysis of grain boundary diffusion measurements, *Br. J. Appl. Phys.*, 1963, **14**, 351–356.